Oxide Coatings on Nickel-Rich Layered Cathode Active Materials for Thiophosphate-Based Solid-State Batteries

Dem Fachbereich Biologie und Chemie
der Justus-Liebig-Universität Gießen
vorgelegte Dissertation zur Erlangung
des akademischen Grades
Doktor der Naturwissenschaften
− Dr. rer. nat. −

David Kitsche

Januar 2023

Dekan / Dean	Prof. Dr. Thomas Wilke
1. Gutachter / 1st Reviewer	Prof. Dr. Jürgen Janek (Justus-Liebig-Universität Gießen)
2. Gutachter / 2nd Reviewer	Prof. Dr. Maren Lepple (Justus-Liebig-Universität Gießen)
Eingereicht / submitted	31.01.2023
Disputation / disputation	30.03.2023

Eidesstattliche Erklärung

Die vorliegende Arbeit wurde im Zeitraum vom 01.07.2019 bis 16.01.2023 im Battery and Electrochemistry Laboratory (BELLA) des Instituts für Nanotechnologie am Karlsruher Institut für Technologie unter Betreuung von Prof. Dr. Jürgen Janek angefertigt.

Ich erkläre:

Ich habe die vorgelegte Dissertation selbstständig und ohne unerlaubte fremde Hilfe und nur mit den Hilfen angefertigt, die ich in der Dissertation angegeben habe. Alle Textstellen, die wörtlich oder sinngemäß aus veröffentlichten Schriften entnommen sind, und alle Angaben, die auf mündlichen Auskünften beruhen, sind als solche kenntlich gemacht. Ich stimme einer eventuellen Überprüfung meiner Dissertation durch eine Antiplagiat-Software zu. Bei den von mir durchgeführten und in der Dissertation erwähnten Untersuchungen habe ich die Grundsätze guter wissenschaftlicher Praxis, wie sie in der „Satzung der Justus-Liebig-Universität Gießen zur Sicherung guter wissenschaftlicher Praxis“ niedergelegt sind, eingehalten.

Karlsruhe, 31.01.2023

____

David Kitsche

Abstract

Lithium-ion batteries (LIBs) lay the foundation of today's portable electronics, which have profoundly changed modern society, providing mobile communication and many other functionalities. However, recently they have drawn even more attention, especially as energy storage devices for electric vehicles (EVs) which are expected to replace vehicles powered by an internal combustion engine in the long run. This has strongly driven the development of LIBs, which are approaching physical limits regarding their energy density. Solid-state batteries (SSBs) are regarded as a promising next-generation battery technology. They are hoped to enable higher energy densities by making use of a Li metal anode. Not containing a flammable liquid, they could also eventually turn out to be safer than LIBs. Among the classes of solid electrolytes (SEs) that could replace their liquid counterpart in conventional LIB cells, thiophosphates stand out due to their high ionic conductivities and favorable processability. The main drawback of thiophosphates is their low thermodynamic stability, leading to a number of incompatibility issues at both anode and cathode. On the cathode side of SSBs, severe thiophosphate oxidation has to be prevented by using protective layers, especially on the cathode active material (CAM). Many such CAM coatings have been proposed in the past and were shown to have functionalities beyond preventing SE oxidation. Moreover, different methods have been used to deposit these layers on CAMs, each with different capabilities regarding the achievable coating thickness and morphology.

The aim of this doctoral project was to prepare, characterize, optimize and test protective CAM coatings on $LiNi_{0.85}Co_{0.10}Mn_{0.05}O_2$, a Ni-rich NCM-type CAM, for use in thiophosphate-based SSB cells. The work resulted in publications on three different metal oxide coatings. Two of them are based on the use of atomic layer deposition (ALD), a method that previously had rarely been employed for this application. Nanometer-thin, conformal and adjustable layers of the binary oxides HfO_2 and ZrO_2 could be obtained. The coatings are nanocrystalline and beneficial for the cycling performance of the NCM CAM, especially when a post-heat treatment at moderate temperatures is performed. A systematic characterization of the ZrO_2@NCM after heat treatment at temperatures ranging between 300 and 700 °C revealed a multifaceted evolution of the (sub)surface layer. This includes changes in crystallinity and a reaction between substrate and coating. The two studies showed that ALD is a viable tool to prepare high-quality model-type coatings that are well-suited for systematic investigations into the property-performance relationships and thereby advance the understanding of the working principles of CAM coatings. Apart from that, a facile wet chemical method was used to deposit a composite oxide coating consisting of Li_3NbO_4 nanoparticles and Li_2CO_3. This protective layer enabled excellent cycling performance regarding reversible specific capacity and rate capability (212 and 150 mAh/g_{CAM} at 0.2 and 2.0 mA/g_{CAM}, respectively) as well as stability (more than 80% capacity retention after 200 cycles). In doing so, the coating compared favorably to common lithium niobate coatings, thus showing that there is still room for improvements when it comes to wet chemical coating methods and CAM coatings in general.

Zusammenfassung

Lithium-Ionen-Akkumulatoren (engl. lithium-ion batteries, LIBs) sind die Grundlage heutiger portabler Elektronik, die die moderne Gesellschaft durch mobile Kommunikation und viele andere Anwendungen des alltäglichen Lebens tiefgreifend verändert hat. In jüngster Zeit haben LIBs jedoch insbesondere als Energiespeicher für Elektrofahrzeuge Aufmerksamkeit auf sich gezogen, die erwartungsgemäß Fahrzeuge mit Verbrennungsmotor langfristig ersetzen werden. Dies hat die Entwicklung von LIBs stark vorangetrieben, sodass sie sich hinsichtlich ihrer Energiedichte physikalischen Grenzen nähern. Festkörperbatterien (engl. solid-state batteries, SSBs) gelten als vielversprechende Technologie der Zukunft. Dabei ist von zentraler Bedeutung, dass sie höhere Energiedichten aufweisen können, wenn sie den Einsatz einer Lithiummetallanode ermöglichen. Da sie keine entflammbare Flüssigkeit enthalten, könnten sie sich auch als sicherer als LIBs erweisen. Unter den Festelektrolyten, die Flüssigelektrolyten in herkömmlichen LIB-Zellen ersetzen könnten, stechen Thiophosphate aufgrund ihrer hohen Ionenleitfähigkeit und günstigen Verarbeitbarkeit hervor. Der größte Nachteil von Thiophosphaten ist ihre geringe thermodynamische Stabilität, was zu einer Reihe von Inkompatibilitätsproblemen sowohl an der Anode als auch Kathode führt. Auf der Kathodenseite einer Feststoffbatterie muss eine starke oxidative Zersetzung der Thiophosphate durch Schutzschichten verhindert werden, insbesondere an der Grenzfläche zum Kathodenaktivmaterial (engl. cathode active material, CAM). Viele CAM-Beschichtungen wurden in der Vergangenheit entwickelt und es wurde gezeigt, dass sie eine Reihe von Funktionen in SSB-Kathoden erfüllen können. Darüber hinaus wurden verschiedene Methoden zur Abscheidung dieser Schichten auf CAMs angewandt, die sich bezüglich der erreichbaren Schichtdicke und Morphologie unterscheiden.

Das Ziel dieser Promotion war die Herstellung, Charakterisierung, Optimierung und Testung von CAM-Schutzschichten für die Verwendung von $LiNi_{0.85}Co_{0.10}Mn_{0.05}O_2$, einem nickelreichen NCM-Material, in Thiophosphat-basierten SSB-Zellen. Die Ergebnisse der Arbeiten an drei verschiedenen Metalloxidbeschichtungen wurden veröffentlicht. Zwei davon beruhen auf der Verwendung der Atomlagenabscheidung (ALD), einer Methode, die bisher nur selten für diese Anwendung eingesetzt wurde. Es konnten nanometerdünne, konforme und kontrollierbare Schichten aus den Binäroxiden HfO_2 und ZrO_2 hergestellt werden. Die nanokristallinen Schichten wirken sich positiv auf die Leistungsfähigkeit des CAMs aus, insbesondere wenn eine thermische Nachbehandlung bei moderaten Temperaturen durchgeführt wird. Eine systematische Charakterisierung des ZrO_2@NCM nach einer Wärmebehandlung bei Temperaturen zwischen 300 und 700 °C zeigte eine vielschichtige Transformation der modifizierten Oberfläche. Dies beinhaltet Veränderungen der Kristallinität und eine Reaktion zwischen dem Substrat und der Beschichtung. Die beiden Studien haben gezeigt, dass ALD eine geeignete Methode zur Herstellung qualitativer Modellschichten ist. Sie eignet sich somit sehr gut dafür, den Zusammenhang der Leistungsfähigkeit eines Kathodenaktivmaterials mit der Beschaffenheit seiner

modifizierten Oberfläche systematisch zu untersuchen und somit das Verständnis der Funktionsprinzipien von CAM-Beschichtungen zu fördern. Darüber hinaus wurde ein einfaches nasschemisches Verfahren zur Abscheidung einer Schicht aus Li_3NbO_4-Nanopartikeln und Li_2CO_3 eingesetzt. Diese Schutzschicht ermöglichte eine hervorragende reversible spezifische Kapazität und Ratenfähigkeit (212 und 150 mAh/g_{CAM} bei 0,2 bzw. 2,0 mA/g_{CAM}) sowie Stabilität (mehr als 80% Kapazitätserhalt nach 200 Zyklen) des CAMs. Damit erwies sich diese Schutzschicht als vorteilhaft gegenüber herkömmlichen Lithiumniobat-Beschichtungen, was zeigt, dass es bei nasschemischen Methoden und CAM-Beschichtungen im Allgemeinen noch Potential für Verbesserungen gibt.

List of Abbreviations

ALD	Atomic layer deposition
ATR-IR	Attenuated total reflection-infrared spectroscopy
ASSB	All-solid-state battery
BET	Brunauer−Emmett−Teller
CAM	Cathode active material
CC	Current collector
CVD	Chemical vapor deposition
DEMS	Differential electrochemical mass spectrometry
EDX/EDS	Energy dispersive X-ray spectroscopy
EELS	Electron energy loss spectroscopy
EIS	Electrochemical impedance spectroscopy
EV	Electric vehicle
FIB	Focused ion beam
GPC	Growth per cycle
HAADF	High-angle annular dark-field
HRTEM	High-resolution transmission electron microscopy
ICP-OES	Inductively coupled plasma-optical emission spectroscopy
LIB	Lithium-ion battery
LGPS	Lithium germanium phosphorus sulfide, $Li_{10}GeP_2S_{12}$
LPS	Lithium phosphorus sulfide, Li_3PS_4
LPSCl	Lithium phosphorus sulfur chloride, Li_6PS_5Cl
LSPS	Lithium tin phosphorus sulfide, $Li_{10}SnP_2S_{12}$
LTO	Lithium titanate, $Li_4Ti_5O_{12}$
LZNO	Lithium zinc niobium oxide, $Li_6ZnNb_4O_{14}$
NBED	Nano-beam electron diffraction
NCM	Lithium nickel cobalt manganese oxide, ($LiNi_xCo_yMn_zO_2$)
NCM851005, NCM85	$LiNi_{0.85}Co_{0.10}Mn_{0.05}O_2$
PEDOT	Poly-3,4-ethylene dioxythiophene
PEEK	Polyether ether ketone
PLD	Pulsed laser deposition
PVDF	Polyvinylidene fluoride
ROI	Region-of-interest
SE	Solid electrolyte
SOC	State-of-charge
SEM	Scanning electron microscopy
SSB	Solid-state battery
STEM	Scanning transmission electron microscopy
TEM	Transmission electron microscopy
TEMAH	Tetrakis(ethylmethylamido)hafnium(IV)
TEMAZ	Tetrakis(ethylmethylamido)zirconium(IV)
ToF-SIMS	Time-of-flight secondary ion mass spectrometry
XPS	X-ray photoelectron spectroscopy
XRD	X-ray diffraction

Table of Contents

1 Introduction

Due to their high energy density, reliability and cycling stability, lithium-ion batteries (LIBs) are arguably the most important electrochemical energy storage systems, laying the foundation for portable consumer electronic devices such as smartphones and laptops.[1–5] These have transformed our daily lives by driving global communication and interconnection, computation and navigation, as well as an ever-extending array of applications in commerce and finance, fitness and health-care, entertainment and education etc. However, despite being around since the beginning of the 1990s and only undergoing iterative improvements (unlike exponential trends such as in the semiconductor field), the technology has garnered a more profound new wave of attention from society, academia and industry. LIBs are considered to be an essential part of (inter)national ambitions to reduce greenhouse gas emissions in the transport sector in order to mitigate future risks of the already unfolding climate change.[6] (Battery) electric vehicles (EVs) were still rather niche products a decade ago, but now an international industry is rapidly ramping up production.[7] Several so-called Gigafactories are already producing large numbers of batteries for EVs, and many more such factories are in planning or under construction. And despite the still low market share that EVs have relative to the total number of passenger vehicles today,[7] it can be argued that the technology has already disrupted the automotive industry.[8] Importantly, many (rich) countries have recently introduced legislation or have plans to phase out vehicles powered by an internal combustion engine (ICE) in the not-too-distant future (for example, in 2035).[9,10] One other important factor is that the total cost of ownership of some EVs is already (or might soon be) lower than that of its ICE-powered counterpart. Moreover, owning an EV is much more convenient than it used to be, for example, due to the improving availability of (fast) charging stations.[11] Furthermore, issues such as “range anxiety” and safety concerns are less debated nowadays than a few years ago, signaling the maturing of EVs.

And yet, the cell design that future EVs will be based on is far from being settled. In recent years, the conventional liquid electrolyte (LE)-based LIBs have been constantly developed upon in terms of safety as well as energy and power density to achieve the aforementioned progress. However, this also means that physical limits, for example, regarding the amount of energy that can be stored in a given volume with currently relevant electrode materials such as $\mathrm{LiNi}_x\mathrm{Co}_y\mathrm{Mn}_z\mathrm{O}_2$ (NCM) and graphite will be approached within the next decade or so.[12,13] This has been a driving force for expansive research efforts to realize next-generation concepts such as lithium-sulfur[14] and lithium-air batteries[15] as well as solid-state batteries (SSBs).[12] In SSBs, the organic liquid electrolyte is replaced by a solid electrolyte (SE) that conducts ions (mostly Li^+ so far) and can act as separator layer. Thus, they consist, as their name suggests, solely of solid components, which is why they are occasionally referred to as all-solid-state batteries (ASSBs) to differentiate them from hybrid systems that still contain some amount of liquid.

There are several classes of solid electrolytes, the most important ones being oxides, sulfides and polymers, with halides having drawn much attention recently. Each of these classes of materials has their own advantages and disadvantages which have been summarized in several review articles.[12,16–20] Using solid electrolytes has been connected with the hope that they could potentially enable the use of the Li metal anode, a decades-old quest with the aim to harness ultimate energy densities.[21] The idea behind this is that SEs could suppress the damaging and dangerous Li dendrite growth that has rendered past attempts to realize Li metal batteries unsuccessful.[4] Even anode-free cell designs are currently under investigation. According to this concept, all of the available lithium in a cell originates from the cathode and the anode is generated *in situ*, providing the highest possible energy density.[22] However, the milestone of reliably using Li metal anodes has yet to materialize.[12,23,24] Other potential benefits of SSBs include possibly improved safety (since no flammable and toxic liquid can leak out), potential operation at higher power (due to the fact that they prevent an ion concentration gradient build-up at high current densities), a wider temperature range for operation and a reduced risk of thermal runaways.[12,25]

Sulfides (or more specifically thiophosphates) are widely regarded as the most promising class of SEs to replace the liquid electrolyte.[12] This is based on their high ionic conductivities (up to ~25 mS/cm at room temperature) which can even surpass those of conventional liquid electrolytes (~10 mS/cm).[26] Low bulk ionic conductivities might be prohibitive for the use of an SE in SSBs, since the tortuous pathways of Li^+ ions in composite electrodes (containing active material, possibly carbon additive(s), binder and residual porosity) result in even more limited effective ionic conductivities.[27–29] Another advantage of thiophosphates is their low Young's modulus, meaning that they are malleable and can be processed well (and at low temperatures) into dense composites, which is favorable for large-scale manufacturing.[21]

The main drawback of thiophosphates is their thermodynamic instability in conjunction with essentially all relevant electrode materials (which will be described in the first chapter of this thesis). Firstly, exhibiting a narrow electrochemical stability window, they are reduced at the anode (e.g., lithium metal) and oxidized already at moderate potentials at the cathode.[30–32] Secondly, they undergo severe chemical degradation, for example, at the interface to high-energy-density cathode active materials (CAMs).[30,32] This has led to the early insight that engineering of stable interfaces by introducing a protective layer is essential for the operation of cathodes containing thiophosphate SEs and high-voltage CAMs.[30] Thus, next to realization of the Li metal anode and low-pressure operation, achieving interfacial compatibility is arguably one of the main challenges that need to be overcome before thiophosphate SSBs can be commercialized. Optimizing cathode performance and capacity is of central importance since it is the only cell component that contributes to the energy density of an ideal cell (with an *in situ*-plated Li metal anode).[27]

An appreciable library of CAM coatings for the use in thiophosphate SSBs has been generated over the last decade and a half.[30] The examination of coated CAMs prior to and after cycling has provided insights into the various functionalities that these protective layers can have. An overview over these will be given in the first chapter of the thesis. A common observation is the mitigation of (electro)chemical degradation at the SE|CAM interface, resulting in significantly improved cycling performance, for example, in terms of higher capacity, reversibility, rate capability and stability. CAM coatings can be applied using various chemical and physical deposition methods that differ significantly in the achievable coating quality, cost, ease-of-use etc. The basic principles of the most important methods will be outlined here, as well as recently proposed CAM coating synthesis approaches. Despite the availability of numerous CAM coatings and methods to apply them, the low fading, high reversibility and strong rate performance seen in state-of-the-art LIBs remain elusive when using SSBs. Future progress requires a more systematic understanding of the influence of coating properties on the phenomena occurring during cell operation. This in turn necessitates thorough investigations of surface-modified CAMs, which is often complicated by the morphological and compositional complexity of coatings.

The focus of this doctoral project was on the preparation and characterization of protective oxide coatings for Ni-rich CAMs. These coatings were also extensively tested in SSB cells with the CAM $LiNi_{0.85}Co_{0.10}Mn_{0.05}O_2$ (NCM85), the SE Li_6PS_5Cl (LPSCl) and the anode material $Li_4Ti_5O_{12}$ (LTO). Special emphasis was placed on the use of atomic layer deposition (ALD). The method is capable of producing very thin and conformal films on complex substrates, but had barely been employed in the field of SSB CAM coatings.[30] The results of the studies on ALD-derived CAM coatings are reported on in two publications of this doctoral thesis. A seminal study focused on finding important process parameters to deposit HfO_2 onto NCM85. The method was shown to be a viable tool to deposit high-quality model coatings onto CAMs that show appreciable performance in SSB cells. The follow-up study concentrated on the influence of a post-heat treatment on ZrO_2@NCM85, revealing several overlapping phenomena that occur at different temperatures. These include changes in crystallinity, Zr^{4+} ion diffusion into the NCM and reactions between CAM and coating. Ultimately, a third study represents a continuation of efforts on sol-gel-derived lithium-containing oxide coatings, targeting the compound $Li_6ZnNb_4O_{14}$. Interestingly, these coatings consisted of Li_3NbO_4 nanoparticles and Li_2CO_3 and outperformed conventional lithium niobate coatings, which are regarded to be well-functioning prototype coatings in the SSB field.

2 Fundamentals

2.1 Degradation Processes in SSB Cathodes

Building viable SSBs requires engineering stable interfaces throughout the whole cell. Using lithium thiophosphates (sulfides) is advantageous due to their high ionic conductivity and low-temperature malleability. However, thiophosphate-based electrodes suffer from various types of degradation during cycling, which are summarized in **Figure 1** and briefly outlined in the following, with an emphasis on NCM-based cathodes.

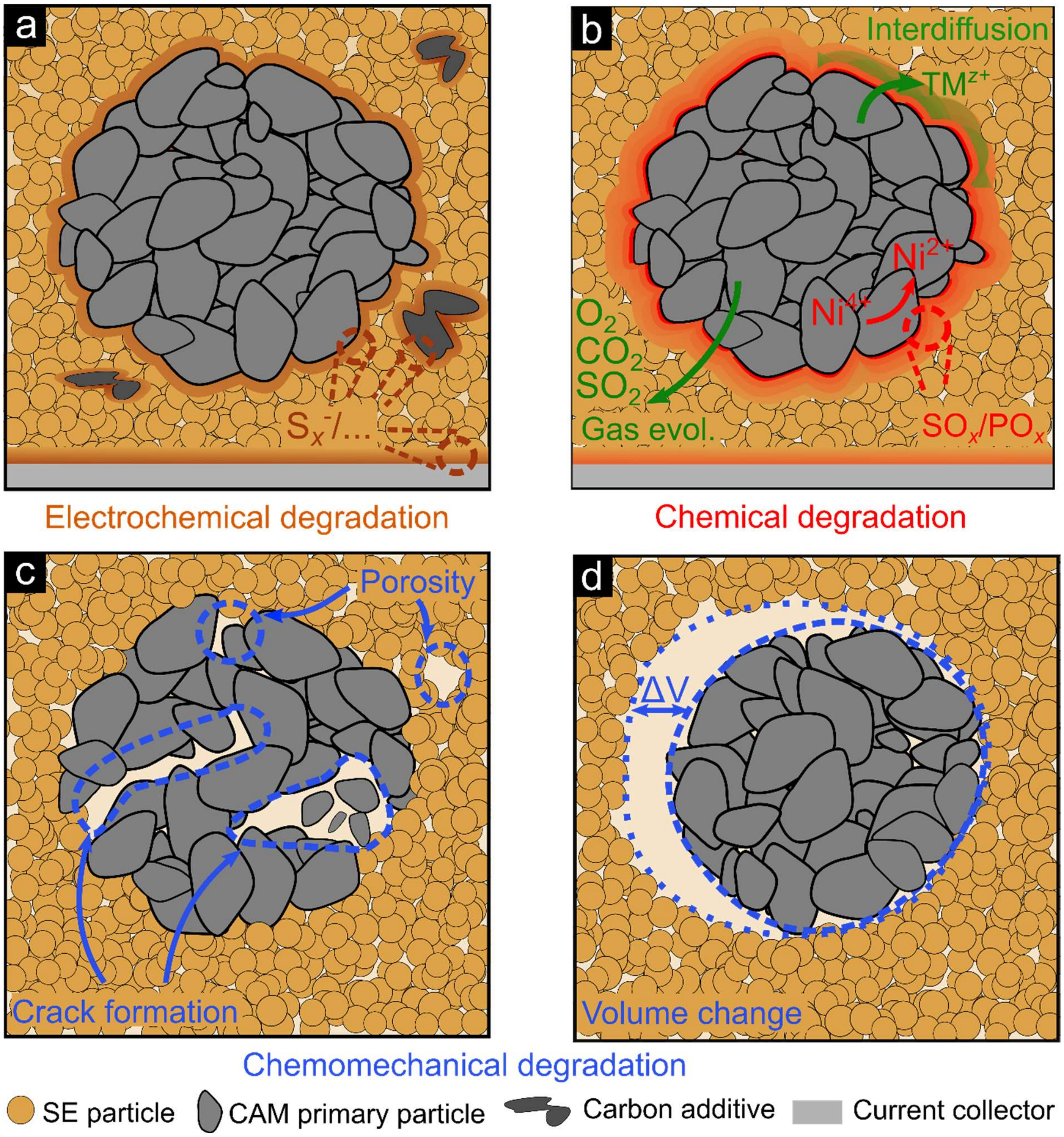

Figure 1: Schematic overview of degradation types in SSB cathodes at the example of thiophosphate/NCM electrodes.

2.1.1 Electrochemical Degradation

High-energy density batteries have to span a wide range in electric potential and electrochemical potential of lithium (see **Figure 2**). However, the use of thiophosphates in SSBs is complicated by their narrow electrochemical stability window.[33–37] This means they are reduced at relatively high potentials (e.g., ~1.7 V vs Li^+/Li in case of LPSCl) and oxidized already at moderate potentials (~2.0 V vs Li^+/Li for LPSCl), if no mitigation measures are taken.[33] While their experimentally observed electrochemical stability window is wider than thermodynamics predict,[33,38] the potentials that relevant electrode active materials (e.g. lithium metal as anode active material, NCM-type materials as CAM) are operated at, are far beyond the stability limits of the thiophosphate SEs.

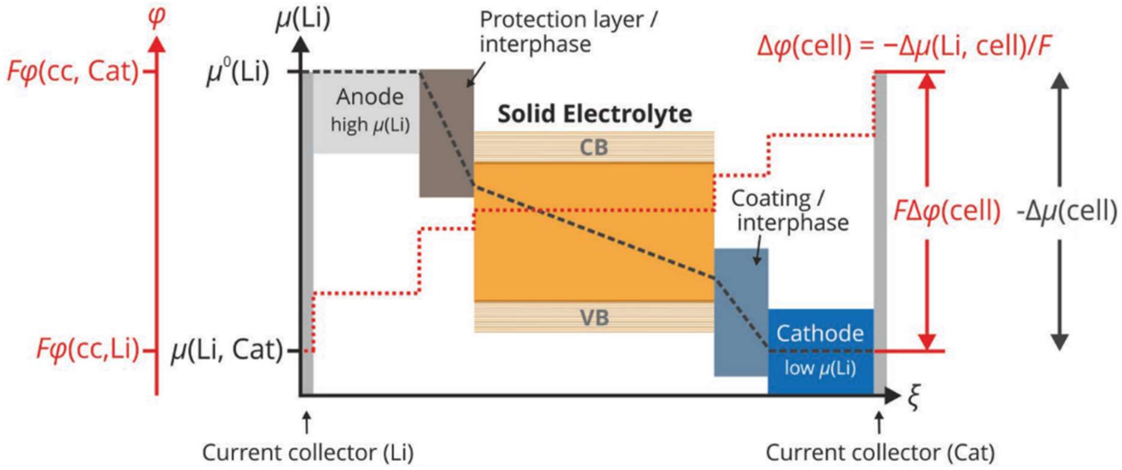

Figure 2: Potential profile in a solid-state battery cell. φ (red) and μ (black) represent the electric potential and the chemical potential of Li (in the neutral state), respectively. Reproduced from Culver *et al*.[30]

As a result, electrochemical degradation (oxidation) takes place at all contacts of the SE with electronically conductive materials within or at the surface of the composite cathode. Specifically, this concerns conductive (carbon) additives,[39,40] the current collector (CC)[41] and the CAM (**Figure 1a**).[40,42] Products of such oxidative degradation processes comprise a wide range of materials and depend on the used SE. The oxidation state of the phosphorus and sulfur increases as the degradation proceeds. Among the decomposition products are LiCl, Li_2S, polysulfides (e.g. Li_2S_x) and P-$[S]_x$-P-containing compounds (having a polymerized PS_4^{3-} unit).[41,43,44] Some of these deleterious redox reactions are partially reversible.[41,44] Still, significant amounts of oxidation products remain in the discharged state. This is problematic because of the low ionic conductivity of some of these compounds (e.g., Li_2S, LiCl) that leads to increasing interfacial resistance and consequentially a decline in SSB performance upon accumulation at the interfaces mentioned above.[41]

Especially in early works on SSBs, problems with interfacial Li-ion transport were assumed to result from the formation of a space charge layer.[30,32,45] This describes a

Li-deficient layer that forms to maintain charge neutrality when electrons migrate from (sulfide) SEs to the cathode, i.e., upon oxidation. The effect was thought to be pronounced, since no opposing space charge layer accumulates in the CAM (mixed conductor), leading to extensive Li migration from sulfide to oxide.[46] However, there is little experimental evidence for the space charge layer, and it has been argued that its effects were probably overestimated at the expense of the probably more important oxidative decomposition of sulfide SEs.[30,32,47]

2.1.2 Chemical Degradation

While chemical reactions can occur at the SE|carbon and SE|CC interfaces due to functional groups (impurities) at the surface of these components,[48] the major share of this type of degradation takes place at the SE|CAM interface (**Figure 1b**).[36,37,42–44,49] A wide range of possible products results from such reactions. Again, they depend on the used CAM and SE materials. However, one common observation is the presence of oxygenated sulfur and phosphorus species revealed using XPS and/or ToF-SIMS.[39,42–44,49,50] This corroborates theoretical predictions stating that these are energetically favorable products of the reaction between sulfides and oxides.[34,36,37] In fact, the formation of SO_x and/or PO_x species has been predicted and observed to take place upon mere contact of a thiophosphate SE and a layered oxide.[36,51,52] As mentioned above, the CAM represents the only source of oxygen, so the oxygenation of the SE mainly occurs at the SE|CAM surface.[49] The CAM (specifically the transition metal cations in the CAM) is reduced in turn, leading to the formation of rocksalt-like phases at and below its surface.[53,54] The negative effects of such resistive phases on the cycling performance of layered oxide CAMs is well-documented, especially for LIB cells.[55,56]

In the recent years, a number of studies reported gas evolution from SSB cathodes using differential electrochemical mass spectrometry (DEMS), an *operando* gas analysis technique already established for LIBs.[50,57–63] Typically, the most prevalent gaseous degradation products in thiophosphate|NCM-cathodes are CO_2, O_2 and SO_2.[57,58] CO_2 stems from the common Li_2CO_3 residues on NCM CAMs which are electrochemically decomposed starting at ~4 V vs Li^+/Li. C-containing CAM coatings could also act as a source for CO_2.[57] O_2 originates from the lattice of the layered oxide that becomes unstable at high SOCs (approximately ≥ 80%), with some of the oxygen being present as highly reactive $^1O_2$.[57,64] Conceivably, a part of the evolved oxygen subsequently reacts with the SE, forming the SO_x species mentioned above. Among those, the gaseous SO_2 has been detected using DEMS.[50,57–63] Notably, H_2S, a flammable and toxic gas forming upon the reaction of thiophosphates with (trace) water, has not been observed in the mentioned gas analysis studies.

Another mode of chemical degradation is interdiffusion. While it is usually slow for multivalent cations, it can take place more rapidly at increased temperatures and during electrochemical cycling. Indeed, interdiffusion has been reported to occur in SSBs. For example, the mutual interdiffusion of Co, P and S between $LiCoO_2$ and Li_2S-P_2S_5 could be observed using transmission electron microscopy (TEM)-based energy-dispersive X-ray spectroscopy (EDS).[65] Similarly, recent TEM-EDS investigations on cycled LPSCl|NCM85 interfaces showed a non-negligible Ni content within the SE.[54] Furthermore, a number of studies suggest the (theoretically predicted)[36] formation of transition metal sulfides based on XPS.[52] However, uncertainties remain about their presence in cycled cathodes due to the complicated detection of the typically low quantities of (minor) degradation products. It has been argued that they represent intermediate phases which in turn react towards the compounds with higher oxidation states mentioned above.[40] It should be noted that electronically conductive degradation products, such as (lithium) transition metal sulfides, lead to further (electro)chemical degradation instead of enabling passivation.[36,37]

Empirical studies have shown that the degree of degradation increases with progressing SSB operation. For example, growing amounts of oxygenated degradation products with increasing cycle number have been reported.[49] Recently, the suggested time dependence could be specified to be based on a diffusion-controlled mechanism according to the Wagner model.[51] In connection with this, the (electro)chemical decomposition has been shown to follow a parabolic rate law.[51] Importantly, this means that degradation slows down with time, but does not stop completely. The study also showed that the SOC of the CAM (NCM622 in the example) determines the driving force for degradation of the SE ($Li_{10}GeP_2S_{12}$, LGPS), meaning that cycling to higher cut-off voltages (and therefore to a higher degree of CAM delithiation) increases the rate of degradation.[51] While it increases gradually with raised cut-off voltages up to 4.2 V vs Li^+/Li, there is a drastic acceleration of the degradation at 4.3 V and above. It is argued that this results from a change in the degradation pathways/products. While the formation of electrochemically oxidized species such as polysulfides takes place already at relatively low SOC, an accelerated degradation connected to the oxygenation of the SE is a consequence of high CAM SOC.[51] As mentioned above, oxygen is released from the lattice of the layered oxide CAM, leading to SE oxidation and potentially the formation of rocksalt-like phases during this regime. It should be mentioned that this type of degradation can already take place while the average CAM SOC is below the threshold for the deleterious oxygen release. This is due to the inhomogeneous SOC/degree of delithiation of the CAM, which is not unusual in SSB cathodes.[62]

The interfacial degradation is governed by the chemical diffusion of lithium through the degradation layer according to the Wagner model, and the interfacial layer should be predominantly ionically conducting and electronically insulating. Thus, electronic conduction is presumably the rate-limiting process of degradation. Therefore, electronic conduction is assumed to determine the activation energy in this Arrhenius-type process, and therefore the rate constant of degradation. Summing up, the (electro)chemical degradation at the SE|CAM interface is a complex process that is governed by multiple factors, including time, SOC and temperature.[51]

2.1.3 Contact Issues and Chemomechanical Degradation

Chemomechanical degradation and its prevention play an especially important role for SSBs. Since such cells are by definition constituted exclusively by solid components, appropriate contact at all relevant interfaces, including those within the cathode, is not as naturally achieved as in the case of conventional LIBs. This is because a solid electrolyte cannot infiltrate small pores or cracks (see below) of the CAM. Grain boundaries of the SE itself and residual porosity in such a cell represent further hindrances for ion conduction (**Figure 1c**).[27] So far, it has been a widely followed practice to fabricate thiophosphate SSB cells using high (mostly uniaxial) pressures, typically on the order of hundreds of megapascals. Also, such cells have to be operated under pressures up to tens of megapascals.[66] While it is an advantage over oxide SEs that thiophosphates can be cold-pressed (and do not need to be sintered at high temperatures) to achieve sufficient contact within a cell, reducing the required external pressure during cycling to a minimum still poses one of the main challenges for (thiophosphate) SSBs.[21] A typically followed strategy to address this issue is the use of polymer binders in composite electrodes.[59,60]

Interfacial chemomechanical degradation is mainly caused by the volume changes of electrode active materials during battery operation (**Figure 1d**). During charging and discharging, the lithium content in the electrodes changes constantly, leading to volume changes since the molar volume of most active materials depends (sometimes strongly) on their lithium content. This applies to solid solutions, but is especially pronounced if a change in lithium content induces phase transitions. For example, layered NCM-type CAMs initially exhibit a volume increase due to reduced shielding of the electrostatic repulsion of neighboring oxygen atom layers due to partially emptied lithium layers. However, when reaching a sufficiently high SOC, the almost empty lithium layer collapses, resulting in a sharp reduction in unit cell volume.[67,68] Overall, a net shrinkage of a few percent occurs during charging (delithiation) of Ni-rich NCM CAMs. Within a relatively rigid matrix of a cold-pressed thiophosphate SE, this can lead to contact loss at the SE|CAM interface.[69] On the other hand, volume increase of active materials leads to stress build-up in the CAM particles and the electrode overall.[70] Different strategies have been proposed on how to mitigate this problem such as selecting NCM materials with appropriate Ni and Co contents that exhibit minor net volume changes upon cycling (“quasi-zero-strain materials”) or material combinations whose opposing volume changes cancel each other out.[71,72] These approaches evidently alleviate stress/pressure build-up on a macroscopic scale. However, the extent of the volume change is not the only parameter determining mechanical degradation. Especially the anisotropic nature of the volume change has been shown to cause interparticle fracture in secondary particles.[13,67,73,74] All of the above processes lead to increasingly tortuous pathways for Li-ion conduction and can result in complete contact loss of some parts of the electrode (i.e., inactive material and capacity decline).[75]

As mentioned previously, the different degradation phenomena partially occur in parallel and influence each other. That is why their contributions to performance decay in SSBs can be challenging to deconvolute and quantify.[60,75,76] The interplay between chemical and electrochemical reactions has been discussed above. It is further exemplified by the competing formation of polysulfides versus oxygenated sulfur species depending on the presence of a conductive carbon additive.[40] While S_x-type compounds dominate with conductive carbon, SO_x species are the main degradation products when no such additive is used. There are also several examples for the connection between (electro)chemical and mechanical phenomena. For example, Han *et al.* have recently demonstrated how local stresses resulting from SE decomposition drive the disintegration of secondary particles in polycrystalline layered CAMs.[77] Vice versa, another recent study has shown that the physical separation of a CAM and its protective coating can lead to locally pronounced oxygen release from NCM materials.[78] For optimal SSB functioning, ideally all of the above degradation phenomena should be addressed. One of the most important strategies to stabilize SSB cathodes are CAM coatings whose functionalities will be discussed in the following section.[30]

2.2 Working Principles of Cathode Active Material Coatings

Due to the various instabilities in thiophosphate-based cathodes outlined above, the essential need for CAM coatings is obvious. Such protective coatings have been developed and investigated for a considerable time now and probably will be for years to come.[30,32] By now, there is a wide range of investigated compounds and methods to apply them, which will be discussed in the following sections. In this section, a few general considerations about coatings are briefly summarized, and it will be outlined how they alleviate different degradation processes in thiophosphate SSBs. These aspects are schematically depicted in **Figure 3**.

When introducing a protective layer, the direct interface of SE and CAM is substituted with SE|coating and coating|CAM interfaces. Therefore, a coating must obviously not react in an adverse way with either of the two interfaced components. This includes that coatings need to be reasonably stable at the high potentials that are typically prevalent in connection with currently relevant CAMs such as Ni-rich NCMs. This is one of the main reasons why oxides have been the most widely used materials for this purpose.[30] In principle, a better understanding of the working principle of coatings would require an independent examination of both artificially created interfaces. However, considering the nanoscale dimensions of coatings, such differentiated insights are difficult to obtain.

2.2.1 Suppression of Electrochemical Side Reactions

It could be argued that the suppression of (electro)chemical decomposition reactions at SE|CAM interface has been the main aim of past and present attempts on CAM coatings. By creating a physical barrier at this interface, the SE is aimed to be shielded from the high potential of the cathode (i.e., the low chemical potential of lithium in the CAM; **Figure 2**). This in turn suppresses or reduces degradation and therefore interfacial resistance growth (**Figure 3a**). However, coatings should be ionically conducting and electronically insulating. In other words, an ideal coating should function like a stable solid electrolyte.[30] However, electrons have to migrate into and out of CAM particles for lithiation and delithiation, respectively. Hence, a compromise regarding the electronic partial conductivity of the interfacial layer needs to be reached. Based on theoretical considerations, a recently proposed guideline stated that the electronic conductivity of the coating layer has to be lower than that of the SE. This in turn would help to create a sufficient potential drop at the interface to effectively protect the SE from oxidative decomposition.[47] Naturally, CAM coatings can only reduce degradation at the corresponding interface. This needs to be considered when interpreting the presence of degradation products (that still form at the SE|CC and SE|carbon interfaces) in cycled composite cathodes.[40]

2.2.2 Influence of Coatings on Interfacial Reactions and Interdiffusion

Similar to electrochemical side reactions, coatings are supposed to limit chemical reactions by preventing the physical contact between the incompatible cell components. Indeed, a typical observation, often made when investigating cycled cathodes by XPS and/or ToF-SIMS, is that there are reduced amounts of degradation products when a CAM coating is used.[30,49,61–63] However, the formation of degradation products has not yet been fully suppressed by any coating compound/method. One likely reason for this is the reaction of O_2 (evolved from the CAM at high SOC) with the SE. It seems unlikely that a coating can be (and remain) sufficiently leak-tight to prevent gases from reaching the SE. However, it could be a strategy to add sacrificial components to a coating whose reactions with the evolved O_2 are less adverse for cell performance than those with the SE.

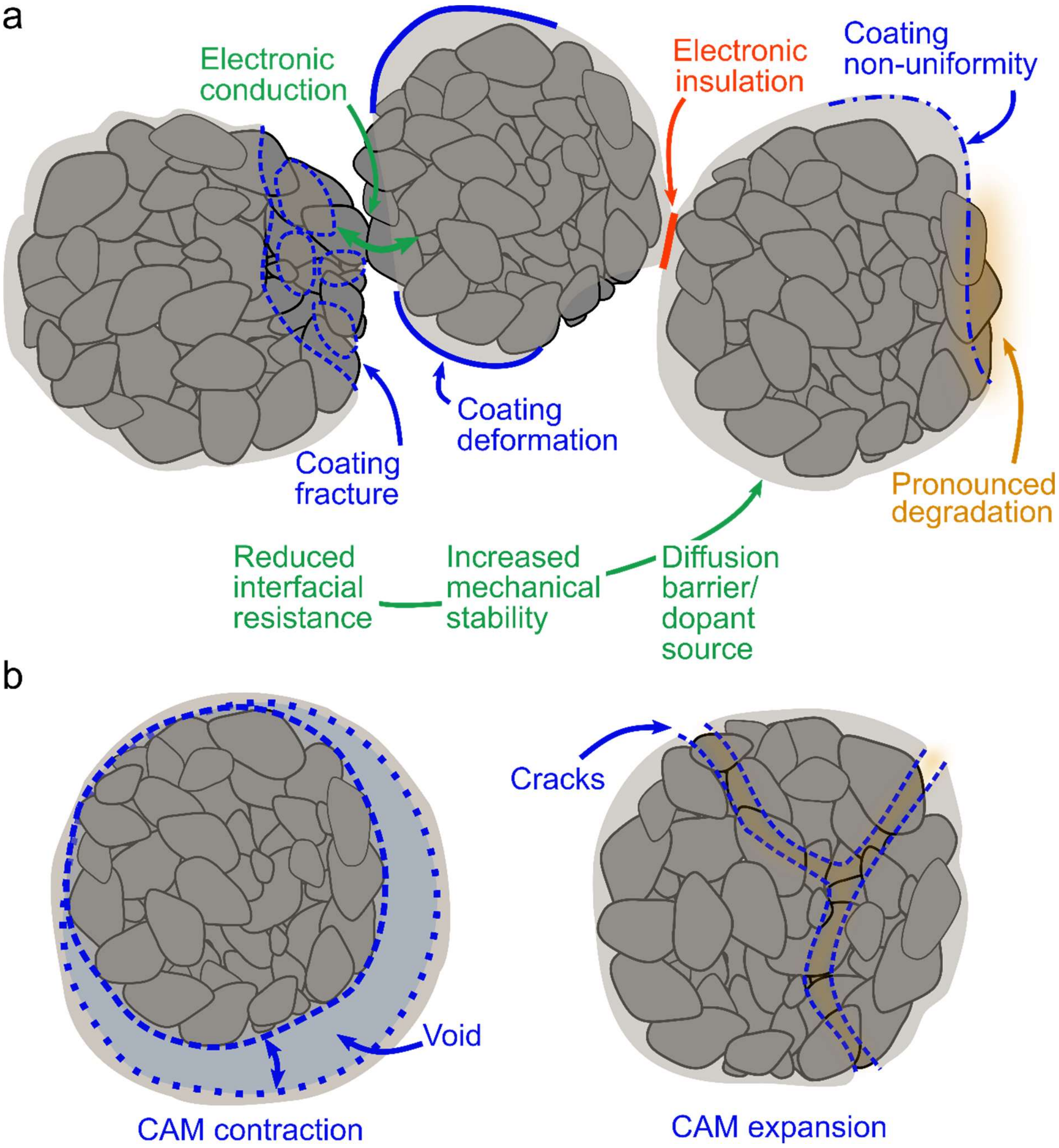

Figure 3: Schematic overview of the functions, morphological and mechanical aspects of CAM coatings. a) Influence of coating coverage on interfacial degradation and the electronic contact across CAM particles. b) Mechanical failure modes of CAM coatings resulting from volume changes. Adapted from Culver *et al.*[30]

As mentioned above, interdiffusion happens as soon as solids are contacted, so they play a role in SSBs as well (**Figure 3a**). There are a few reports that assess coating functionality with regards to this phenomenon.[54,65,79–81] For example, the mutual interdiffusion of Co, S and P across a Li_2S-P_2S_5|LCO interface was reduced by the introduction of a Li_2SiO_3 layer.[65] The authors attributed lower interfacial resistance to reduced interdiffusion and the consequently reduced structural degradation. However, elsewhere it has been shown that, after high numbers of charge/discharge cycles, interdiffusion takes place despite the presence of a coating layer.[80] Interdiffusion between coating and CAM during synthesis also plays an important role for SSB performance and will be discussed in the next section.

2.2.3 Morphological and Mechanical Aspects of CAM Coatings

Any aspect of CAM coating functionality is influenced by its morphology and mechanical integrity (**Figure 3**). Obviously, only actually covered CAM surface regions can benefit from the protecting nature of the artificially introduced surface layer. There are several scenarios in which a CAM surface can be exposed, despite the fact that a coating was applied (**Figure 3a**). First of all, every coating has, depending on the deposition method, some degree of non-uniformity, which includes the existence of gaps in the protective layer. Eliminating the possibility of any uncovered spots might require the use of excessive amounts of coating material. However, this is unattractive since too thick coatings often negatively affect interfacial charge transfer and thus SSB performance. Secondly, coating fracture and deformation upon battery assembly (due to composite mixing or electrode compression) or during operation (due to repeated CAM volume changes) lead to exposed areas of the CAM surface. On the one hand, the aforementioned (electro)chemical SE decomposition processes will take place primarily at these unprotected spots. On the other hand, in case of strongly electronically insulating layers, imperfections (at the contact points of CAM particles) might be necessary for electronic percolation.

As mentioned in the previous section, volume changes of the CAM are among the main degradation processes in SSB cathodes. **Figure 3b** shows how they can also damage the coating and reduce its contact area with the CAM. Contraction of the CAM can lead to void formation and, therefore, contact loss in case of an inflexible coating. Several reports have shown the segregation (sometimes referred to as exfoliation or delamination), aggregation and ”breakdown” of a coating.[78,82] Apart from the contact loss, such separation has been suggested to initiate locally pronounced oxygen loss from the CAM.[78] Moreover, CAM expansion could, as mentioned above, lead to crack formation in a brittle coating. It has been claimed that coatings can (physically) confine growth of secondary particles.[83] However, estimations have shown that a nanometer-thick coating cannot confine such a bulk expansion.[30] Nevertheless, the presence of a coating might still reduce the extent of crack formation at the primary particle grain boundaries. A recent study indicates that mechanical stabilization can result indirectly from the reduction of (electro)chemical SE oxidation.[77] The authors argue that high local stresses are caused by the volume change the SE undergoes as it decomposes, promoting the fracture of polycrystalline CAM secondary particles.

2.2.4 Interpreting and Improving Coating Functionality

Overall, there is no shortage of evidence that CAM coatings improve SSB performance in a multitude of ways.[30,32] Generally, it seems that coatings rather slow down the degradation in SSB cathodes than fully suppress it. This would, for example, explain the reduced amount of SO_x/PO_x species after a given number of cycles when using a CAM coating. However, often it is not unlikely that the level of degradation seen for bare CAMs would be reached equally for coated CAMs, just at a later stage of cycling. The goal of applying coatings might therefore be to reduce the degradation rate to an extent that allows for acceptable lifetimes of the corresponding cathodes.

The analysis and understanding of the functionality of CAM coatings is challenging.[49] Not only all the (partially suppressed) degradation processes have to be considered, but also the additional interactions involving the coating and its imperfections have to be taken into account. Moreover, the analytical requirements for thorough analysis of the coating and all its relevant functions are high. They include (but are not limited to) high resolution, inert conditions, the necessity to examine interfaces which are difficult to access and possibly *operando* approaches.[62] Even if all the relevant effects of the protective layer are correctly identified, a quantitative attribution to the superimposing phenomena that collectively determine the performance (benefits) of a coating remains hard to achieve. In any case, the use of complementary analysis techniques is required for the characterization of the modified CAM both in the pristine and cycled states. Furthermore, it might be useful to revisit compositionally “simple” or established model coatings to reduce complexity. Moreover, it should be valuable to use appropriate reference samples, for example, prepared by another coating method. Also, sets of samples obtained by varying parameters such as temperature or composition should be used. All this could help improve understanding of the occurring phenomena and facilitate the identification of the most important aspects that should be targeted when designing novel coatings.

2.3 Coating Methods for Cathode Active Materials

The previous chapters have explained why a protective layer between CAM and SE is essential and what its functionalities should ideally be. How (well) a coating works is not only determined by the compounds it is made from, but also by its thickness, morphology etc. These characteristics are controlled to a large extent by the used coating method/parameters. To date, a considerable number of techniques to deposit coatings on CAMs have been reported, each having advantages and disadvantages.[30] A survey of the recent literature on CAM coatings is provided in the following section, including explanations of approaches that are new for this application. In this chapter, two important methods employed in the publications of this thesis are described.

2.3.1 Wet Chemical Methods

All wet chemical methods involve the use of a solution containing appropriate amounts of coating precursors/constituents in which the CAM is suspended. Then a certain period of mixing (e.g., by stirring/ultrasonication) follows, during which the suspension is sometimes heated slightly. Subsequently, the solvent (including the unreacted precursor compounds) could be removed by filtration or the solvent is removed directly in vacuum. Sometimes this is carried out at slightly increased temperatures (60 °C or similar) and with the suspension being agitated. Usually, the resulting dry powder is then calcined in oxygen/air to remove residual organics and obtain the desired properties of the protective layer, which is described in more detail below. This facile process sequence is rather common[30,54,63,84,85] and has been referred to as slurry-based/dispersion/solution coating method.

There are wet chemical methods that promote (a more uniform) adsorption/deposition of the coating precursors on the CAM surface to improve the conformity of the resulting surface layer. The most common example for this is the sol-gel technique, which involves the transition of a colloidal liquid (sol) into a viscoelastic solid (gel).[86] It is based on the use of metalorganic compounds (often alkoxides, since they readily react with water) that undergo a series of hydrolysis and condensation reactions. Hydrolysis reactions take place between metalorganic species and H_2O (see **equations 1**, **2**)

$$\mathrm{M(OR)}_z + x\,\mathrm{H_2O} \rightarrow \mathrm{M(OR)}_{z-x}\mathrm{(OH)}_x + x\,\mathrm{ROH}, \qquad (\mathbf{1})$$

$$\text{e.g., } \mathrm{Nb(OEt)}_5 + x\,\mathrm{H_2O} \rightarrow \mathrm{Nb(OEt)}_{5-x}\mathrm{(OH)}_x + x\,\mathrm{EtOH}, \qquad (\mathbf{2})$$

where *z* is the valence of the metal M and R is an organic ligand. M-O-M bonds can then be formed via polycondensation of partially hydrolyzed metalorganic species, i.e., nucleophilic substitutions (see **equations 3**, **4**),

$$n\,\mathrm{HO} - \mathrm{M(OR)}_{z-1} \rightarrow \mathrm{HO} - (\mathrm{Nb(OR)}_{z-2} - \mathrm{O})_{n-1} - \mathrm{Nb(OR)}_{z-2} - \mathrm{OH} + (n-1)\,\mathrm{ROH}, \qquad (\mathbf{3})$$

$$\text{e.g., } n\,\mathrm{HO} - \mathrm{Nb(OEt)}_4 \rightarrow \mathrm{HO} - (\mathrm{Nb(OEt)}_3 - \mathrm{O})_{n-1} - \mathrm{Nb(OEt)}_3 - \mathrm{OH} + (n-1)\,\mathrm{EtOH}, \qquad (\mathbf{4})$$

where *n* is the number of monomers forming a polymer. Depending on the degree of hydrolysis of the monomers (and the corresponding number of –OH groups), branching of the polymer takes place. By this, a three-dimensional network of metal-oxygen bonds is formed, which can have side chains, crosslinks, rings etc., depending on the reaction conditions (e.g., the water concentration in the mixture). This network grows within the sol until a gel is formed. The gel point is defined as the time when a macromolecule extends through the whole solution. Therefore, the gel can be described by a "solid skeleton enclosing a liquid phase".[86] Since the CAM particles are present in the liquid during polymerization, which exhibit hydroxyl groups and usually moisture that can start the hydrolysis and polymerization, they are covered by the metal ion-containing gel. The properties of the gel depend strongly on the reaction conditions and have an effect on the resulting surface layer when the gel-covered CAM is dried and calcined. Hence, a robust coating process necessitates control over parameters such as CAM water content, precursor concentrations, temperature etc.

Both aforementioned approaches are popular due to their low cost (no expensive or complicated equipment is required) and have enabled the relatively facile application and testing of different coating chemistries. However, they are considered to be limited in terms of uniformity, scalability and reaching very low thicknesses. Notably, spray coating, an already commercialized technique, which is another subtype of the wet chemical methods has advantages in this regard. It is based on transferring the CAM powder from a packed into a fluidized state (also referred to as fluidized bed) and spraying the dissolved precursors onto the particles, which allows for reproducible and scalable CAM coating processes. However, in contrast to the aforementioned laboratory-scale methods, spray coating requires the respective equipment and cannot be used for coating small batches of material.

2.3.2 Atomic Layer Deposition

A method that is particularly suited to fulfil the aforementioned requirements for SSB CAM coatings regarding thickness, uniformity etc. is atomic layer deposition (ALD). ALD is a technique to deposit thin films on various substrates by a series of gas-solid reactions.[87–92]

2.3.2.1 Basic Principles of ALD

Developed as atomic layer epitaxy in the 1970s,[93] it is now a well-established and commercialized technique used to deposit a vast library of compounds for a diverse range of applications, including semiconductors, photovoltaics and increasingly also batteries.[94] ALD processes are performed following a cyclical sequence of two (or more) precursors reacting with a solid substrate. These reactions are often referred to as subcycles. They result in the deposition of a film with binary (or multinary) composition. **Figure 4** schematically depicts an idealized ALD process. Importantly, the essential and unique feature of ideal ALD processes is the self-limiting characteristic of all reaction subcycles.[88] In an ALD reactor, vaporized precursors are carried by an inert gas such as N_2, which is pulsed sequentially into a reaction chamber. There, the precursors react with a substrate until saturation is reached, i.e., when all available surface sites have reacted with precursor molecules. After any reaction subcycle, all unreacted precursor species and side products are purged out of the reactor using the carrier gas.

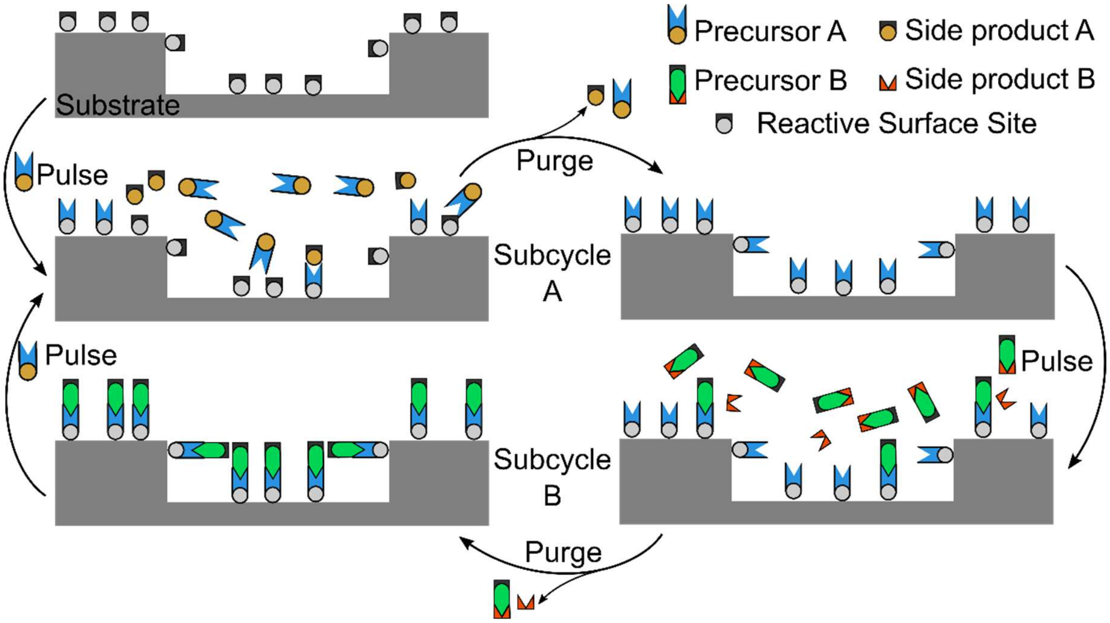

Figure 4: Schematic depiction of an ALD process with two precursors. A substrate naturally has or is treated to have a certain number of reactive surface sites. In subcycle A, precursor A reacts at these sites in a self-limiting manner, depositing half a monolayer of material and forming the side product A. The unreacted precursor A molecules and side product species are removed completely during the subsequent purging step using an inert carrier gas. Starting subcycle B, precursor B is introduced into the reaction chamber and reacts with the surface, forming side product B. Again, all gaseous species are removed from the reactor in a purging step. This ALD (super)cycle is repeated until the desired film thickness is obtained. Adapted from Puurunen[93] and Johnson *et al.*[87]

This process design prevents gas phase reactions between the precursor molecules that would lead to chemical vapor deposition (CVD)-type growth. It also enables bottom-up film formation in sub-nanometer steps with unmatched levels of homogeneity and conformity of deposited films, even on complex substrates. Furthermore, the possibility to adjust numerous process parameters such as temperature, the number of ALD cycles, pulse/purge durations etc., allows for a high degree of control over thickness, composition and other film properties.

Despite the fact that it is a well-established and commercially used technique, there are still some misconceptions and inconsistent terminology that sometimes lead to wrong expectations of the capabilities of the method.[93] To name a few, it is rare that full monolayers of atoms/molecules are deposited (which might be suggested by the name “atomic layer deposition”).[90,93] Among other reasons, steric hindrance between the ligands of precursor molecules prevents that all active sites are reacting.[90]

Notably, even the meaning of term “monolayer” can vary. One reason is that it does not distinguish between chemisorption and physisorption. Another example is that monolayers of/on amorphous, single- or polycrystalline materials would clearly differ.[93] Secondly, growth does not always take place in a layer-by-layer fashion (Frank-van der Merwe growth), but can also occur via islands (Volmer-Weber growth) or randomly.[93] Moreover, growth per cycle (GPC), which describes the amount of material deposited in a full ALD cycle, does not have to be constant as the deposition progresses. In other words, the total amount of deposited material does not have to be proportional to the number of ALD cycles carried out. For example, initial nucleation on the substrate could be delayed, meaning that the GPC increases as the ALD process progresses.[93] Vice versa, a linear increase in deposited material as a function of the number of cycles is not a sign that actual ALD growth takes place. This could also result from non-saturated reactions or CVD-type growth.[88] Furthermore, the notion that a so-called temperature window with constant GPC would exist for every ALD process is not true. This window refers to a temperature range combining appropriate reactivity precursor stability. However, even within such a window, the GPC varies due to the different number of available reactive surface sites.[88] Again, vice versa, windows of constant GPC can actually occur for non-ALD processes such as CVD.

2.3.2.2 Issues Preventing Ideal ALD

There are numerous issues preventing ideal ALD, which explains the large discrepancies of literature results for what should be identical processes.[88] First of all, there are various equipment-related problems. Since ALD precursors are usually very reactive, any exposure to air, dust, humidity etc. by leaks, malfunctioning valves and cold spots (acting as so-called virtual leaks) can severely alter deposition processes and damage the equipment. Moreover, cross-contamination between different processes in the form of precursor and substrate residues (especially when powders are coated in the ALD device) must be avoided.[88] This might sound trivial, but in typical research settings a single ALD device is used by many scientists for various processes. Some of the aforementioned issues might also not be obvious and their cause can be hard to detect and/or address. Another source of inconsistency are suboptimal process parameters such as insufficient pulse or purge times. Among other aspects, these depend strongly on the substrate. For example, porous substrates naturally require longer precursor exposure and removal durations. This is because reactants and side products need to be transported through the substrate interior. Conversely, too long purge durations could, in some cases, lead to desorption of molecules or amplify problems related to (virtual) leaks. Apart from that, various precursor- and substrate-related problems may occur in ALD. For example, precursors could damage the substrate. Also, precursor decomposition could result from the reactor temperature or might be catalyzed by the substrate or the deposited material.[88] Moreover, some substrates might not be conducive (or completely incompatible) for nucleation of certain films, which must be considered to avoid erroneous conclusions about the GPC.[88]

2.3.2.3 ALD for LIB Applications

Based on the need for thin and high-quality protecting layers in batteries and the intensification of research on electrochemical energy storage, it might not come as a surprise that ALD has been applied in this field increasingly often. Apart from the aforementioned advantages of the method, ALD does not require any solvents to produce coatings. At first, the method was mostly employed to improve conventional LIBs.[94–98] However, ALD has also already been used to stabilize the anode|SE interface in SSB cells.[99] For example, an ALD-derived alumina layer improved the wetting properties of the garnet SE $Li_7La_{2.75}Ca_{0.25}Zr_{1.75}Nb_{0.25}O_{12}$ and strongly suppressed interfacial impedance growth with lithium metal.[100] Moreover, several Li-M-O-based thin films (with M = Nb,[101] Ta[102] and P[103]), which are promising for the application as CAM coatings in SSBs, have been reported.[99] However, until recently, only in few studies ALD-derived CAMs were actually applied in bulk-type SSB full cells.[30,79,99] For example, in a seminal study, Woo *et al*. reported the increased stability of a $Li_{3.15}Ge_{0.15}P_{0.85}S_4$|LCO interface when an ALD-derived alumina layer is used.[79] Recently, more studies on ALD for SSB CAM coatings were published, including two parts of this thesis project. These approaches are summarized in **Table 1** in the next section.

2.3.2.4 ALD of Hafnia and Zirconia Films with Alkylamide Precursors

In two of the publications of this thesis, HfO_2 and ZrO_2 were coated on Ni-rich NCM, characterized, and tested in high-loading LPSCl-based SSB cells. For this, precursors with alkylamide ligands were used that have been shown to enable a relatively low process temperature of 250 °C, as well as fast, irreversible and self-terminating reactions resulting in smooth films with low impurity levels. Additionally, their handling is facilitated by the fact that they are liquid, have appreciable vapor pressure and form less corrosive side products than the respective chloride precursors.[104,105] Generally, a similar mechanism is assumed for the Hf and Zr systems.[104] **Figure 5** shows possible reaction mechanisms for the established HfO_2-ALD processes involving the precursor tetrakis(ethylmethylamino)hafnium(IV) (TEMAH) and the oxidants H_2O or O_3.[106]

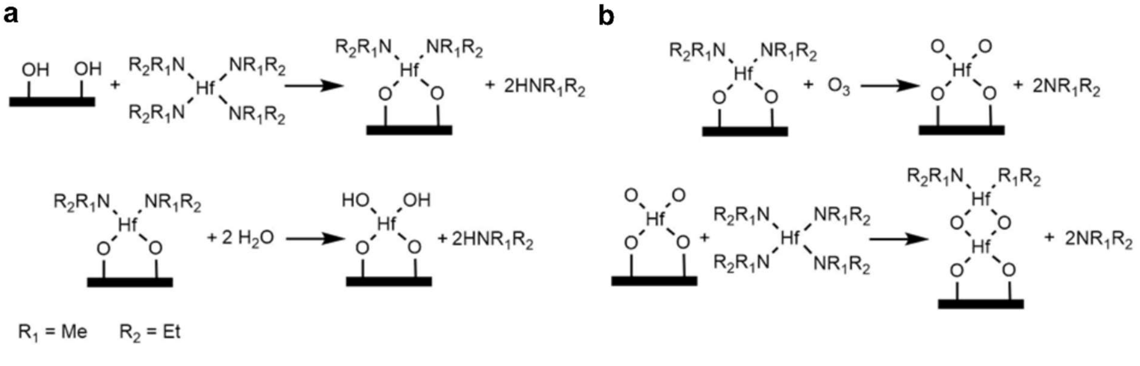

Figure 5: Possible reaction mechanisms for the deposition of HfO_2 using the precursor TEMAH and the oxidants a) H_2O and b) O_3. Adapted from Liu *et al*.[106]

In both cases, the process starts with the reaction of TEMAH with surface hydroxyl groups, breaking the Hf-N bond and forming an Hf-O bond plus ethylmethylamine. In the water-based process, H_2O reacts with the surface-bound hafnium amides and cleaves the remaining ligands to form a hydroxylated surface, which can react with a TEMAH molecule in the next cycle. The so-called combustion in the O_3-subcycle is more complicated and different mechanisms have been proposed. Originally Liu *et al*. hypothesized that most metal alkylamide surface species are cleaved by the highly reactive O_3 at the Hf-N bond, leaving –O· radical surface species behind.[106] Elsewhere, it has been argued that such a reaction would directly produce –OH groups.[107,108] The formed ligand radical is further oxidized by ozone to final products such as CO_2, H_2O, CH_2O, NO_2 and CH_3CN.[106,108] Furthermore, direct cleavage of C-H and C-N bonds is conceivable as well. Notably, using ozone does not eliminate water from the reactor, but its amount is significantly lower in this case. Moreover, the surface is partially hydroxylized by the formed H_2O after the cleavage of the amide ligands. In the next cycle, $Hf(NEtMe)_4$ molecules can then react with the –O· and –OH species. The deposition rates of HfO_2 and ZrO_2 are ~0.1 nm/cycle in the aforementioned processes. A different mechanism for $Zr(NEtMe)_4/O_3$ with long O_3 exposure durations was found to enable higher GPC values of 0.18 nm/cycle (initially) and 0.28 nm/cycle (after 47 cycles), which was attributed to the incorporation of “active oxygen” in the film.[108]

2.3.3 The Influence of Heat Treatment in CAM Coating Syntheses

Post-treatment in the form of calcination (annealing) is a common step in CAM coating synthesis. In most approaches, the annealing is carried out in air and/or pure oxygen, mostly at moderate temperatures (e.g., 400 °C). First of all, for some techniques this step is used to remove solvents and other organic materials from CAM treatment (e.g., the sol-gel method). Apart from that, the annealing step also affects the morphology and crystallinity of a surface layer, and it is often used to obtain smoother, denser or more complete coatings with a better contact to the CAM.[109]

Depending on the temperature and the coating, both lithium diffusion into the coating and metal diffusion (doping) of the CAM (subsurface) are possible. The former has been reported to improve the performance of CAMs coated with a binary oxide layer.[30,109,110] This was shown to result from Li^+ incorporation into the coating and the resulting improvement of Li-ion conduction through the protection layer. Doping is discussed in numerous studies, since CAM coating/doping has been investigated extensively already for the application in LE-based LIBs, e.g., for zirconium oxide-based coatings.[95,111–114] Generally, it can be stated that a surface coating is increasingly transformed into a (subsurface) doping with increasing temperature (beyond a certain threshold temperature). However, such (surface) doping approaches are not yet systematically studied regarding their effects and relative importance in SSBs. Nevertheless, it is unlikely that proven CAM dopings for LIBs can just be transferred to SSBs. Interestingly, a large share of the so far reported and most beneficial coatings are based on highly charged cations such Nb^{5+}, Zr^{4+}, Ta^{5+} that have a low tendency for diffusion, suggesting that doping is not the most important factor of their functionality. It should be noted that their oxides also exhibit high oxidative stability. Furthermore, especially for highly charged cations, the threshold for significant diffusion is not surpassed at the mild post-treatment temperatures reported in the literature. Again, this indicates that coating performance is not considered to rely strongly on high levels of CAM doping.

Using an annealing step was found to be one of the most important factors for the performance of ALD-derived HfO_2@NCM85 in Publication I.[109] Therefore, Publication III places special emphasis on the multifaceted evolution of a coated CAM (ZrO_2@NCM85) during heat treatment.[115] Apart from coating crystallinity and doping, also the reaction of the zirconia with the NCM and the connected interlayer formation, as well as their influence on cycling behavior are discussed. The results indicate that potentially beneficial effects of high-temperature annealing can be outweighed by adverse phenomena that have not been discussed extensively in the literature so far. Lastly, it should be mentioned that heat treatments can have advantageous influences on the CAM (surface), independent of the presence of an added surface layer.[116] This should be considered when evaluating the effectiveness of coatings. In other words, coated CAMs need to be compared to the respective heat-treated, uncoated reference samples.

2.4 Review of CAM Coatings for Thiophosphate-Based SSBs

A review of the literature on CAM coatings for thiophosphate was written by Culver *et al*. in 2019.[30] The survey, spanning about 15 years of SSB research, showed that the SEs were mostly Li_2S-P_2S_5 compounds in these studies, while LGPS and argyrodite-type SEs had been employed sporadically as well. Regarding CAMs, most studies had focused on LCO, in some cases NCMs (typically with low Ni content) were used, with only few exceptions such as $LiNi_{0.5}Mn_{1.5}O_4$. The authors found that mostly (ternary) oxides such as $LiNbO_3$, $Li_4Ti_5O_{12}$ and Li_2SiO_3 had been applied to CAMs using wet chemical approaches such as spray coating or the sol-gel technique. Using oxides is beneficial because of their relatively good stability at high potentials. Li-containing ternary oxides usually exhibit appreciable Li-ion conductivity combined with low electronic conductivity. However, according to thermodynamic analyses and empirical results, ternary oxides are not stable in contact with delithiated CAMs at high voltages.[82,117] It is also advantageous that oxide coating layers can be synthesized relatively easily by calcination in air or oxygen. Owing to these promising properties, they have been the most studied group of compounds for SSB CAM coatings. Especially $LiNbO_3$ has been widely used and can be regarded as a prototype material in the field. Despite the marked improvements (increase in capacity, rate capability and cycling stability) over uncoated CAMs, evident in a large number of studies, mainly enabled by the reduction of (electro)chemical degradation, performance was still not sufficient, and a lack of thorough mechanistic understanding of coating functionality was noted.[30]

2.4.1 Recent Trends

Table 1 gives an overview over the recent reports (2019-2022) on CAM coatings for thiophosphate SSB cells. Note that a quantitative comparison of cell performance indicators is beyond the scope of this survey, but has been carried out in depth elsewhere.[118] It should be kept in mind that there is no standardized test setup nor a unified set of materials or parameters to compare performance data (and therefore CAM coatings) across research labs yet.

While **Table 1** only lists thiophosphate-based SSBs, it appears that most of the work on CAMs coatings deals indeed with this class of batteries. This seems reasonable since thiophosphate are widely regarded as the most promising class of SEs but suffer most from interfacial incompatibility issues. Generally, a trend towards material combinations that enable high power/energy density is observable. As for the SE, compounds with higher bulk ionic conductivity (such as LGPS, argyrodite LPSCl and lithium tin phosphorus sulfide) were used in most of the studies. Regarding CAMs, mainly Ni-rich NCMs (with a Ni content of more than 60% in the transition metal layer) were used instead of the model compound LCO, which was widely employed earlier. As noted previously, almost exclusively oxides were used as coating compounds, with the exception of the polymer poly-3,4-ethylene dioxythiophene (PEDOT)[119] and a dual-layer coating that included an outer shell of the sulfide SE LGPS[85] (however, again, an oxide was used as the CAM-facing layer).

A further observable tendency is that recently applied coatings were, on average, thinner, often with thicknesses below 10 nm. This is favorable because thinner surface layers impede interfacial ion transfer less. In other words, if a coating is very thin (on the order of a few nanometers), even mediocre ion conductors can be used. A lower bound for the thickness of coatings is mainly given by the deposition method. The lower thicknesses in recent works can in part be attributed to the more frequent application of ALD, while the usage of methods resulting in thicker layers such as pulsed laser deposition (PLD) was not continued. Dry coatings represent an exception to this trend (see below). The importance of post-annealing after applying a coating (or the corresponding precursors), as discussed in the previous section, was already noticed in past CAM modification approaches.[30] This trend has continued, meaning that a heat treatment is part of almost every recently reported CAM surface modification. Often, including in the publications of this thesis, it is even stated that it is crucial in determining the electrochemical performance.

2.4.1.1 Atomic Layer Deposition

Apart from the ALD-derived binary oxides presented in this thesis, ternary oxides such as $LiNbO_3$, Li_2O-ZrO_2 or Li_3PO_4 could be successfully deposited onto CAMs for the use in bulk-type SSBs.[85,120,121] This is notable since ALD of Li-containing compounds is not trivial.[122] For example, lithium zirconium oxide (LZO) compared favorably to its binary counterpart ZrO_x in LPSCl|LCO cathodes in a recent report.[121] This was attributed to facilitated charge transfer through the Li-containing oxide. However, the performance of the ZrO_x@LCO reference was rather limited, with much better results in terms of capacities, shown elsewhere. Even considering that LCO was used, the performance of the binary oxide-coated sample could probably be improved on. Moreover, the presence of Li in an oxide coating should mainly influence the ionic conductivity (here, $\sim 7 \cdot 10^{-5}$ S/cm could be achieved). This in turn should mainly impact the rate capability of the material which, unfortunately, cannot be evaluated since many investigations on the ZrO_x@LCO were omitted. However, the results rather suggest improved cycling stability of LZO@LCO, deviating from findings in the aforementioned studies on the lower high-voltage stability of ternary oxides, which is not explained convincingly. Overall, while it is often claimed that ternary oxides enable superior cycling performance and ALD produces high-quality CAM coatings, the success of the combination of the two has so far been limited with regards to the reported SSB cell performances.[85] To sum up, a systematic comparison between optimized binary and ternary oxides deposited using ALD for relevant CAM/SE combinations would certainly be of value. Based on this, it could be assessed whether the demanding Li-ALD chemistry should be used, or if indirect approaches aiming at the Li^+ incorporation into a binary oxide by post-annealing suffice to generate adequate Li-transfer capabilities of protective layers. The latter approach is followed and discussed in Publications I and III.

2.4.1.2 Wet Chemical Methods

In the past years, the use of wet chemical methods for CAM coatings has continued. For example, the dispersion method was used to coat the SE LGPS from solution onto

$LiNbO_3$@LCO to improve the interfacial contact with the catholyte, enabling high rate performance in such cathodes. The method was also modified to deposit oxide nanoparticles onto Ni-rich NCM materials (described in more detail below).[54,63] Regarding the sol-gel technique, several studies reported the coating of prior used compounds such as lithium niobate/zirconate on Ni-rich NCM CAMs, addressing their influence on gassing behavior in SSBs and the role of Li_2CO_3 in such coatings (see below).[49,50,123,124] Moreover, a few new compounds were deposited using this technique. For example, $Li_3B_{11}O_{18}$ was selected based on thermodynamic considerations.[82] The compound has a wide stability window and low reaction enthalpies with NCM523 and glassy LPS, which were used in the study. The $Li_3B_{11}O_{18}$ coating leads to superior performances over LZO, which reacts in a more exothermic manner with LPS (−111 vs 0 meV/atom of $Li_3B_{11}O_{18}$). The observed decomposition and breakdown of the LZO coating are attributed to the aforementioned lithium extraction at high voltages. Another previously unused coating composition (Li-Zn-Nb-O) was reported in Publication II.[125]

One of the most important recent works in the field published by researchers at Samsung demonstrated large-format cells (0.6 Ah) with high energy density (546 Wh/kg considering anode, separator and cathode) and high cycling stability (low capacity losses over 1000 cycles, >99.8% average Coulomb efficiency), among other impressive performance indicators.[126] This was enabled by a highly optimized cell design and several innovative concepts such as an Ag-C nanocomposite and warm isostatic pressing. Interestingly, a facile sol-gel-derived Li_2O-ZrO_2 was used as CAM coating. A uniform, 5 nm-thick layer on the NCM (90% Ni in transition metal layer) could be achieved. The coating was synthesized according to a previously reported recipe.[127] In brief, the CAM was suspended in a solution of lithium methoxide and zirconium(IV) tetrapropoxide in propanol, followed by vacuum drying at 50 °C while ultrasonicating the dispersion, filtration and calcination for 1 h in air. Presumably, further unspecified measures were taken to obtain such uniform films. Unfortunately, the coating is not characterized in detail to reveal potential differences from other LZO coatings. Nevertheless, this study shows that the combination of a known coating material and a facile coating method enables excellent cycling performance. This also exemplifies how the interpretation of performance data of compositionally similar or identical CAM coatings in the literature is limited by the coating quality, but certainly also by other non-optimized cell components.

Table 1: Survey of CAM coatings in thiophosphate-based SSB cells in the recent literature (published between 2019 and 2022). *Thickness estimated from micrographs. #From this thesis.

Compound(s) (Method)	**SE|CAM**	**Coating thickness/ weight fraction**	**Heat treatment (ϑ, atm., t)**	**Remarks**
Al_2O_3/ $LiAlO_2$[128] (Dry coating)	LPSCl| NCM701515	~50 nm*	600 °C, O_2, 8 h	High-energy mixing to apply fumed alumina to NCM without solvents; post-annealing transforms highly porous alumina coating into denser/smoother layer and improves performance
HfO_2[54] (Dispersion method)	LPSCl| NCM85	11 nm/ 0.82 wt%	400 °C, O_2, 2 h	Surfactant-stabilized HfO_2 nanoparticles (6 nm) conformally coated onto NCM secondary particles
HfO_2[109]# (ALD)	LPSCl| NCM85	2-3 nm/ 0.61 wt%	400 °C, O_2, 30 min	Thin, conformal polycrystalline layers; performance improvement by annealing of coated CAM
$Li_4Ti_5O_{12}$[129] (Dry coating)	NCM701515| LPSCl	0.5-2wt%	-	High-energy mixing to apply fumed $Li_4Ti_5O_{12}$ to NCM; no post-annealing; relatively coarse-grained surface layer
Li_2O-ZrO_2[121] (ALD)	LPSCl|LCO	~5 nm	-	ALD-derived “Li_2O-ZrO_2” compares favorably with ZrO_2; slightly non-uniform layer despite use of ALD
Li_2O-ZrO_2[126] (Sol-gel)	LPSCl| NCM900505	5 nm	300 °C, air, 1 h	Performance among the best reported in the SSB field; highly optimized pouch full-cell with Ag-C composite anode layer prepared with binder-containing, slurry-cast separator and cathode layer, warm isostatic pressing etc.
$Li_3B_{11}O_{18}$[82] (Sol-gel)	LPS| NCM532	≤10 nm	350 °C, O_2, 1 h	LBO is selected based on high oxidation stability and outperforms an LZO coating in this work
$LiNbO_3$/ Li_2CO_3[124] (Sol-gel)	LPSCl| NCM622, LPS| NCM622	~5-40 nm*/ 1 wt% $LiNbO_3$, 0.1-0.95 wt% Li_2CO_3	300 °C, air, 2 h	Variation of carbonate content to determine influence on cell performance
$LiNbO_3$[61] (Sol-gel)	LPSCl|$LiNiO_2$	0.76 wt%	350 °C, O_2, 2 h	First use of $LiNiO_2$ in SSBs; coating could substantially improve capacity retention in LPSCl-based cells
$LiNbO_3$/ LGPS[85] (ALD/ Dispersion method)	LGPS|LCO	5 nm ($LiNbO_3$), 30 wt% (LGPS)	-	ALD-derived $LiNbO_3$@LCO is additionally coated with LGPS using a wet-chemical method for better SE/CAM contact

LiNbO$_3$[130] **(Dry coating)**	Li$_7$P$_2$S$_8$I| NCM622	50-100 nm (3 wt%)	-	Nanoparticles synthesized via citrate route and applied in dry state to CAM using acoustic wave vibration (to deagglomerate NPs); coarse-grained coating is not densely covering CAM
LiNbO$_3$[131] **(ALD)**	LSPS| SC-NCM811	4 nm	300-500°C, O$_2$, 3 h	Annealing at 400 °C for optimal performance (removal of Li surface residues, decreased roughness); coating thickness fluctuates
Li$_3$PO$_4$[120] **(ALD)**	LGPS| NCM811	1/5/10 nm (outer coating)	600 °C, atm. N/A, 2 h	2-stage ALD process to first coat inner grain boundaries (yielding 10 nm layer) and then outer surface of NCM secondary particles; 5 nm-thick outer coating optimal
Li-Zn-Nb-O/ Li$_2$CO$_3$[125]# **(Sol-gel)**	LPSCl| NCM85	1 wt% (nom.) Li$_6$ZnNb$_4$O$_{14}$	100/300/ 500 °C, O$_2$, 2 h	Coating consists of nanocrystalline rocksalt Li$_3$NbO$_4$ embedded in Li$_2$CO$_3$, higher performance than conventional lithium niobate coatings
Li$_2$ZrO$_3$[130] **(Dry coating)**	Li$_7$P$_2$S$_8$I| NCM622	30-60 nm/ 3 wt%	-	Nanoparticles synthesized via citrate route and applied in dry state to CAM using acoustic wave vibration (to deagglomerate NPs). Coarse-grained coating layer not densely covering CAM
Li$_2$ZrO$_3$/ Li$_2$CO$_3$[50] **(Sol-gel)**	LPSCl| NCM622	≤10 nm/ ~1 wt% Li$_2$ZrO$_3$	300/800 °C, O$_2$/air, 5 h	Li$_2$CO$_3$ content depends on annealing atmosphere and temperature and influences performance
Li$_2$ZrO$_3$[82] **(Sol-gel)**	LPS| NCM532	≤10 nm	350 °C, air, 1 h	Delithiation of LZO at high voltages; coating “breakdown” observed
PEDOT[119] **(MLD)**	LGPS| NCM811	2/5/10 nm	-	Both CAM and carbon nanotube conductive additive coated with polymer PEDOT; 5 nm-thick layer optimal
ZrO$_2$/ Li$_2$CO$_3$[63] **(Dispersion method)**	LPSCl| NCM85	10 nm/ 0.92 wt% ZrO$_2$, 8 nm Li$_2$CO$_3$	400 °C, O$_2$, 2 h	Preformed zirconia NPs (4-5 nm) coating the NCM in regular monolayer with Li$_2$CO$_3$ interlayer
ZrO$_2$[115]# **(ALD)**	LPSCl| NCM85	1-5 nm/ 0.2-1.2 wt%	300-700 °C, O$_2$, 30 min	Different thicknesses and annealing temperatures tested; intermediate temperatures optimal for performance (capacity, rate capability, retention); temperatures ≥500 °C influence capacity negatively

2.4.2 The Role of Surface Impurities

In recent years, growing attention has been paid to lithium carbonate and other contaminants that are usually present for different reasons on the CAM surface (sometimes alongside protective coatings).[123] One reason for this was the growing awareness of the fact that Li_2CO_3 and related impurity species are formed to a non-negligible extent on Ni-rich layered oxide materials in ambient atmosphere.[132,133] This in turn, had been shown to negatively affect electrochemical performance and cause gas evolution in LIB and SSB cells.[57,58,132,133] Nevertheless, some experimental results indicated a protective role of artificially grown Li_2CO_3[134,135] and surface contaminants that were deliberately incorporated into hybrid coating layers.[84,123] Therefore, the effect of Li_2CO_3 was investigated in more detail. Kim *et al*. investigated the influence of the carbonate amount in a $Li_2CO_3/LiNbO_3$ hybrid coating on SSB performance.[124] While the carbonate fraction did not have a strong effect on the capacity and reversibility, the results suggested that a Li_2CO_3 content of 0.5-0.7 wt% could be optimal for rate capability. However, the authors noted that this could also result from other factors such as variations in surface microstructure and composition. They concluded that calcination in O_2 atmosphere might generally be preferable for increased reproducibility of the coating process. In another recent study, analysis of a $Li_2CO_3/LiNbO_3$ hybrid coating showed that the Li_2CO_3 and other carbonaceous species act as kind of a matrix for the metal oxide nanoparticles (see section below), meaning that they play an important role for the morphology of the surface layer.[49] Further conceivable advantages of the carbonaceous layers are that they enable full CAM coverage, despite the main coating constituent being particulate in nature. Moreover, they might stabilize the CAM/coating contact during cycling by adding some degree of flexibility.

While Li_2CO_3 should intrinsically not be a good coating compound (regarding stability and ionic conductivity),[117] it appears that its presence and that of related species (in suitable amounts) is beneficial to the SSB performance. However, there are still numerous open questions regarding its/their role. One reason for this knowledge gap is presumably that investigating the role of surface contaminants is challenging. The main difficulties are compositional complexity (Li_2CO_3 might be a main compound, but is probably not the only one) and difficult characterization. The latter requires non-destructive methods of high spatial resolution and chemical contrast. Moreover, for example, it is difficult to adjust the Li_2CO_3 content without influencing other CAM and/or coating properties. CAMs can be re-calcined at temperatures higher than 725 °C to reduce the fraction of Li_2CO_3.[109,115,125] However, it has been shown that Ni-rich layered oxides (which are especially prone to carbonate contamination) are not completely stable at such temperatures.[136] Alternatively, materials can be washed to remove surface impurities, but this has its own side effects such as rocksalt growth at the surface.[116] These considerations are true for bare CAMs, but obviously the influence of high-temperature annealing and washing on a coated CAM surface is even more complex to clarify. Moreover, some methods such as the sol-gel technique might intrinsically lead to the deposition of carbonaceous species, which are formed when residual precursor(s) and solvent molecules are not completely removed during calcination. This seems to be the case for the often-selected moderate temperatures. Ultimately, if the influence of ambient atmosphere is to be excluded, materials can only be synthesized, handled and analyzed in a dry-room or inert atmosphere.

While these considerations might explain why the topic of surface contaminants is omitted in a number of reports on coatings, following some basic guidelines would be a starting point. First of all, in all studies on CAM coatings, the carbonate content should be determined and stated alongside the weight fraction of the target compound. Secondly, if no specific measures for the reduction and prevention of carbon-containing contaminants are taken, it should be assumed that they are present in CAM coatings. While Li_2CO_3 is only mentioned in **Table 1** if explicitly stated in the respective publications, it should be contained in more coatings summarized in the survey.

2.4.3 Recently Proposed SSB CAM Coating Techniques

As mentioned above, wet chemical methods such as the sol-gel technique or dispersion approaches still account for a large share of recent coating studies. However, some coating methods have been adopted for SSBs for the first time.

2.4.3.1 Nanoparticle Coatings

Nanoparticle (NP) coatings (ZrO_2, HfO_2 etc.) can be considered a subtype of the wet chemical methods (**Figures 6a**-**c**).[54,63] While new in the SSB field, there are established methods to synthesize a wide range of compounds as NPs in different shapes and sizes.[137] The underlying idea is to gain better control over the coating morphology (homogeneity and thickness) by preforming the main constituents already in the dimensions of the final surface layer. In some cases, such NPs need to be stabilized in a dispersion using surfactants to avoid agglomeration in the liquid phase and on the CAM surface. For example, the amphiphilic compound oleic acid, an unsaturated fatty acid, has been used for this purpose. Indeed, thin (~10 nm) and highly conformal coatings could be obtained by the NP technique, comprising single or few layers of the metal oxide NPs and a carbonaceous layer (mainly consisting of Li_2CO_3). Such coatings yielded significant performance improvements (e.g., reversible specific capacities over 200 mAh/g_{CAM}, 94% capacity retention after 200 cycles) of tape-cast and pellet-type SSB cathodes, as well as in conventional LIBs. They enabled effective suppression of various degradation processes such as SE oxidation, gas evolution, interdiffusion and particle fracture.

Notably, in several cases, advanced characterization of coatings synthesized by other methods such as the sol-gel (**Figures 6d**-**f**) or ALD technique (**Figures 6g**-**i**) has shown that such coatings are actually constituted by nanoparticles as well. These form during the coating process on the CAM surface and are embedded in/on a carbonaceous matrix/layer, as explained above.[49,109,115,125]

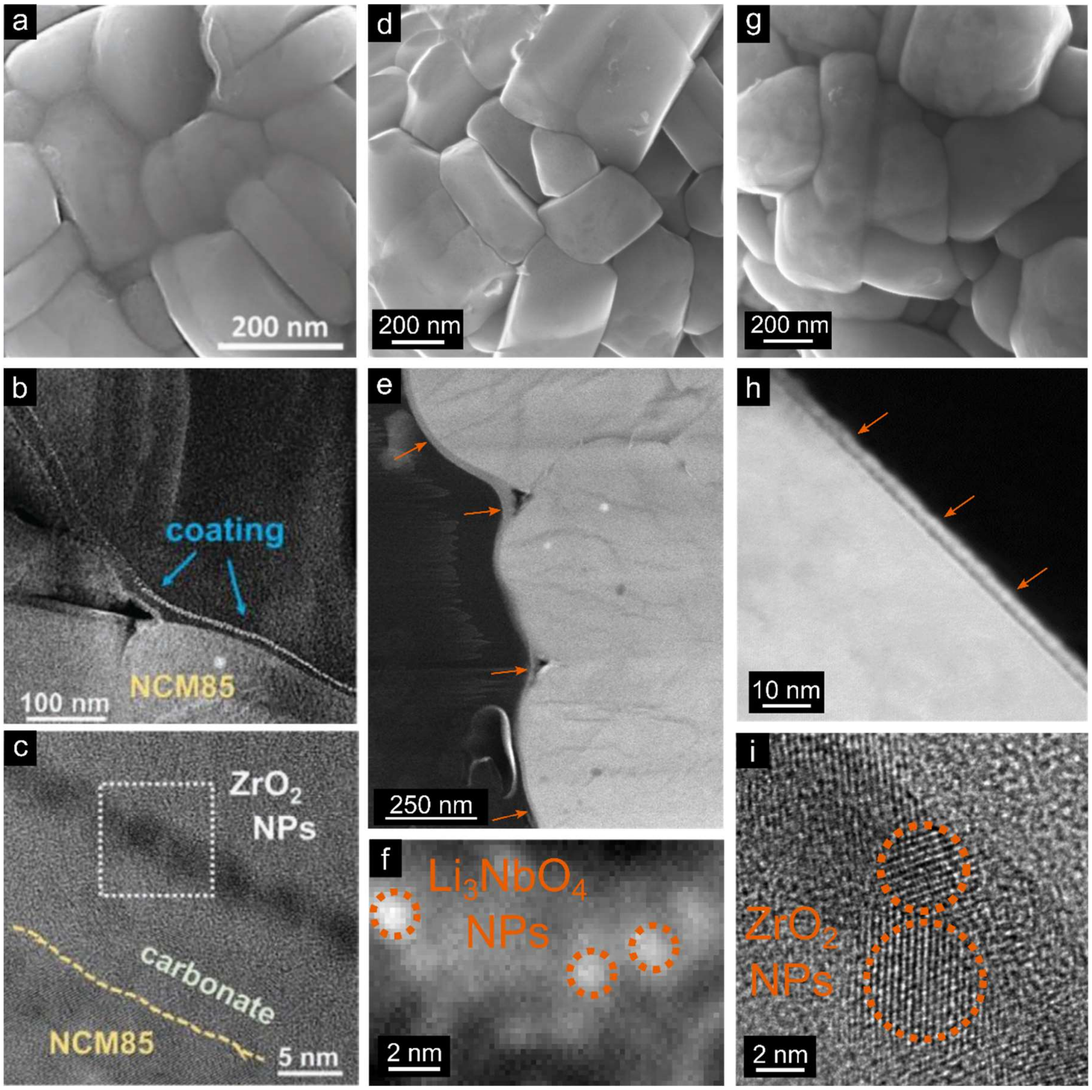

Figure 6: Electron micrographs at different magnifications of nanoparticle-containing coatings on polycrystalline NCM851005. a-c) ZrO_2 NPs on a carbonate layer coated using the dispersion method. Adapted from Ma *et al*.[63] d-f) Li_3NbO_4 NPs in a carbonate-containing matrix coated using the sol-gel method, targeting the nominal composition of $Li_6ZnNb_4O_{14}$. Adapted from Publication II.[125] g-i) ZrO_2 NPs constituting a surface layer synthesized using ALD. Adapted from Publication III.[115]

2.4.3.2 Dry Coatings

Dry coatings represent another emerging group of SSB CAM coatings (**Figure 7**).[128,130] Here, particulate coating compounds are deposited onto the CAM using mechanical forces. Advantageously, there is no need for solvents in these processes. Furthermore, seminal studies suggest that dry coatings can be applied in a time-efficient manner (on the order of minutes). After starting with a low-energy mixing step, the subsequently applied high-energy agitation of the CAM/coating powder mixtures often also entails a size reduction and de-agglomeration of the coating compound.[128,138] In a study on the coating of NCM622 with $LiNbO_3$ and Li_2ZrO_3 the so-called resonant acoustic mixing (RAM) method was used (**Figures 7a**-**c**).[130] This relatively new technique is based on the resonant vibration of the reaction mixture at around 60 Hz in a closed vessel, resulting in high material displacements and high accelerations acting on the powders (here 60 *g*).[139] The method has a number of benefits such as a good scalability (although it remains unclear whether the large amounts of CAM needed for EV applications could be processed), fast mixing times and cost efficiency. Additionally, it is applicable to a wide range of materials, not only solids. Therefore, the technique could represent an interesting platform to produce coatings in a facile manner. However, the micrographs of the as-received coatings show thick, coarse-grained and irregular surface layers. Hence, optimization of the process parameters seems necessary to assess whether high-quality coatings can be obtained using this technique. Specifically, a smaller size of the preformed NPs could be targeted and measures to prevent NP agglomeration should be considered.

A second dry coating approach was transferred from the LIB application to SSBs (**Figures 7d**-**f**).[128,129,138] Here, fumed nanostructured oxides such as alumina were deposited onto NCM701515 using high energy mixing. The process was carried out in a 0.5 L vessel with two rotors, but was stated to be well-scalable. The as-coated CAM was annealed at 600 °C to obtain $LiAlO_2/Al_2O_3$ with better ionic conductivity. Interestingly, this improved the SSB performance, while a similar heat treatment leads to porosity reduction and performance decrease of dry-coated Al_2O_3@NCM701515 in LIB cells.[138] This is explained by the fact that conventional LIB cells benefit from infiltration of coating pores by the liquid electrolyte, which leads to a higher contact area and therefore a lower interfacial current density, which is not possible for SEs. In an analogous approach using $Li_4Ti_5O_{12}$ (LTO) the annealing step was left out, which would reduce cost and complexity of such a process. However, electron microscopy images indicate that this leads to non-uniform surface layers, with the LTO accumulating at the NCM grain boundaries.[129] The first results on the proposed dry coating approach are encouraging in the sense that they show a significant performance improvement compared to the bare CAM. However, the improvements occurred from a relatively low level. This results probably from the CAM and SE used in the study. The approach could certainly be optimized for SSBs by reducing the coating thickness, the annealing parameters and using other compounds such as Li_2ZrO_3 and $LiNbO_3$ that have already been deposited using this procedure.[140] Conceivably, similar coating qualities and performances as those achieved, e.g., by wet chemical approaches could then be reached while benefitting from the aforementioned aspects.

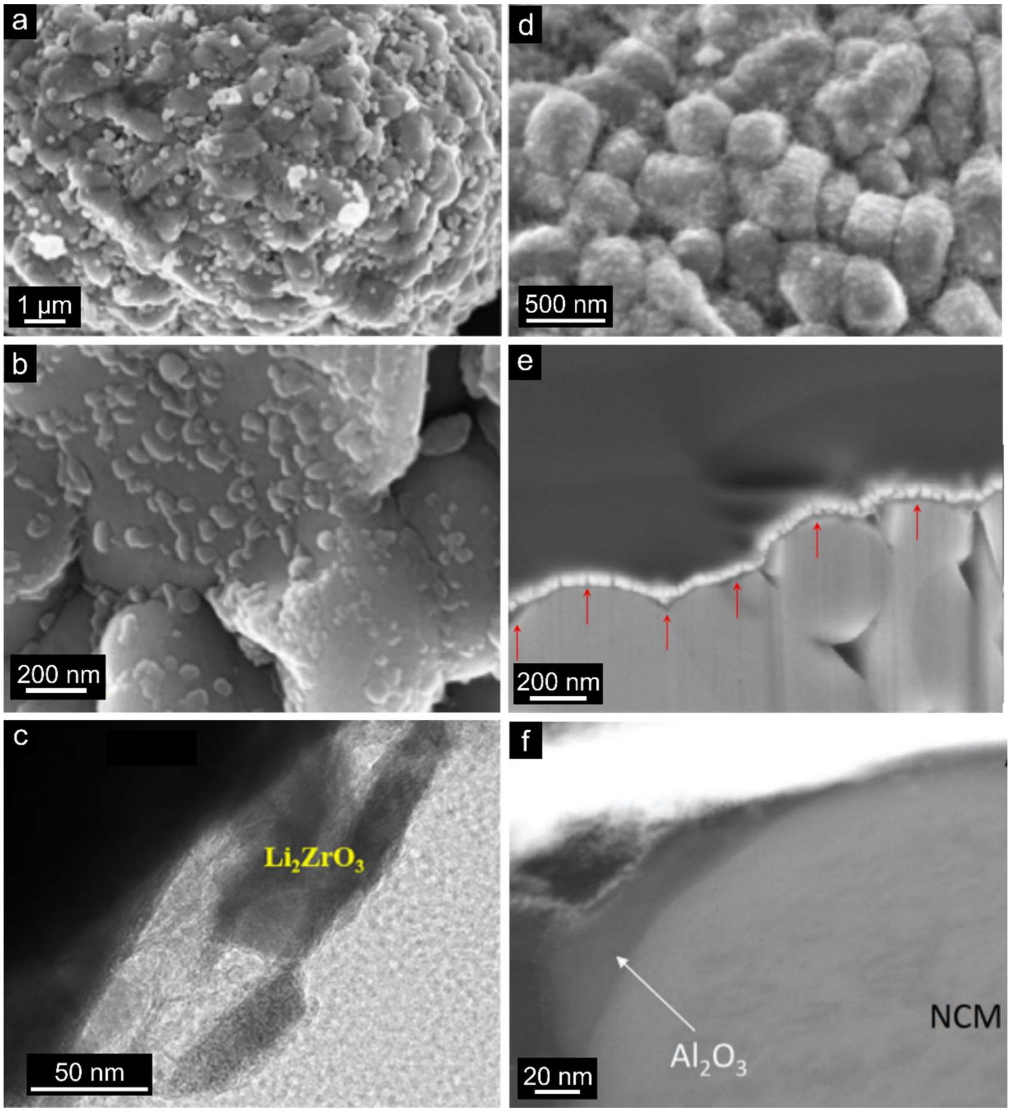

Figure 7: Electron micrographs of protective surface layers deposited by dry coating methods at different magnifications. a-c) Li_2ZrO_3 particles deposited onto NCM622 by resonant acoustic mixing. Adapted from Kim *et al*.[130] d-f) $LiAlO_2/Al_2O_3$ on NCM701515 obtained by high-energy mixing of the CAM and fumed nanostructured alumina and subsequent annealing at 600 °C. Adapted from Negi *et al*.[128]

3 Results

Before the start of this doctoral research project, the degradation processes at the SE|CAM interface in thiophosphate SSBs had been predicted and observed, and the necessity of CAM coatings had been recognized, along with properties that such a protective layer should have. Around the time of the beginning of this thesis, a survey of the already appreciably extensive body of CAM coating literature showed, among other things, that mainly LCO and Li_2S-P_2S_5 compounds were used as CAM and SE, respectively, in such studies. Furthermore, mainly wet chemical methods with limited control over coating thickness and uniformity were used, while there was only one study demonstrating ALD-coated CAMs in bulk-type SSB full cells. Finally, the authors noted a lack of systematic investigations into the property-functionality relations of coatings.

Based on this, the need for the capability to fabricate very thin and conformal CAM coatings in a controlled manner was apparent. Therefore, a central aim of this doctoral project was to systematically investigate the capability of atomic layer deposition to introduce ultrathin, conformal and tailor-made protective interlayers for relevant SSB cathodes with Ni-rich NCM and argyrodite LPSCl. The results of this were reported in Publications I and III. A further goal was to continue on efforts to improve the performance of sol-gel-derived coatings already established at BELLA. A successful approach was demonstrated in Publication II.

3.1 Publication I: High Performance All-Solid-State Batteries with a Ni-Rich NCM Cathode Coated by Atomic Layer Deposition and Lithium Thiophosphate Solid Electrolyte

In the work leading to Publication I, the binary oxide HfO_2 was targeted, for which ALD-processes on flat substrates were already established. Based on preliminary experiments, depositions onto sufficiently large batches of NCM powder in a porous sample holder (without any agitation) were found to be feasible in the available setup. Also, subsequently, processes were carried out at 250 °C using ozone. Importantly, an annealing step at 400 °C in oxygen was found to have the most significant benefits for the cycling performance among all tested process parameter variations in the coating synthesis.

Investigation of the as-prepared samples using ICP-OES, SEM, TEM, EDS and XPS revealed that, indeed, high-quality films can be deposited using this technique. Furthermore, the heat treatment was shown to lead to a homogenization of the initially nanoparticulate surface layer and suggested a partial incorporation of Li into the HfO_2. Finally, galvanostatic cycling showed appreciable improvements regarding reversible capacity, rate capability and cycling stability by the hafnia coating that were extended upon annealing.

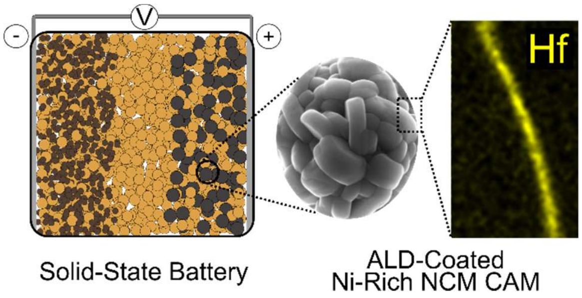

Figure 8: Table of Contents graphic of Publication I. Reprinted from reference [109].

The experiments were planned and designed by the first author under the supervision of M. Bianchini, J. Janek and T. Brezesinski. The first author optimized the ALD process, prepared the modified CAM samples, tested their electrochemical performance, conducted post mortem impedance measurements and sample recovery. Y. Tang performed the TEM investigation, including sample preparation and data analysis, and interpreted the corresponding results together with the first author. Y. Ma conducted the SEM examination, D. Goonetilleke analyzed the XRD data and J. Sann as well as F. Walther carried out the XPS investigation, including data analysis. The manuscript was written by the first author and edited by all coauthors.

Reprinted with permission from D. Kitsche, Y. Tang, Y. Ma, D. Goonetilleke, J. Sann, F. Walther, M. Bianchini, J. Janek, T. Brezesinski, *ACS Appl. Energy Mater.* **2021**, *4*, 7338.

ACS APPLIED ENERGY MATERIALS

www.acsaem.org Article

High Performance All-Solid-State Batteries with a Ni-Rich NCM Cathode Coated by Atomic Layer Deposition and Lithium Thiophosphate Solid Electrolyte

David Kitsche, Yushu Tang, Yuan Ma, Damian Goonetilleke, Joachim Sann, Felix Walther, Matteo Bianchini, Jürgen Janek,* and Torsten Brezesinski*

Cite This: *ACS Appl. Energy Mater.* 2021, 4, 7338−7345

Read Online

ACCESS | Metrics & More | Article Recommendations | Supporting Information

ABSTRACT: Achieving compatibility between cell components is one of the major challenges for the widespread adoption of bulk-type solid-state batteries. In particular, superionic lithium thiophosphate solid electrolytes suffer from oxidation at high voltages when interfaced with state-of-the-art cathode materials. Here, we report on atomic layer deposition (ALD) of conformal HfO_2 nanocoatings onto $LiNi_{0.85}Co_{0.10}Mn_{0.05}O_2$ (NCM-851005) cathode material. Based on electrochemical testing in high-loading (pellet-stack) solid-state battery cells, we demonstrate the positive effect of ALD HfO_2 coating on the cyclability and stability of NCM-851005. Modification of the coating morphology by postannealing further improved the cycling performance considerably, especially the Coulombic efficiency in the initial cycles and the rate capability. The results demonstrate the ability of ALD to produce high-quality surface films on industrially relevant electrode materials, thus providing a suitable platform for systematic investigations into the functionality of protective coatings in solid-state and other batteries.

KEYWORDS: *solid-state battery, atomic layer deposition, layered Ni-rich oxide cathode, argyrodite solid electrolyte, protective coating, interfaces*

1. INTRODUCTION

Solid-state batteries (SSBs) are among the prime candidates to replace conventional lithium-ion batteries (LIBs) for application in electric vehicles. This is due, in part, to the fact that LIBs are approaching their limits in terms of gravimetric and volumetric energy density in the near term.[1−3] Among the conceivable solid electrolytes (SEs), lithium thiophosphates stand out, as they exhibit the highest room-temperature ionic conductivities achieved so far while at the same time offering favorable mechanical properties.[1,4−6] However, their main drawback is a narrow stability window, giving rise to reduction (e.g., when paired with a lithium-metal anode) and oxidation reactions at low and high voltages, respectively. This is the case particularly at the voltages to which high-capacity cathode active materials (CAMs), such as layered lithium-metal oxides of the form $LiNi_xCo_yMn_zO_2$ (referred to as NCM or NMC), are being cycled. The side reactions occurring at the interface between the SE and CAM particles (and/or the conductive additive) during battery operation lead to the formation of detrimental degradation products and therefore to impedance growth and capacity fading.[5,7−9] This emphasizes the need for protective CAM coatings which, above all, should serve as an ion-conducting but electron-blocking layer. However, the surface shell must not be completely electronically insulating, as otherwise sufficient electronic percolation in the electrode cannot be achieved.[8]

In recent years, several studies have demonstrated the beneficial effects of CAM coatings in SSBs (e.g., evident from improvements in cycling stability and rate capability),[8] with the vast majority focusing on Li-containing ternary oxides, such as $LiNbO_3$ or $Li_4Ti_5O_{12}$, applied by wet-chemical deposition techniques.[10−12] Although the latter methods are versatile, cost-efficient, and easy to implement, they provide only limited control over coating thickness and morphology.[13] Hence, the quest for highly effective coating materials and advanced coating technologies is ongoing.

Atomic layer deposition (ALD) allows preparing atomically thin, conformal coatings on substrates with complex surfaces. The technique has been extensively applied in the field of LIBs.[13−18] Several promising CAM coatings based on $LiMO_x$ (e.g., with M = Nb,[19] Ta,[20] and P[21]) have been successfully produced by means of ALD. However, few examples exist in the literature on the use of ALD-modified CAMs in bulk-type SSBs.[8,22] Herein, we report on the coating of a Ni-rich NCM CAM, $LiNi_{0.85}Co_{0.10}Mn_{0.05}O_2$ (NCM-851005), with HfO_2.

Received: May 25, 2021
Accepted: June 11, 2021
Published: June 24, 2021

https://doi.org/10.1021/acsaem.1c01487
ACS Appl. Energy Mater. 2021, 4, 7338−7345

HfO_2 exhibits chemical and structural similarities to ZrO_2 from which a number of protective CAM coatings for SSB applications have been derived.[23−26] ALD of HfO_2 is a well-established process. Note that HfO_2 thin films are widely used as high-*k* dielectrics in the semiconductor industry. One of the most common precursors is tetrakis(ethylmethylamido)-hafnium(IV) (TEMAH), which can be employed in combination with H_2O or O_3 as the oxidant.[27−31]

In this work, we describe the preparation of HfO_2-coated NCM-851005 CAM via ALD of TEMAH/O_3 and characterize the surface layer using different techniques. The positive effect of the coating, especially after annealing, on the electrochemical performance of NCM-851005 in thiophosphate-based SSB cells is also demonstrated.

2. EXPERIMENTAL SECTION

2.1. Atomic Layer Deposition. Prior to ALD coating, $LiNi_{0.85}Co_{0.10}Mn_{0.05}O_2$ (NCM-851005; BASF SE) CAM was heated in O_2 flow at 750 °C for 3 h to reduce the amount of residual surface carbonates. The heating and cooling rates were set to 5 °C/min. For the coating process, 2 g of NCM-851005 was encased in a gas-permeable powder holder and introduced into the ALD reactor (Picosun), followed by flushing with N_2 and stabilization at 250 °C for 1 h. A typical ALD process comprised 20 cycles, consisting of a pulse sequence for O_3 (ozone generator from IN USA Inc.), followed by the same sequence for $Hf[N(CH_2CH_3)(CH_3)]_4$ (TEMAH; 99.99%, Sigma-Aldrich, precursor container heated at 105 °C). It included 100 pulses of 0.1 s duration, each followed by 2 s reactor purging and 60 s purging after the last pulse. This sequence was carried out once for O_3 before commencing the 20 ALD cycles. The N_2 carrier-gas flow in the TEMAH and ozone lines was set to 200 sccm. Finally, the HfO_2-coated NCM-851005 CAM was heated in O_2 flow at 400 °C for 30 min, with heating and cooling rates set to 10 °C/min.

2.2. Elemental Analysis. For elemental analysis, ALD-coated NCM-851005 CAM was dissolved in acid using a graphite furnace. The Hf content was determined by inductively coupled plasma-optical emission spectroscopy (ICP-OES) using a Thermo Fisher Scientific iCAP 7600 DUO. The carbon content was probed using a CS analyzer. Mass fractions represent the mean of three independent measurements.

2.3. X-Ray Diffraction (XRD). XRD data were collected using a STOE Stadi-P diffractometer with a DECTRIS MYTHEN 1 K strip detector in Debye−Scherrer geometry. The instrument uses a Mo anode, which provides a wavelength of $\lambda = 0.70926$ Å. The instrumental contribution to the peak broadening was obtained by measuring a NIST 640f Si standard reference material (SRM) as a line broadening reference. Rietveld refinement was performed using GSAS-II.[32] For refinement of NCM structural models against the diffraction data, the scale factor, zero shift, and crystallite size broadening parameters were allowed to vary. A fixed background was fitted to the data using a Chebyshev polynomial function with 16 terms. In the structural model, the unit cell parameters, the oxygen *z*-coordinate, and the atomic displace parameters (isotropic, u_{iso}) for each site were refined. Atoms occupying the same site were constrained to have the same atomic parameters, and site occupancy factors (SOFs) were constrained such that each site remained fully occupied.

2.4. X-Ray Photoelectron Spectroscopy (XPS). XPS measurements were carried out with a PHI VersaProbe II instrument (ULVAC-PHI, Inc.) using monochromatic Al Kα radiation (λ = 1486.6 eV). The power of the X-ray source was set to 100 W. The powder samples were pressed into pellets and mounted on a sample holder with an insulating double-sided tape (inert sample transfer). The examined area had a size of 1.3 mm × 0.1 mm. For survey and detail spectra, pass energies of 93.9 and 23.5 eV, respectively, were used. For charge neutralization, the PHI dual-beam charge neutralization was employed, consisting of a 20 nA, 10 V Ar-ion beam in combination with a 20 μA, 3 V electron beam and effectively pinning the sample potential at −3 V versus ground potential. Data evaluation was carried out with CasaXPS (version 2.3.18, Casa Software Ltd.). The spectra were calibrated in relation to the signal of adventitious carbon at 284.8 eV. A Shirley background was used, and the spectra were fitted with a GL line shape.

2.5. Scanning Electron Microscopy (SEM). SEM and energy-dispersive X-ray spectroscopy (EDS) were carried out at an accelerating voltage of 20 kV using a LEO-1530 electron microscope (Carl Zeiss AG) with a field-emission source. Cross-sectional SEM images were taken from manually fractured pellets, harvested from SSB cells before/after cycling.

2.6. Transmission Electron Microscopy (TEM). NCM-851005 CAM samples were investigated using Tecnai F20 ST and Themis-Z microscopes (Thermo Fisher Scientific) at accelerating voltages of 200 and 300 kV, respectively. Elemental maps of particle cross-sections were acquired by EDS on the Themis-Z microscope at 300 kV with a Super-X EDS detector. Sample cross-sections were prepared using a focused Ga-ion beam (FIB) in an FEI Strata 400 at 30 kV. Carbon layers were deposited by electron/ion-beam-induced deposition to protect the coating during sample preparation and processing. The carbon tape where the NCM-851005 CAM particles were put on was also thinned to characterize the coating.

2.7. Electrode Composites. The cathode composite was prepared by mixing the NCM-851005 CAM, Li_6PS_5Cl (LPSCl; NEI Corp.) SE, and Super C65 carbon black additive (Timcal) 69:30:1 by weight using 10 zirconia balls in a planetary mill (Fritsch) at 140 rpm for 30 min under an Ar atmosphere. Using the same procedure, the anode composite was prepared from carbon-coated $Li_4Ti_5O_{12}$ (LTO; NEI Corp.), LPSCl, and Super C65 carbon black at a weight ratio of 30:60:10.

2.8. SSB Cell Assembly and Testing. The electrochemical performance of the uncoated and HfO_2-coated NCM-851005 CAMs was tested in SSB cells using a customized setup comprising a polyether ether ketone (PEEK) sleeve and two stainless steel dies. Pellet stacks of 10 mm diameter were produced by first cold-pressing an amount of 100 mg LPSCl SE at a uniaxial pressure of 62 MPa to prepare the separator layer. Subsequently, 65 mg anode composite and 12 mg cathode composite (~2.9 mAh/cm² for q_{th} = 274 mAh/g_{CAM}) were added on either side, and the stack was pressed at 437 MPa. The final cells were galvanostatically cycled at 45 °C in a voltage range between ~2.9 and 4.3 V versus Li^+/Li while maintaining a uniaxial pressure of 81 MPa. Cycling stability tests were carried out at 0.5C (1C = 190 mA/g_{CAM}) for 60 cycles. Rate performance tests were carried out at 0.1C, 0.2C, 0.5C, and 1C, with two charge/discharge cycles at each C-rate. Results are averaged from at least three independent measurements.

2.9. LIB Cell Assembly and Testing. Cathodes for testing in LIB coin cells consisted of the NCM-851005 CAM, Super C65 carbon black, and polyvinylidene fluoride (PVDF) binder in a 94:3:3 weight ratio. A slurry based on *N*-methyl-2-pyrrolidone (NMP) was cast onto Al foil, vacuum-dried overnight at 120 °C, and then calendared at 15 N/mm. Circular electrodes of 12 mm diameter with an areal loading of 10 mg_{CAM}/cm^2 were punched out from the as-prepared tapes and used to assemble 2032 coin cells. The cells used a glass fiber separator (GF/D; Whatman), 100 μL LP57 electrolyte (1 M $LiPF_6$ in 3:7 by weight ethylene carbonate and ethyl methyl carbonate; BASF SE), and a Li-metal anode (Albemarle Germany GmbH). They were galvanostatically cycled at 45 °C in the same voltage window (2.9−4.3 V vs Li^+/Li) at 0.1C, 0.2C, 0.5C, and 1C, with two charge/discharge cycles at each C-rate, followed by 0.2C (1C = 225 mA/g_{CAM}).

2.10. Electrochemical Impedance Spectroscopy (EIS). EIS was carried out at frequencies ranging from 7 MHz to 100 mHz with an amplitude of 10 mV using a VMP3 impedance analyzer (Bio-Logic Science Instruments Ltd.).

3. RESULTS AND DISCUSSION

3.1. Surface Modification via ALD Coating. The as-received NCM-851005 CAM was first heated in O_2 flow at 750

°C for 3 h to minimize the impact of detrimental surface carbonates remaining from the synthesis.[33] According to elemental analysis, this treatment led to a decrease in carbon content from 0.23 to 0.09 wt %, which translates to a decrease in carbonate content from 1.38 to 0.54 wt % assuming that all carbon is present in the form of Li_2CO_3.

Initial experiments showed that HfO_2 can be deposited onto NCM-851005 using H_2O or O_3 as a counter reactant. It should be noted that exposure of layered Ni-rich oxide CAMs to ambient atmosphere typically leads to some degree of degradation.[34] However, exposure to H_2O in the ALD process at a reactor temperature of 250 °C did not severely affect the electrochemical performance of the NCM-851005 in SSB cells. Regardless, H_2O is present in the ALD reactor, as it is formed as a side product when using O_3 as the counter reactant, but in much lower amounts.[30] Nevertheless, based on promising initial electrochemical testing results (Figure S1), O_3 was selected as an oxidant in this study.

ICP-OES results indicated that the amount of deposited material, and therefore the coating thickness, can be tailored by the number of ALD cycles (Figure S2), as expected. The growth rate was found to increase with increasing ALD cycles. This suggests slower or less preferred deposition onto the NCM-851005 CAM than onto an already formed HfO_2 film. Similar behavior has been observed for other ALD processes in the past and is presumably due to the different number of reactive surface sites as the deposition progresses.[35] The sample containing 0.61 wt % HfO_2 (0.52 wt % Hf from ICP-OES), resulting from 20 TEMAH/O_3 cycles (100 pulses of 0.1 s duration), was among the best-performing CAMs in the investigated thickness or coating content range (Figure S3) and studied in more detail in the present work.

From the total surface area A, the mass fraction w and density ρ of the deposited material, and the total mass m of the sample, the coating thickness t can be estimated according to: $t = \frac{w}{\rho \cdot A} \cdot m$. Using the Brunauer–Emmett–Teller (BET) surface area of the NCM-851005 CAM ($A_{\mathrm{BET}} = 0.71\ \mathrm{m^2/g}$) and the crystallographic density of monoclinic HfO_2 ($\rho = 10.1\ \mathrm{g/cm^3}$), this yields a coating thickness of 0.86 nm, which in turn corresponds to an average growth per cycle of 0.43 Å. However, because the actual density of the deposited HfO_2 and the total substrate area are probably somewhat lower, the average coating thickness and growth rate are expected to be higher, and thus, the estimates should be seen as lower bounds only.

XRD was used to examine potential effects of the ALD process on the crystal structure of NCM-851005 (Figure S4). All of the observed diffraction peaks before and after coating, as well as after annealing at 400 °C for 30 min in an oxygen atmosphere, could be accounted for using the expected hexagonal α-$NaFeO_2$-type structure with the space group $R\bar{3}m$ (Figure S4a). Rietveld refinement confirmed that the change in structural parameters upon coating/annealing is negligible (Figure S4b and Table S1).

Furthermore, XPS was used to study the influence of the coating process on the NCM-851005 CAM. Figure S5 shows XP spectra of the Ni 2p and O 1s core-level regions. Both ALD (when using H_2O or O_3 as the counter reactant) and the postannealing step did not lead to a notable modification/degradation of the CAM surface. Apart from increased quantities of carbonate or related species, the data only suggest the presence of a slightly oxygen-depleted layer.

Next, electron microscopy was used to probe the morphology of the coated CAM and the microstructure of the coating. Figure 1 presents SEM, high-angle annular dark-field scanning transmission electron microscopy (HAADF STEM), and high-resolution TEM (HRTEM) data for the as-prepared HfO_2-coated NCM-851005. SEM investigations did not reveal major changes in CAM morphology during either the ALD or annealing processes (Figure 1a and Figure S6). Yet, bright spots were visible on the NCM-851005 particles, and a slightly roughened surface texture indicated the presence of a shell. TEM was also used to reveal the microstructure of the HfO_2 coating. Figure 1b shows a thin layer, conformally covering the outer surface of an NCM-851005 particle. As expected, it appeared bright in HAADF STEM imaging due to the high atomic number of Hf. Interestingly, the coating consisted of nanocrystals with a size of ~3 nm (Figure 1c). These nanoparticles were identified to have a monoclinic baddeleyite-type structure with the space group $P2_1/c$, which is the common low-temperature phase of HfO_2 (Figure S7).[36] Although such a morphology differs from the well-known 2-dimensional layer-by-layer (Frank-van der Merwe) growth, nanoparticle formation by ALD has been previously reported.[37] The latter can result from the incomplete reaction of the ALD precursor(s) with the available surface sites and preferential chemisorption on the already deposited material (island or Volmer–Weber growth). Preferred deposition onto transition-metal sites has been shown in a recent study on the

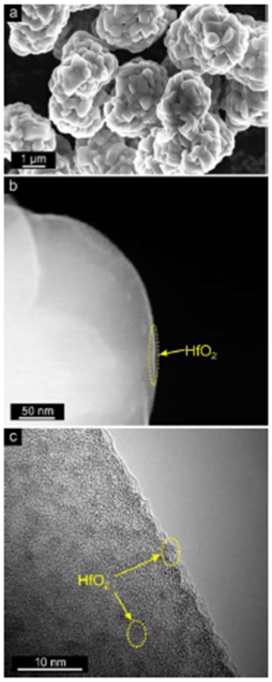

Figure 1. Electron microscopy of the as-prepared HfO_2-coated NCM-851005 CAM. (a) SEM image demonstrating preserved CAM morphology after coating. (b) HAADF STEM image showing the coating as a thin surface shell. (c) HRTEM image revealing the presence of monoclinic HfO_2 nanocrystals on the surface.

https://doi.org/10.1021/acsaem.1c01487
ACS Appl. Energy Mater. 2021, 4, 7338–7345

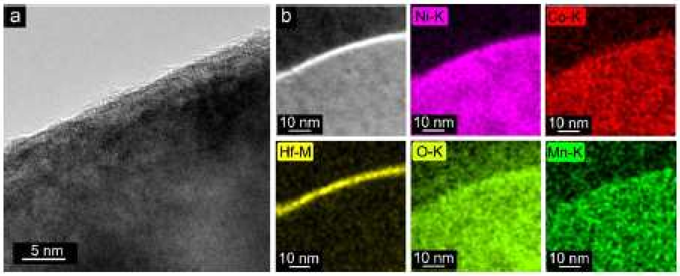

Figure 2. Electron microscopy of the annealed HfO_2-coated NCM-851005 CAM. (a) HRTEM image showing the particle surface. (b) HAADF STEM image and corresponding elemental maps of a FIB-cut cross-section.

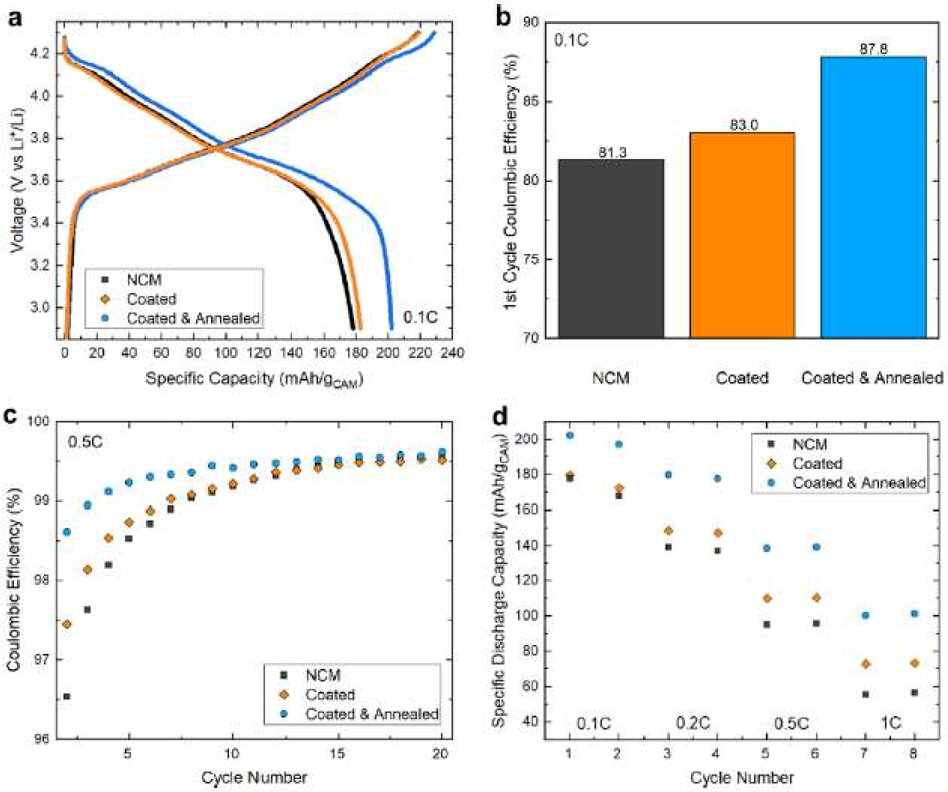

Figure 3. Electrochemical performance of the bare and (as-prepared and annealed) HfO_2-coated NCM-851005 CAMs in SSB cells at 45 °C. (a) First-cycle voltage profiles and (b) initial Coulombic efficiencies at 0.1C. (c) Coulombic efficiencies at 0.5C in the 2nd to 20th cycles. (d) Specific discharge capacities at rates ranging from 0.1C to 1C.

nonuniform growth of ALD alumina thin films on NCM111 (33% Ni content).[38]

Figure 2 shows the HfO_2-coated NCM-851005 CAM after annealing at 400 °C. Unlike for the as-prepared sample, no distinct coating nanoparticles were found on the surface, as can be seen from Figure 2a. Furthermore, the surface appeared smoother than before the heating. These results suggest that the HfO_2 layer densifies and spreads more evenly on the particle surface during the posttreatment process. The XP spectra of the Hf 4d and 4f core-level regions were similar before and after annealing (Figure S8). Although there is no direct proof of significant Li incorporation into the HfO_2 layer, slight peak shifts (by ~0.15 and 0.25 eV for the Hf 4d and 4f data, respectively, relative to the as-prepared HfO_2-coated NCM-851005) are indicative of increased Li/Hf interactions for the annealed CAM. In a recent study on Al_2O_3-coated NCM-701515, comparable (Al 2p) peak shifts to lower binding energies have been ascribed to the formation of an amorphous Al_2O_3/$LiAlO_2$ surface layer at 600 °C.[39] To gain more detailed information on the coating after annealing, FIB-cut cross-sections were examined by TEM. Figure 2b shows a HAADF STEM image and corresponding elemental maps confirming that Hf accumulates at the particle surface. The coating thickness was measured to be in the range between 2

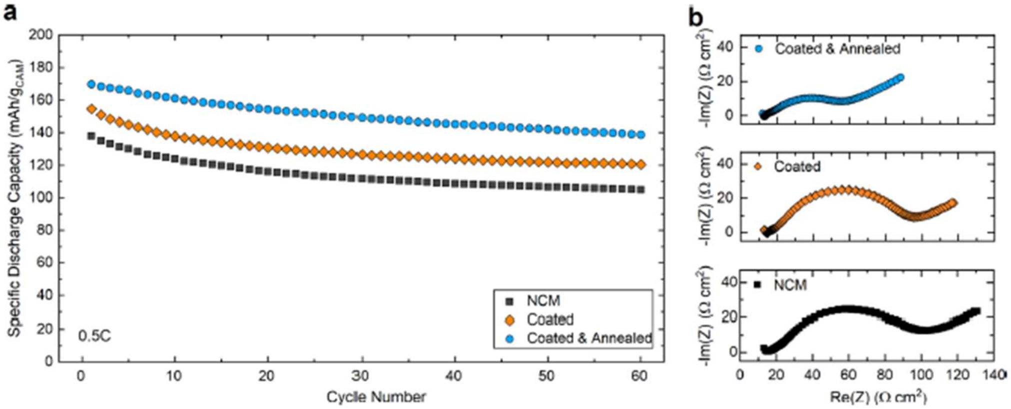

Figure 4. Long-term cycling performance of the bare and (as-prepared and annealed) HfO$_2$-coated NCM-851005 CAMs in SSB cells at 45 °C. (a) Specific discharge capacities at 0.5C over the first 60 cycles. (b) Nyquist plots of the electrochemical impedance at 45 °C for the different cells after cycling.

and 3 nm (Figure S9), corresponding to a growth rate of 1.0–1.5 Å per ALD cycle. Hence, the actual coating thickness is about three times larger than the above estimate. EDS also showed that virtually no Hf signal emerges from regions 5–10 nm away from the surface, thereby indicating that bulk diffusion can be ruled out (Figure S10). This was somewhat expected considering the ionic radius and charge of Hf^{4+}, as well as the relatively low annealing temperature. Elemental mapping further revealed that the primary particle surface in the interior of the secondary particles remains free of deposit (Figure S11). Coating of the interior could possibly be achieved to some extent, depending on the residual porosity, by altering the ALD conditions (e.g., using longer precursor pulse durations). However, regarding the application in SSBs, this is not important, as the inner primary particles are not in direct contact with the SE.

3.2. Electrochemical Testing and Postmortem Analysis.

The cycling performance of the uncoated (bare) and HfO$_2$-coated NCM-851005 CAMs was tested in a voltage range of ~2.9–4.3 V versus Li$^+$/Li at 45 °C in SSB cells with carbon-coated LTO as the anode active material and with argyrodite Li$_6$PS$_5$Cl SE, both in the electrode composites and as the separator layer (analogous data for the bare NCM-851005 CAM in liquid-electrolyte-based LIB coin cells are presented in Figure S12). Figure 3a shows the respective first-cycle charge/discharge curves at a rate of 0.1C. The shape of the voltage profiles was virtually identical, differing only slightly at the end of the discharge cycle. As is evident from Figure 3b, the larger specific discharge capacity delivered by the HfO$_2$-coated NCM-851005 CAMs is due to the lower irreversibility in the initial cycle and improved kinetics. Comparison of the voltage profiles further revealed a significantly lower overpotential for the cells using the annealed HfO$_2$-coated NCM-851005. As a result, both a slightly larger specific charge capacity (improved delithiation at voltages above 4.0 V vs Li$^+$/Li) and a more than 10% increase in specific discharge capacity to over 200 mAh/g$_{CAM}$ (~2.1 mAh/cm^2) were achieved. Note that (uncoated) as-prepared O$_3$-treated and annealed O$_3$-treated reference samples also delivered larger specific discharge capacities, with increased Coulombic efficiency and rate capability, than the pristine CAM (Figure S13). In case of the as-prepared HfO$_2$-coated NCM851005, the exposure to ozone during ALD might therefore partly explain the improved cyclability. However, among the annealed CAMs, the HfO$_2$-coated NCM851005 clearly outperformed the uncoated counterpart.

An important aspect of the superior electrochemical performance of the annealed HfO$_2$-coated NCM-851005 CAM is the considerably increased first-cycle Coulombic efficiency (~88% compared to ~83 and 81% for the as-prepared HfO$_2$-coated and uncoated NCM-851005, respectively). The differences in Coulombic efficiency point to a different extent of side reactions, especially in the initial cycles. In other words, the higher the reversibility, the lower the level of SE oxidation. Figure 3c shows the Coulombic efficiency over the first 20 cycles of identical cells cycled at a rate of 0.5C. The annealed HfO$_2$-coated NCM-851005 CAM showed the highest Coulombic efficiencies, also after the first cycle, stabilizing at ~99.5% from the 10th cycle onward, compared to more than 15 cycles for cells using the uncoated or as-prepared HfO$_2$-coated NCM-851005. Overall, these findings are characteristic of a more rapid formation of "stable" interfaces when using the annealed HfO$_2$-coated NCM-851005 CAM, which also helps explain the reduced overpotential during battery operation.

Figure 3d shows the specific discharge capacities for the different NCM-851005 CAMs at rates ranging from 0.1C to 1C (analogous data for the O$_3$-treated reference samples are presented in Figure S14). As can be seen, the rate performance was clearly improved by the surface coating. At low C-rates, the annealed HfO$_2$-coated NCM-851005 delivered significantly larger specific discharge capacities (by 20–30 mAh/g$_{CAM}$) compared to the uncoated and as-prepared HfO$_2$-coated NCM-851005 CAMs. Cells using the latter materials delivered similar capacities. However, they diverged with increasing C-rate. At 1C, the improvement in specific discharge capacity achieved by applying a coating amounted to 30% for the as-prepared HfO$_2$-coated NCM-851005 and 80% for the annealed HfO$_2$-coated NCM-851005. This is probably due, in part, to mitigated effects of interfacial side reactions, which predominantly occur in the initial cycles. Note that interfacial SE degradation has been shown to cause impedance increase.[5,8,9,40−42] Apart from this, the significantly larger cell capacities achieved with the annealed HfO$_2$-coated NCM-

851005, especially at higher C-rates, indicate improved charge transport across the CAM/SE interface. One possible explanation for this might be the reaction of residual Li species on the surface of the NCM-851005 particles with HfO_2 to form ternary oxides of Li, Hf, and O, which is supported by the XPS results discussed above. Such $Li_xHf_yO_z$ compounds may contribute to increased ionic conductivity (relative to the binary oxide coating), as has been shown, for example, for Al_2O_3.[39] However, the transformation of the crystalline coating into an amorphous surface layer, as evidenced by TEM, might also play a role. For $LiNbO_3$, a well-established CAM coating material, it has been shown that the ionic conductivity is higher, by several orders of magnitude, in the amorphous versus the crystalline state.[43,44]

Finally, the cycling stability of the uncoated and HfO_2-coated NCM-851005 CAMs was tested at a rate of 0.5C over 60 cycles (Figure 4a). As expected from the data shown in Figure 3, the first-cycle specific discharge capacity differed significantly among the different SSB cells ($q_{\mathrm{dis}} \approx 134$ mAh/g_{CAM} [uncoated NCM-851005], 155 mAh/g_{CAM} [as-prepared HfO_2-coated NCM-851005], and 170 mAh/g_{CAM} [annealed HfO_2-coated NCM-851005]). While the annealed HfO_2-coated NCM-851005 showed a rather linear capacity fading behavior (~0.3% per cycle), more rapid decay in the initial 10 cycles followed by linear capacity degradation was observed for both the as-prepared HfO_2-coated NCM-851005 and the uncoated NCM-851005. This confirms the longer time needed to form robust interfaces in the positive electrode when using the latter CAMs. The capacity retention after 60 cycles increased from ~76 to 78% by ALD coating of HfO_2 and further to ~82% (~139 mAh/g_{CAM} or ~1.5 mAh/cm^2) by postannealing at 400 °C, despite the fact that the total cumulative charge passing through the cell was much larger. Overall, stabilization of the CAM/SE interface by applying a coating on the surface of the NCM-851005 secondary particles via ALD is clearly beneficial to the cycling performance and stability of the bulk-type SSB cells.

Cross-sectional SEM imaging and EDS mapping of the cathode of cells using the annealed HfO_2-coated NCM-851005 before and after cycling revealed that the structure and morphology remain largely unaffected, without apparent loss of contact between the CAM and SE particles (Figures S15–S17). Furthermore, EIS measurements were conducted on the SSB cells after 60 cycles. Figure 4b shows representative Nyquist plots of electrochemical impedance, which can be used for semiquantitative comparisons. As is evident from the depressed semicircle, the difference in cathode interfacial impedance between the uncoated and as-prepared HfO_2-coated NCM-851005 CAMs was minor. However, a significantly smaller semicircle was found for the annealed HfO_2-coated NCM-851005, corroborating the results from the above cycling experiments.

4. CONCLUSIONS

High-quality, ALD-derived HfO_2 coatings onto NCM-851005 CAM, achieved by sequential surface reactions of H_2O, or preferably O_3, and TEMAH at 250 °C, have been presented. TEM measurements indicated that the as-deposited HfO_2 is nanocrystalline but can be modified by a facile posttreatment in an O_2 atmosphere at 400 °C, resulting in a smooth (amorphous) Hf-containing surface layer of thickness 2–3 nm. Electrochemical testing demonstrated the positive effect that HfO_2 ALD coating has on the cycling performance and stability of the NCM-851005 CAM in SSB cells. The cyclability was considerably improved by annealing of the coated material. We suggest the reaction of lithium residues on the NCM surface with HfO_2 to form Li-based ternary oxides as the most likely cause for such improvement, but this needs further study. The present work is one of the first demonstrations of the unique capabilities of ALD to produce ultrathin, conformal CAM coatings for bulk-type SSB applications. The results are encouraging and call for future investigations into other (Li-containing) materials to improve on the understanding of the functioning of protective coatings in solid-state and other batteries.

■ ASSOCIATED CONTENT

Supporting Information

The Supporting Information is available free of charge at https://pubs.acs.org/doi/10.1021/acsaem.1c01487.

> Cycling performance of the NCM-851005 coated by ALD of TEMAH/H_2O or TEMAH/O_3 (for 0, 10, 20, and 100 ALD cycles); HfO_2 content from ICP-OES versus ALD cycles; XRD patterns collected from the NCM-851005 before/after coating and the Rietveld refinement profile for the bare NCM-851005; refined structural parameters; O 1s and Ni 2p core-level spectra for the bare and HfO_2-coated NCM-851005 before/after heating; high- and low-magnification SEM images of the bare and HfO_2-coated NCM-851005 before/after heating; XP spectra of the Hf 4d and 4f core-level regions for the HfO_2-coated NCM-851005 before/after heating; calculation of lattice spacings from HRTEM images; determination of the coating thickness, EDS data, and mapping results for the annealed HfO_2-coated NCM-851005; cycling performance of bare NCM-851005 in liquid-electrolyte-based LIB coin cells; cycling performance of the O_3-treated (uncoated) NCM-851005 before/after heating in SSB cells; cross-sectional SEM imaging and EDS mapping of the cathode and cathode/separator interface of SSB cells using the annealed HfO_2-coated NCM-851005 before/after cycling (PDF)

■ AUTHOR INFORMATION

Corresponding Authors

Jürgen Janek – *Battery and Electrochemistry Laboratory, Institute of Nanotechnology, Karlsruhe Institute of Technology (KIT), 76344 Eggenstein-Leopoldshafen, Germany; Institute of Physical Chemistry & Center for Materials Science (ZfM/LaMa), Justus-Liebig-University Giessen, 35392 Giessen, Germany;* orcid.org/0000-0002-9221-4756; Phone: +49 721 60828827; Email: juergen.janek@kit.edu

Torsten Brezesinski – *Battery and Electrochemistry Laboratory, Institute of Nanotechnology, Karlsruhe Institute of Technology (KIT), 76344 Eggenstein-Leopoldshafen, Germany;* orcid.org/0000-0002-4336-263X; Phone: +49 721 60828827; Email: torsten.brezesinski@kit.edu

Authors

David Kitsche – *Battery and Electrochemistry Laboratory, Institute of Nanotechnology, Karlsruhe Institute of*

Technology (KIT), 76344 Eggenstein-Leopoldshafen, Germany

Yushu Tang – *Institute of Nanotechnology, Karlsruhe Institute of Technology (KIT), 76344 Eggenstein-Leopoldshafen, Germany*

Yuan Ma – *Battery and Electrochemistry Laboratory, Institute of Nanotechnology, Karlsruhe Institute of Technology (KIT), 76344 Eggenstein-Leopoldshafen, Germany;* orcid.org/0000-0003-4369-9520

Damian Goonetilleke – *Battery and Electrochemistry Laboratory, Institute of Nanotechnology, Karlsruhe Institute of Technology (KIT), 76344 Eggenstein-Leopoldshafen, Germany;* orcid.org/0000-0003-1033-4787

Joachim Sann – *Institute of Physical Chemistry & Center for Materials Science (ZfM/LaMa), Justus-Liebig-University Giessen, 35392 Giessen, Germany*

Felix Walther – *Institute of Physical Chemistry & Center for Materials Science (ZfM/LaMa), Justus-Liebig-University Giessen, 35392 Giessen, Germany*

Matteo Bianchini – *Battery and Electrochemistry Laboratory, Institute of Nanotechnology, Karlsruhe Institute of Technology (KIT), 76344 Eggenstein-Leopoldshafen, Germany; BASF SE, 67056 Ludwigshafen, Germany;* orcid.org/0000-0003-4034-7706

Complete contact information is available at: https://pubs.acs.org/10.1021/acsaem.1c01487

Notes

The authors declare no competing financial interest.

■ ACKNOWLEDGMENTS

This study was supported by BASF SE. The work was partly performed with the support of the Karlsruhe Nano Micro Facility (KNMF), a Helmholtz Research Infrastructure at Karlsruhe Institute of Technology (KIT). D.K. acknowledges financial support from the Fonds der Chemischen Industrie (FCI) through a Kekulé scholarship. We thank Dr. Thomas Bergfeldt (Institute for Applied Materials, KIT) for ICP-OES measurements, Dr. Andrey Mazilkin (Institute of Nanotechnology, KIT) for TEM support, Thomas Diemant (Ulm University) for XPS support, as well as Prof. Christian Kübel (Institute of Nanotechnology, KIT) and Dr. Xiaohan Wu (BASF SE) for fruitful discussions.

■ REFERENCES

(1) Janek, J.; Zeier, W. G. A Solid Future for Battery Development. *Nat. Energy* **2016**, *1*, 16141.

(2) Andre, D.; Kim, S.-J.; Lamp, P.; Lux, S. F.; Maglia, F.; Paschos, O.; Stiaszny, B. Future Generations of Cathode Materials: An Automotive Industry Perspective. *J. Mater. Chem. A* **2015**, *3*, 6709–6732.

(3) Randau, S.; Weber, D. A.; Kötz, O.; Koerver, R.; Braun, P.; Weber, A.; Ivers-Tiffée, E.; Adermann, T.; Kulisch, J.; Zeier, W. G.; Richter, F. H.; Janek, J. Benchmarking the Performance of All-Solid-State Lithium Batteries. *Nat. Energy* **2020**, *5*, 259–270.

(4) Wang, Y.; Richards, W. D.; Ong, S. P.; Miara, L. J.; Kim, J. C.; Mo, Y.; Ceder, G. Design Principles for Solid-State Lithium Superionic Conductors. *Nat. Mater.* **2015**, *14*, 1026–1031.

(5) Banerjee, A.; Wang, X.; Fang, C.; Wu, E. A.; Meng, Y. S. Interfaces and Interphases in All-Solid-State Batteries with Inorganic Solid Electrolytes. *Chem. Rev.* **2020**, *120*, 6878–6933.

(6) Sun, Y.-K. Promising All-Solid-State Batteries for Future Electric Vehicles. *ACS Energy Lett.* **2020**, *5*, 3221–3223.

(7) Lim, H.-D.; Park, J.-H.; Shin, H.-J.; Jeong, J.; Kim, J. T.; Nam, K.-W.; Jung, H.-G.; Chung, K. Y. A Review of Challenges and Issues Concerning Interfaces for All-Solid-State Batteries. *Energy Storage Mater.* **2020**, *25*, 224–250.

(8) Culver, S. P.; Koerver, R.; Zeier, W. G.; Janek, J. On the Functionality of Coatings for Cathode Active Materials in Thiophosphate-Based All-Solid-State Batteries. *Adv. Energy Mater.* **2019**, *9*, No. 1900626.

(9) Strauss, F.; Stepien, D.; Maibach, J.; Pfaffmann, L.; Indris, S.; Hartmann, P.; Brezesinski, T. Influence of Electronically Conductive Additives on the Cycling Performance of Argyrodite-Based All-Solid-State Batteries. *RSC Adv.* **2020**, *10*, 1114–1119.

(10) Kim, A.-Y.; Strauss, F.; Bartsch, T.; Teo, J. H.; Hatsukade, T.; Mazilkin, A.; Janek, J.; Hartmann, P.; Brezesinski, T. Stabilizing Effect of a Hybrid Surface Coating on a Ni-Rich NCM Cathode Material in All-Solid-State Batteries. *Chem. Mater.* **2019**, *31*, 9664–9672.

(11) Takada, K.; Ohta, N.; Zhang, L.; Fukuda, K.; Sakaguchi, I.; Ma, R.; Osada, M.; Sasaki, T. Interfacial Modification for High-Power Solid-State Lithium Batteries. *Solid State Ionics* **2008**, *179*, 1333–1337.

(12) Oh, G.; Hirayama, M.; Kwon, O.; Suzuki, K.; Kanno, R. Bulk-Type All Solid-State Batteries with 5 V Class $LiNi_{0.5}Mn_{1.5}O_4$ Cathode and $Li_{10}GeP_2S_{12}$ Solid Electrolyte. *Chem. Mater.* **2016**, *28*, 2634–2640.

(13) Weber, D.; Tripković, Đ.; Kretschmer, K.; Bianchini, M.; Brezesinski, T. Surface Modification Strategies for Improving the Cycling Performance of Ni-Rich Cathode Materials. *Eur. J. Inorg. Chem.* **2020**, *2020*, 3117–3130.

(14) Park, J. S.; Mane, A. U.; Elam, J. W.; Croy, J. R. Amorphous Metal Fluoride Passivation Coatings Prepared by Atomic Layer Deposition on $LiCoO_2$ for Li-Ion Batteries. *Chem. Mater.* **2015**, *27*, 1917–1920.

(15) Xie, J.; Sendek, A. D.; Cubuk, E. D.; Zhang, X.; Lu, Z.; Gong, Y.; Wu, T.; Shi, F.; Liu, W.; Reed, E. J.; Cui, Y. Atomic Layer Deposition of Stable $LiAlF_4$ Lithium Ion Conductive Interfacial Layer for Stable Cathode Cycling. *ACS Nano* **2017**, *11*, 7019–7027.

(16) Neudeck, S.; Mazilkin, A.; Reitz, C.; Hartmann, P.; Janek, J.; Brezesinski, T. Effect of Low-Temperature Al_2O_3 ALD Coating on Ni-Rich Layered Oxide Composite Cathode on the Long-Term Cycling Performance of Lithium-Ion Batteries. *Sci. Rep.* **2019**, *9*, 5328.

(17) Mohanty, D.; Dahlberg, K.; King, D. M.; David, L. A.; Sefat, A. S.; Wood, D. L.; Daniel, C.; Dhar, S.; Mahajan, V.; Lee, M.; Albano, F. Modification of Ni-Rich FCG NMC and NCA Cathodes by Atomic Layer Deposition: Preventing Surface Phase Transitions for High-Voltage Lithium-Ion Batteries. *Sci. Rep.* **2016**, *6*, 26532.

(18) Zhao, Y.; Zheng, K.; Sun, X. Addressing Interfacial Issues in Liquid-Based and Solid-State Batteries by Atomic and Molecular Layer Deposition. *Joule* **2018**, *2*, 2583–2604.

(19) Wang, B.; Zhao, Y.; Banis, M. N.; Sun, Q.; Adair, K. R.; Li, R.; Sham, T.-K.; Sun, X. Atomic Layer Deposition of Lithium Niobium Oxides as Potential Solid-State Electrolytes for Lithium-Ion Batteries. *ACS Appl. Mater. Interfaces* **2018**, *10*, 1654–1661.

(20) Liu, J.; Banis, M. N.; Li, X.; Lushington, A.; Cai, M.; Li, R.; Sham, T.-K.; Sun, X. Atomic Layer Deposition of Lithium Tantalate Solid-State Electrolytes. *J. Phys. Chem. C* **2013**, *117*, 20260–20267.

(21) Kozen, A. C.; Pearse, A. J.; Lin, C.-F.; Noked, M.; Rubloff, G. W. Atomic Layer Deposition of the Solid Electrolyte LiPON. *Chem. Mater.* **2015**, *27*, 5324–5331.

(22) Woo, J. H.; Trevey, J. E.; Cavanagh, A. S.; Choi, Y. S.; Kim, S. C.; George, S. M.; Oh, K. H.; Lee, S.-H. Nanoscale Interface Modification of $LiCoO_2$ by Al_2O_3 Atomic Layer Deposition for Solid-State Li Batteries. *J. Electrochem. Soc.* **2012**, *159*, A1120–A1124.

(23) Ito, S.; Fujiki, S.; Yamada, T.; Aihara, Y.; Park, Y.; Kim, T. Y.; Baek, S.-W.; Lee, J. M.; Doo, S.; Machida, N. A Rocking Chair Type All-Solid-State Lithium Ion Battery Adopting Li_2O-ZrO_2 Coated $LiNi_{0.8}Co_{0.15}Al_{0.05}O_2$ and a Sulfide Based Electrolyte. *J. Power Sources* **2014**, *248*, 943–950.

(24) Lee, Y.-G.; Fujiki, S.; Jung, C.; Suzuki, N.; Yashiro, N.; Omoda, R.; Ko, D.-S.; Shiratsuchi, T.; Sugimoto, T.; Ryu, S.; Ku, J. H.;

Watanabe, T.; Park, Y.; Aihara, Y.; Im, D.; Han, I. T. High-Energy Long-Cycling All-Solid-State Lithium Metal Batteries Enabled by Silver-Carbon Composite Anodes. *Nat. Energy* **2020**, *5*, 299−308.

(25) Wang, C.; Chen, L.; Zhang, H.; Yang, Y.; Wang, F.; Yin, F.; Yang, G. Li_2ZrO_3 Coated $LiNi_{1/3}Co_{1/3}Mn_{1/3}O_2$ for High Performance Cathode Material in Lithium Batteries. *Electrochim. Acta* **2014**, *119*, 236−242.

(26) Strauss, F.; Teo, J. H.; Maibach, J.; Kim, A.-Y.; Mazilkin, A.; Janek, J.; Brezesinski, T. Li_2ZrO_3-Coated NCM622 for Application in Inorganic Solid-State Batteries: Role of Surface Carbonates in the Cycling Performance. *ACS Appl. Mater. Interfaces* **2020**, *12*, 57146−57154.

(27) Kukli, K.; Ritala, M.; Sajavaara, T.; Keinonen, J.; Leskelä, M. Atomic Layer Deposition of Hafnium Dioxide Films from Hafnium Tetrakis(Ethylmethylamide) and Water. *Chem. Vap. Deposition* **2002**, *8*, 199−205.

(28) Senzaki, Y.; Park, S.; Chatham, H.; Bartholomew, L.; Nieveen, W. Atomic Layer Deposition of Hafnium Oxide and Hafnium Silicate Thin Films Using Liquid Precursors and Ozone. *J. Vac. Sci. Technol., A* **2004**, *22*, 1175−1181.

(29) Kirsch, P. D.; Quevedo-Lopez, M. A.; Li, H.-J.; Senzaki, Y.; Peterson, J. J.; Song, S. C.; Krishnan, S. A.; Moumen, N.; Barnett, J.; Bersuker, G.; Hung, P. Y.; Lee, B. H.; Lafford, T.; Wang, Q.; Gay, D.; Ekerdt, J. G. Nucleation and Growth Study of Atomic Layer Deposited HfO_2 Gate Dielectrics Resulting in Improved Scaling and Electron Mobility. *J. Appl. Phys.* **2006**, *99*, No. 023508.

(30) Liu, X.; Ramanathan, S.; Longdergan, A.; Srivastava, A.; Lee, E.; Seidel, T. E.; Barton, J. T.; Pang, D.; Gordon, R. ALD of Hafnium Oxide Thin Films from Tetrakis(Ethylmethylamino)Hafnium and Ozone. *J. Electrochem. Soc.* **2005**, *152*, G213−G219.

(31) Rose, M.; Niinistö, J.; Endler, I.; Bartha, J. W.; Kücher, P.; Ritala, M. In Situ Reaction Mechanism Studies on Ozone-Based Atomic Layer Deposition of Al_2O_3 and HfO_2. *ACS Appl. Mater. Interfaces* **2010**, *2*, 347−350.

(32) Toby, B. H.; Von Dreele, R. B. GSAS-II: The Genesis of a Modern Open-Source All Purpose Crystallography Software Package. *J. Appl. Crystallogr.* **2013**, *46*, 544−549.

(33) Kim, A.-Y.; Strauss, F.; Bartsch, T.; Teo, J. H.; Janek, J.; Brezesinski, T. Effect of Surface Carbonates on the Cyclability of $LiNbO_3$-Coated NCM622 in All-Solid-State Batteries with Lithium Thiophosphate Electrolytes. *Sci. Rep.* **2021**, *11*, 5367.

(34) Jung, R.; Morasch, R.; Karayaylali, P.; Phillips, K.; Maglia, F.; Stinner, C.; Shao-Horn, Y.; Gasteiger, H. A. Effect of Ambient Storage on the Degradation of Ni-Rich Positive Electrode Materials (NMC811) for Li-Ion Batteries. *J. Electrochem. Soc.* **2018**, *165*, A132−A141.

(35) Sønsteby, H. H.; Yanguas-Gil, A.; Elam, J. W. Consistency and Reproducibility in Atomic Layer Deposition. *J. Vac. Sci. Technol., A* **2020**, *38*, No. 020804.

(36) Geller, S.; Corenzwit, E. Hafnium Oxide, HfO_2 (Monoclinic). *Anal. Chem.* **1953**, *25*, 1774.

(37) Richey, N. E.; De Paula, C.; Bent, S. F. Understanding Chemical and Physical Mechanisms in Atomic Layer Deposition. *J. Chem. Phys.* **2020**, *152*, No. 040902.

(38) Hoskins, A. L.; McNeary, W. W.; Millican, S. L.; Gossett, T. A.; Lai, A.; Gao, Y.; Liang, X.; Musgrave, C. B.; Weimer, A. W. Nonuniform Growth of Sub-2 Nanometer Atomic Layer Deposited Alumina Films on Lithium Nickel Manganese Cobalt Oxide Cathode Battery Materials. *ACS Appl. Nano Mater.* **2019**, *2*, 6989−6997.

(39) Negi, R. S.; Celik, E.; Pan, R.; Stäglich, R.; Senker, J.; Elm, M. T. Insights into the Positive Effect of Post-Annealing on the Electrochemical Performance of Al_2O_3-Coated Ni-Rich NCM Cathodes for Lithium-Ion Batteries. *ACS Appl. Energy Mater.* **2021**, *4*, 3369−3380.

(40) Auvergniot, J.; Cassel, A.; Ledeuil, J.-B.; Viallet, V.; Seznec, V.; Dedryvère, R. Interface Stability of Argyrodite Li_6PS_5Cl toward $LiCoO_2$, $LiNi_{1/3}Co_{1/3}Mn_{1/3}O_2$, and $LiMn_2O_4$ in Bulk All-Solid-State Batteries. *Chem. Mater.* **2017**, *29*, 3883−3890.

(41) Walther, F.; Koerver, R.; Fuchs, T.; Ohno, S.; Sann, J.; Rohnke, M.; Zeier, W. G.; Janek, J. Visualization of the Interfacial Decomposition of Composite Cathodes in Argyrodite-Based All-Solid-State Batteries Using Time-of-Flight Secondary-Ion Mass Spectrometry. *Chem. Mater.* **2019**, *31*, 3745−3755.

(42) Walther, F.; Strauss, F.; Wu, X.; Mogwitz, B.; Hertle, J.; Sann, J.; Rohnke, M.; Brezesinski, T.; Janek, J. The Working Principle of a $Li_2CO_3/LiNbO_3$ Coating on NCM for Thiophosphate-Based All-Solid-State Batteries. *Chem. Mater.* **2021**, *33*, 2110−2125.

(43) Glass, A. M.; Nassau, K.; Negran, T. J. Ionic Conductivity of Quenched Alkali Niobate and Tantalate Glasses. *J. Appl. Phys.* **1978**, *49*, 4808−4811.

(44) Ohta, N.; Takada, K.; Sakaguchi, I.; Zhang, L.; Ma, R.; Fukuda, K.; Osada, M.; Sasaki, T. $LiNbO_3$-Coated $LiCoO_2$ as Cathode Material for All Solid-State Lithium Secondary Batteries. *Electrochem. Commun.* **2007**, *9*, 1486−1490.

3.2 Publication II: A Quasi-Multinary Composite Coating on a Nickel-Rich NCM Cathode Material for All-Solid-State Batteries

Publication II resulted from the continuation of prior work on sol-gel-derived oxide CAM coatings at BELLA. The initially targeted phase of the coating was $Li_6ZnNb_4O_{14}$ (LZNO), which had been shown to exhibit a promising ionic conductivity of $3\cdot10^{-5}$ S/cm (at room temperature). For this, an established sol-gel route in combination with subsequent calcination at varying temperatures was followed.

Interestingly, characterization using TEM showed that the coating consists of rocksalt-type Li_3NbO_4 nanoparticles embedded in Li_2CO_3. Due to the low Zn content in the surface layer, its role could not be completely clarified. However, testing of the as-coated NCM851005 in LPSCl-based SSB cells revealed excellent cycling performance, superior to conventional lithium niobate coatings that were synthesized analogously.

Rocksalt coating: Lithium thiophosphate-based solid-state battery cells using a layered Ni-rich NCM cathode active material show excellent cycling performance after coating of the secondary particles with a protective Li–Nb–O-type nanocomposite layer.

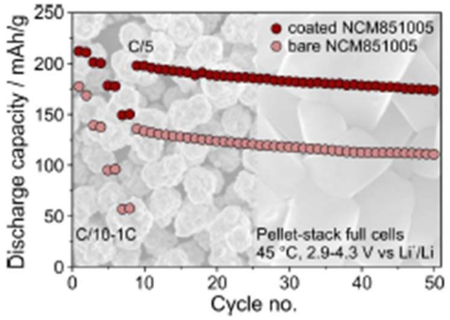

Figure 9: Table of Contents graphic and corresponding text of Publication II. Reprinted from reference [125].

A-Y. Kim had the original idea for this study and performed preliminary experiments. The experiments were designed by F. Strauss and the first author under the supervision of J. Janek and T. Brezesinski. N. Bartnick and F. Strauss synthesized the coated CAM samples and recorded the corresponding infrared spectra, which were analyzed by the first author. The first author performed the XRD characterization with help from D. Goonetilleke and evaluated the electrochemical performance of the modified CAM samples with contributions by N. Bartnick. Moreover, the first author conducted impedance measurements and prepared post mortem samples. Y. Tang performed the TEM experiments, including sample preparation and data analysis. Y. Tang and the first author interpreted the TEM results. C. Kübel contributed to discussions of the TEM results. Y. Ma conducted the SEM examination. The manuscript was written by the first author and edited by all coauthors.

Reprinted from D. Kitsche, F. Strauss, Y. Tang, N. Bartnick, A. Kim, Y. Ma, C. Kübel, J. Janek, T. Brezesinski, *Batter. Supercaps* **2022**, *5*, e202100397.

A Quasi-Multinary Composite Coating on a Nickel-Rich NCM Cathode Material for All-Solid-State Batteries

David Kitsche,[a] Florian Strauss,*[a] Yushu Tang,[b] Nikolai Bartnick,[a] A-Young Kim,[a] Yuan Ma,[a] Christian Kübel,[b, c, d, e] Jürgen Janek,[a, f] and Torsten Brezesinski*[a]

Inorganic solid-state batteries are attracting significant interest as a contender to conventional liquid electrolyte-based lithium-ion batteries but still suffer from several limitations. The search for advanced coatings for protecting cathode materials in solid-state batteries to achieve interfacial stability is a continuing challenge. In the present work, the surface of an industrially relevant Ni-rich $LiNi_xCo_yMn_zO_2$ cathode material, NCM-851005 (85% Ni), was modified by applying a coating containing Li, Nb and Zn, aiming at a composition $Li_6ZnNb_4O_{14}$, by means of sol-gel chemistry. Detailed characterization using scanning transmission electron microscopy combined with energy-dispersive X-ray spectroscopy and nano-beam electron diffraction showed that the surface layer after heating in O_2 at 500 °C contains Li_3NbO_4 nanocrystals and Li_2CO_3, with Zn presumably acting as a dopant. The protective coating on the NCM-851005 secondary particles significantly increased the cycling performance (reversible capacity, rate capability etc.) and stability of full cells using argyrodite Li_6PS_5Cl as solid electrolyte. Interestingly, the level of improvement is superior to that achieved with conventional $LiNbO_3$ coatings.

Introduction

Engineering of stable interfaces is one of the major challenges on the route to bulk-type solid-state batteries (SSBs) that are capable of competing with liquid electrolyte-based Li-ion batteries (LIBs) in terms of electrochemical performance.[1–3] Lithium thiophosphates, which exhibit the highest room-temperature ionic conductivities[4] among the reported superionic solid electrolytes (SEs) along with favorable mechanical properties, have been shown to be unstable when in contact with energy-dense cathode active materials (CAMs), such as $LiNi_xCo_yMn_zO_2$ (referred to as NCM), especially at the high voltages they are usually operated at.[5–11] Therefore, it is imperative to introduce a buffer layer between CAM and SE. In the past, various protective CAM coatings prepared by different techniques have been reported.[12–18] Wet-chemical methods have been applied most often because of their simplicity, low costs and good scalability.[12] Despite numerous reports on the beneficial effects of CAM coatings, such as reduced interfacial resistance and improved cycling stability, the quest for new materials or improving on established ones is ongoing. Specific chemical compositions and structures have been targeted to attain desired functionalities, typically based on the bulk properties of the respective materials. However, it has been shown that the microstructure and coating composition can deviate strongly from the bulk, especially if sol-gel methods are used in the preparation.

Ternary lithium niobium oxides, often assumed to be present as $LiNbO_3$, are among the best-performing coating materials and have been studied in considerable detail.[12–15] The relatively high room-temperature ionic conductivity in the amorphous state is regarded as one of the reasons for the suitability of $LiNbO_3$ in the SSB field.[19] Because of difficulties in characterizing nanoscale coatings on CAMs, their microstructure and chemical identity are often not examined in detail. However, in a recent study, the sol-gel derived Li–Nb–O-type coating has been shown to be particulate in nature, with $LiNbO_3$ nanoparticles surrounded by a Li_2CO_3-containing shell.[14]

In this work, we focus on a compound of composition $Li_6ZnNb_4O_{14}$, referred to as LZNO. This particular material has previously been investigated as a potential SE.[20,21] The metastable oxide was found to undergo disproportionation

---

[a] D. Kitsche, Dr. F. Strauss, N. Bartnick, Dr. A-Y. Kim, Dr. Y. Ma, Prof. J. Janek, Dr. T. Brezesinski
Battery and Electrochemistry Laboratory, Institute of Nanotechnology, Karlsruhe Institute of Technology (KIT), Hermann-von-Helmholtz-Platz 1, 76344 Eggenstein-Leopoldshafen, Germany
E-mail: florian.strauss@kit.edu
torsten.brezesinski@kit.edu
[b] Dr. Y. Tang, Prof. C. Kübel
Institute of Nanotechnology, Karlsruhe Institute of Technology (KIT), Hermann-von-Helmholtz-Platz 1, 76344 Eggenstein-Leopoldshafen, Germany
[c] Prof. C. Kübel
Karlsruhe Nano Micro Facility (KNMF), Karlsruhe Institute of Technology (KIT), Hermann-von-Helmholtz-Platz 1, 76344 Eggenstein-Leopoldshafen, Germany
[d] Prof. C. Kübel
Helmholtz Institute Ulm (HIU), Helmholtzstr. 11, 89081 Ulm, Germany
[e] Prof. C. Kübel
Technical University Darmstadt, Department of Materials and Earth Sciences, Alarich-Weiss-Str. 2, 64287 Darmstadt, Germany
[f] Prof. J. Janek
Institute of Physical Chemistry & Center for Materials Research (ZfM/LaMa), Justus-Liebig-University Giessen, Heinrich-Buff-Ring 17, 35392 Giessen, Germany

Supporting information for this article is available on the WWW under https://doi.org/10.1002/batt.202100397

into Li_3NbO_4, $Li_{1-x}NbO_3$ and $LiZnNbO_4$ upon cooling after high-temperature solid-state synthesis. Nonetheless, the conductivity of the as-obtained composite material was relatively high, approximately 3×10^{-5} S/cm at room temperature, making the Li–Zn–Nb–O system attractive for CAM coatings. Here, we surface-modified a Ni-rich NCM CAM, $LiNi_{0.85}Co_{0.10}Mn_{0.05}O_2$ (NCM-851005), aiming at the nominal coating composition of LZNO, for application in lithium thiophosphate-based SSB cells.

Results and Discussion

The NCM-851005 CAM was first heated in O_2 at 750°C to reduce the amount of surface impurities, followed by coating using a sol-gel route, similar to recent studies.[15,22,23] The treated material was then heated in O_2 at 100, 300 or 500°C. The respective samples are referred to as LZNONCM-100/300/500 hereafter. Using inductively coupled plasma-optical emission spectroscopy (ICP-OES), the Zn and Nb weight fractions were determined to be 0.077(1) and 0.50(1) wt.%, respectively, slightly below the targeted values of 0.093 and 0.53 wt.% (corresponding to 1 wt.% LZNO). Note that the molar ratio of n(Nb):n(Zn) ≈4.57 also deviated from the stoichiometric ratio of 4.

Figure 1(a–d) shows low- and high-magnification scanning electron microscopy (SEM) images of the bare NCM-851005 and LZNO-NCM-500 (LZNO-NCM-100/300 are shown for comparison in Figure S1, Supporting Information). The morphology of the base CAM was found to remain unaltered upon coating. However, small amounts of agglomerated coating material were observed to be randomly distributed over the secondary particles, as somewhat expected for a non-optimized sol-gel synthesis. These observations were made irrespective of the heating temperature.

The presence of Li_2CO_3 in the bare and coated NCM-851005 CAMs was verified via attenuated total reflection-infrared (ATR-IR) spectroscopy (Figure S2, Supporting Information), with minor differences between the spectra. This result indicates that some surface impurities from the synthesis remained, and the carbonate content did not change much with coating. According to elemental analysis, the Li_2CO_3 content was approximately 0.5 wt.% in all samples. Note that previous studies have demonstrated that carbonate species, as part of hybrid or solid-solution coatings, can be beneficial to the SSB performance.[15,24]

X-ray diffraction (XRD) was used to assess possible changes in lattice structure of the coated samples. All reflections in the patterns of the different CAMs can be indexed within the $R\text{-}3m$ space group (α-$NaFeO_2$-type structure), as expected for NCM materials (Figure 2). In addition, refinement analysis (see Figure S3, Supporting Information, for Rietveld profiles) revealed that the crystal structure remains largely unaffected (Table 1).

Based on electrochemical performance screening of the coated NCM-851005 CAMs (Figure S4, Supporting Information),

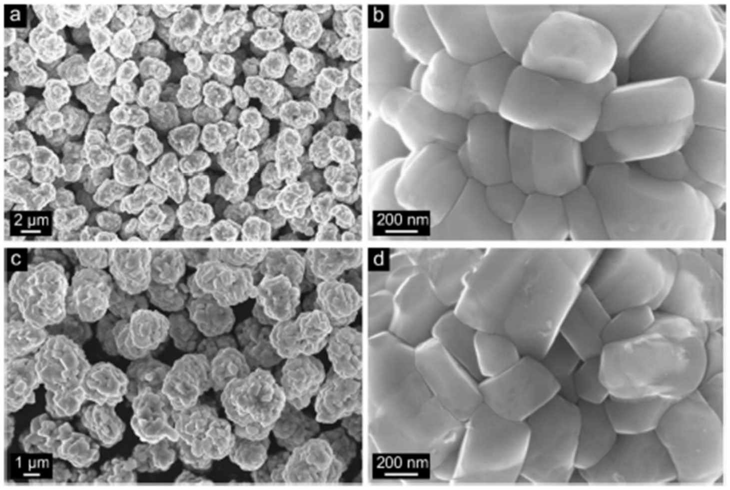

Figure 1. SEM images at different magnifications of a, b) bare NCM-851005 and c, d) LZNO-NCM-500.

Table 1. Refined structural parameters of bare and LZNO-coated NCM-851005 CAMs.

Sample	Rf [%]	a [Å]	c [Å]	V [Å^3]	z of O	u_{iso} Li site [Å^2]	u_{iso} TM site [Å^2]	Ni on Li site
NCM-851005	2.07	2.86993(7)	14.1872(3)	101.197(4)	0.2420(2)	0.018(2)	0.0052(2)	0.027(2)
LZNO-NCM-100	1.97	2.87017(7)	14.1866(3)	101.211(4)	0.2421(1)	0.021(2)	0.00500(2)	0.031(2)
LZNO-NCM-300	1.58	2.87028(6)	14.1858(3)	101.213(3)	0.2419(1)	0.025(2)	0.0032(2)	0.036(2)
LZNO-NCM-500	2.4	2.87048(7)	14.1869(3)	101.234(4)	0.2419(2)	0.021(2)	0.0054(2)	0.032(2)

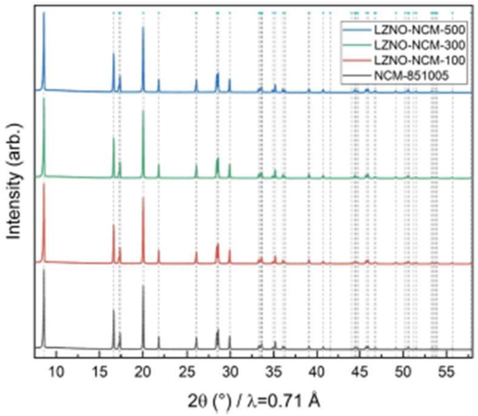

Figure 2. Normalized XRD patterns collected from bare and LZNO-coated NCM-851005 CAMs.

LZNO-NCM-500 was selected for more detailed investigations. Transmission electron microscopy (TEM) was used to gain insights into the microstructure of the coating. The presence of an amorphous shell on the secondary particles was evidenced by high-resolution TEM (Figure S5, Supporting Information). Figure 3(a) presents a low-magnification high-angle annular dark-field scanning TEM (HAADF STEM) image, showing the coating on the outer surface of a focused ion beam (FIB)-prepared NCM-851005 particle cross-section. The thickness of this layer ranged from a few nanometers to a few tens of nanometers, and the coating appeared to be somewhat thicker at the outward facing grain boundaries (see also Figure S6, Supporting Information). The presence of uncoated (free) surfaces is in principle conceivable but was not apparent from the imaging data.

The chemical composition of the coating was further probed using energy-dispersive X-ray spectroscopy (EDS). Figure 3(b) shows a higher magnification HAADF STEM image and corresponding elemental maps of the surface region of a FIB-prepared particle cross-section. A clear separation of CAM and coating was evident in STEM dark-field mode, coinciding with the locations of Ni and Nb. Diffusion of Nb into the bulk was not observed, in agreement with expectations considering the size and charge of the Nb ions. The elemental map of Zn suggests its presence both in the coating and in the NCM-851005 CAM. However, given the minor Zn content, the EDS results are not unambiguous. This issue was not to be solved by electron energy-loss spectroscopy (EELS) either because of overlap of the Ni L-edge (1008 eV) and Zn L-edge (1020 eV) and the very low amount of Zn relative to that of Ni. Hence, elucidating the specific role of Zn in the LZNO-NCM requires further study.

Crystalline species in the amorphous surface layer were detected by nano-beam electron diffraction (NBED; Figure S7, Supporting Information). Virtual dark-field images (see Figure S8, Supporting Information, for details on the 4D-STEM approach) revealed the presence of nanoparticles (Figure 3c, left side) having a cubic crystal structure (Figure 3c, right side), unlike the targeted monoclinic LZNO.[20] Previous studies have shown that the latter phase can only be obtained at high temperatures and is not stable upon cooling. However, a room-temperature ionic conductivity of $\sigma_{Li} \approx 3 \times 10^{-5}$ S/cm has been reported for the resulting composite material, which is in the range of that of good oxide Li-ion conductors.[21] The lattice spacings match well with those of rocksalt-type (*Fm*-3*m* space

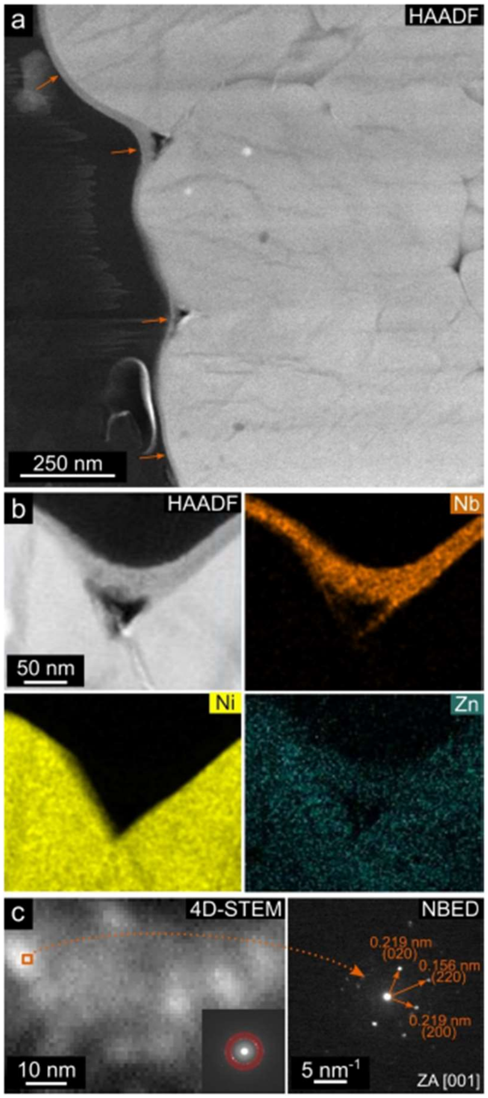

Figure 3. Electron microscopy of LZNO-NCM-500. a) Low-magnification HAADF STEM image of a FIB-prepared particle cross-section, with orange arrows indicating the coating. b) High-magnification HAADF STEM image and corresponding elemental maps. c) Left: Virtual dark-field image (aperture indicated in the inset diffraction pattern) of the coating from a 4D-STEM dataset. Right: Indexed NBED pattern of the area denoted on the left.

group) lithium niobium oxides, such as Li_3NbO_4 and related compounds.[25,26] Note that cubic Li_3NbO_4 has previously been prepared by a sol-gel method.[27] In addition, a broad reflection observed at low diffraction angles (see Figure S7, Supporting Information), not indexable in the *Fm*-3*m* space group, is probably resulting from partially crystalline Li_2CO_3, as observed by ATR-IR (Figure S2, Supporting Information). The protective surface layer thus shows similarities to previously reported $Li_2CO_3/LiNbO_3$ hybrid coatings on an NCM-622 (60% Ni) CAM, where the lithium niobate was embedded in an amorphous carbonate matrix.[14,15,28]

Until recently, the presence of crystalline Li_3NbO_4 in sol-gel derived Li–Nb–O-type coatings had not been demonstrated. This could be because the preparation conditions usually involve heating at temperatures below the onset of crystallization. Another reason could be the lack of advanced characterization techniques required to detect these species. Specifically, Nb coatings on NCM-811 (80% Ni) have been examined for their crystalline components.[29,30] In the first study, $LiNbO_3$ and Li_3NbO_4 have been predominantly observed at temperatures ranging from 400 to 500 °C and 700 to 800 °C, respectively (without comments on the lattice structures).[29] In the second study, the authors pointed out that Li_3NbO_4 is much more abundant than $LiNbO_3$ in the surface layer at 475 °C already but difficult to detect because of its low crystallinity.[30] Based on these results, we decided to probe a (bulk) mixture of the coating reagents in the absence of the NCM-851005 CAM *in situ* during heating in O_2 using XRD. The crystallization (onset) temperature was found to be approximately 470 °C (see contour plot in Figure S9, Supporting Information). The main component was $LiNbO_3$ (*R*3*c* space group). Li_3NbO_4 identified via NBED could not be observed clearly by XRD, thereby indicating a different crystallization and/or phase formation behavior relative to the nanoscale coating on the surface of the layered oxide CAM. Regardless, the degree of crystallinity is assumed to be relevant, as the positive effect of lithium niobate coatings has been attributed in part to their favorable electrical transport properties. Apart from that, the identification of cubic Li_3NbO_4, which has recently received attention as a host structure for disordered rocksalt (DRX) CAMs,[31,32] expands the current perspective on Li–Nb–O-type protective coatings. Although Li_3NbO_4 is an insulator, transition metal substitution can affect the cation ordering and result in a percolating network for lithium migration.[32] This could potentially be a new approach for the development of advanced coating materials for SSB and/or LIB applications.

The electrochemical performance of the bare and coated NCM-851005 CAMs was probed at 45 °C in the voltage range 1.35–2.75 V vs. $Li_4Ti_5O_{12}/Li_7Ti_5O_{12}$ (approximately 2.9–4.3 V vs. Li^+/Li) in pellet-stack SSBs with argyrodite Li_6PS_5Cl (LPSCl) SE, used in the electrodes and separator, and with $Li_4Ti_5O_{12}$ (LTO) as anode active material. LTO was chosen because of its zero-strain nature and favorable operating voltage range (note that the focus of the present work is on the NCM-851005 CAM). In fact, preliminary data confirm that the anode has no major effect on the cycling performance of the cathode. Figure 4(a) shows the first-cycle charge/discharge curves of representative cells at a rate of 0.1 C. The LZNO-NCM-500 delivered a specific discharge capacity of 212 mAh/g_{CAM} (approximately 2.2 mAh/cm^2), compared to 178 mAh/g_{CAM} for the bare NCM-851005, enabled by superior kinetics and reversibility. The voltage profile suggests improved delithiation, resulting in a larger capacity than for the uncoated counterpart. The difference in Coulombic efficiency, 88.6% vs 81.3% for the coated and uncoated CAM, respectively, indicates that more severe side reactions occurred in the case of bare NCM-851005.[14] This result helps to explain the strongly reduced overpotential observed for the LZNO-NCM-500. It should be noted that resistance buildup has been reported to result from detrimental chemical and electrochemical reactions between the electrode constituents during cycling operation, among others.

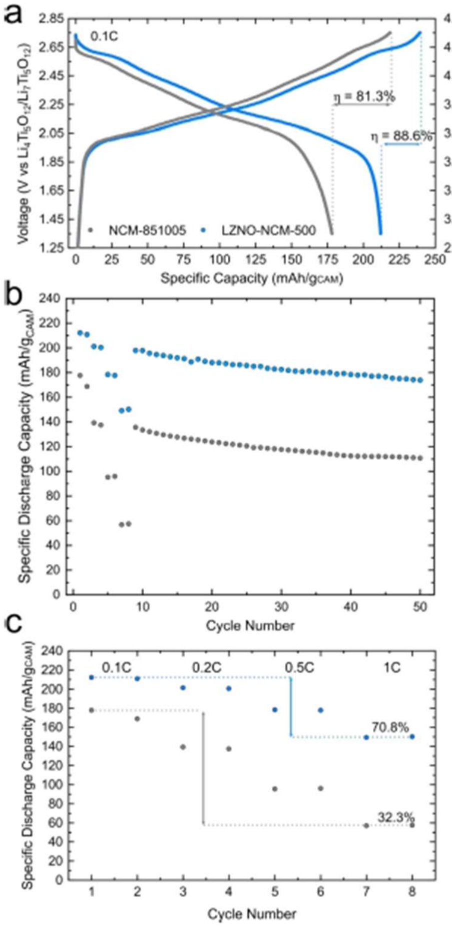

Figure 4. Electrochemical performance of bare NCM-851005 and LZNO-NCM-500 at 45 °C in pellet-stack SSB cells with an LTO anode and LPSCl as SE. a) First-cycle voltage profiles at 0.1 C and corresponding Coulombic efficiencies. b, c) Specific discharge capacities during rate capability testing, with two cycles each at 0.1 C, 0.2 C, 0.5 C and 1 C, followed by 0.2 C cycling. The percentage values in c) reflect the capacity retention at 1 C (8th cycle) relative to the first cycle at 0.1 C rate.

Interfacial degradation in lithium thiophosphate-based SSBs has already been studied in detail using X-ray photoelectron spectroscopy (XPS) and time-of-flight secondary ion mass spectrometry (ToF-SIMS), for example. SE oxidation, evident from the appearance of polysulfide and oxygenated sulfur/phosphorus species, typically occurs at the contact points between the particles upon charging, with the degree of interfacial degradation being significantly different for coated and uncoated CAMs.[5–8,14,18,24,33,34] The same is to be expected here. However, from the available literature reports, it is apparent that there are no clear trends of what coating chemistry and/or morphology works best in terms of suppressing the formation of certain degradation products.

Figure 4(b, c) shows the specific discharge capacities for rates between 0.1 C and 1 C. The overall performance of the LZNO-NCM-500 was clearly better than that of the uncoated CAM, with differences in capacity ranging from 30 to 90 mAh/g_{CAM}. At 1 C (2 mA/cm^2), a specific discharge capacity of approximately 150 mAh/g_{CAM} was achieved with the LZNO-NCM-500, corresponding to 71 % of the capacity at 0.1 C rate. In contrast, the bare NCM-851005 delivered a specific discharge capacity of approximately 57 mAh/g_{CAM}, corresponding to only 32% of the initial capacity. These results emphasize the improved charge-transfer kinetics through the modified CAM|SE interface. The large cell capacities afforded by the coated CAM were also reasonably stable with $q_{dis} \approx 174$ mAh/g_{CAM} at 0.2 C in the 50th cycle.

Furthermore, the cyclability of the LZNO-coated NCM-851005 CAMs in SSB cells was evaluated against that of three analogously prepared reference coatings (Figure S10, Supporting Information). These coatings had nominal n(Li):n(Nb) ratios of 1:1 (representing the $LiNbO_3$ stoichiometry), 1.5:1 (equal to LZNO but without Zn) and 3:1 (for Li_3NbO_4). As expected, all of them resulted in substantial improvements in cycling performance over the bare NCM-851005. Notably, the LZNO coating clearly outperformed the other Li–Nb–O-type protective coatings. Although the role of Zn is still largely unclear, its presence in the surface layer has a strong positive effect on the reversible capacity, rate capability and stability of the Ni-rich NCM CAM in SSBs with argyrodite Li_6PS_5Cl as SE. Because superior performance was also seen for the LZNO-NCM-300, the presence of crystalline components in the coating appears to play no major role though.

The long-term cycling stability of the two CAMs was also tested at 1 C (Figure 5a). As expected from the rate performance data shown in Figure 4(c), the LZNO-NCM-500 delivered superior specific capacities. While the bare NCM-851005 showed rapid capacity fading over the first 20 cycles, the capacity degradation of the LZNO-NCM-500 was found to occur more gradually. More than 81 % of the initial discharge capacity was retained after 200 cycles, compared to only 68 % for SSBs using the uncoated CAM, despite the much larger cumulative charge exchanged in the cells with the LZNO-NCM-500. Figure 5(b) shows the Coulombic efficiencies up to the 50th cycle. The LZNO-NCM-500 exhibited higher values throughout, with the differences being particularly significant over the first 20 cycles. This suggests faster formation of stable interfaces in the case of coated CAM. Nonetheless, the Coulombic efficiencies converged during the course of cycling and stabilized above 99.9 % after 60 cycles.

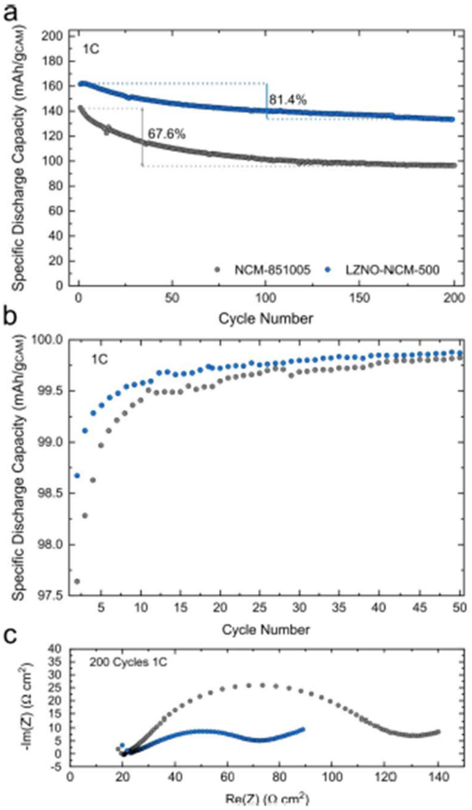

Figure 5. Electrochemical performance of bare NCM-851005 and LZNO-NCM-500 at 45 °C in pellet-stack SSB cells with an LTO anode and LPSCl as SE. a) Long-term cycling at 1 C rate. The percentage values indicate the capacity retention after 200 cycles. b) Corresponding Coulombic efficiencies from the 2nd cycle onward. c) Nyquist plots of the electrochemical impedance at 45 °C of representative cells after 200 cycles.

Finally, the SSBs after 200 cycles were examined by electrochemical impedance spectroscopy (EIS) and SEM. Figure 5(c) shows Nyquist plots from EIS measurements conducted on the cells using the bare and coated NCM-851005 in the discharged state. Semi-quantitative comparison of the depressed semicircles representing the interfacial cathode resistance indicated that this contribution is reduced by a factor of about two with the LZNO-NCM-500 CAM. This finding corroborates the differences in Coulombic efficiency discussed above.

Figure S11 (Supporting Information) shows cross-sectional SEM images at different magnifications of cathodes harvested from the cycled cells. In both cases, there were no signs of major (chemo)mechanical degradation (contact loss, particle fracture etc.), implying that the differences in cycling performance between bare NCM-851005 and LZNO-NCM-500 mainly arise from a different degree of (electro)chemical decomposition at the CAM|SE interface.

Conclusion

In conclusion, application of a facile wet chemistry-based synthesis route led to the formation of a promising composite coating, containing Li_3NbO_4 (or related) nanocrystals and Li_2CO_3, on a Ni-rich NCM cathode active material. Although the targeted phase $Li_6ZnNb_4O_{14}$ could not be stabilized, the presence of rocksalt-type Li_3NbO_4 expands the current perspective on Li–Nb–O derived protective coatings. The latter have thus far been present mostly in the form of (amorphous) $LiNbO_3$. Ultimately, the reported coating has proven to be highly beneficial to the cycling performance of argyrodite Li_6PS_5Cl-based solid-state battery cells, resulting in large capacities, high-rate capability and good capacity retention, and further shown to outperform conventional lithium niobate coating materials.

Experimental Section

Materials

$LiNi_{0.85}Co_{0.10}Mn_{0.05}O_2$ (NCM-851005, $d_{50} = 3.52$ µm, $d_{90} = 5.05$ µm; BASF SE) CAM was heated in O_2 at 750 °C for 3 h (5 °C/min heating rate) to reduce the amount of residual surface carbonates. 1 M lithium ethoxide solution was prepared by the reaction of absolute ethanol (Sigma-Aldrich; 99.8 %) with Li metal (Albemarle Germany GmbH). To prepare 0.5 M niobium ethoxide and 0.01 M zinc acetate solutions, $Nb(OCH_2CH_3)_5$ (Sigma-Aldrich; 99.95 %) or $Zn(O_2CCH_3)_2$ (Sigma-Aldrich) was dissolved in absolute ethanol.

Surface coating

For the preparation of LZNO-coated NCM-851005 (with a nominal coating content of 1 wt.%), the CAM powder (5.94 g) was added to a mixture of lithium ethoxide (512 µL), niobium ethoxide (683 µL) and zinc acetate (8500 µL) solutions in an Ar-filled glovebox, followed by 30 min ultrasonication of the dispersion. Subsequently, the reaction mixture was dried in a vacuum overnight. The resultant powder was ground using a mortar and pestle and heated in O_2 at 100, 300 or 500 °C for 2 h (5 °C/min heating rate).

Electrode preparation, cell assembly and testing

Cathode composite was prepared by mixing the bare or coated NCM-851005, Li_6PS_5Cl (LPSCl; NEI Corp.) and Super C65 carbon black (Timcal) in a ratio of 70 : 30 : 1 by weight in a planetary mill (Fritsch) at 140 rpm for 30 min. Using the same procedure, anode composite was prepared from carbon-coated $Li_4Ti_5O_{12}$ (LTO; NEI Corp.), LPSCl and Super C65 at a weight ratio of 30 : 60 : 10 (30 : 65 : 5 in Figure 5).

The electrochemical performance of the bare and coated NCM-851005 was tested in SSB cells using a custom-built setup comprising a polyether ether ketone sleeve and two stainless steel dies. 10 mm diameter pellet stacks were prepared starting from the separator layer, made by cold pressing 100 mg LPSCl at a uniaxial pressure of 62 MPa. They were finished by adding 65 mg anode composite and 12 mg cathode composite (approximately 2.9 mAh/cm^2, $q_{th} = 274$ mAh/g$_{CAM}$) and pressing the stack at 437 MPa. All cells were galvanostatically cycled at 45 °C in the voltage range 1.35–2.75 V vs. $Li_4Ti_5O_{12}/Li_7Ti_5O_{12}$ (approximately 2.9–4.3 V vs. Li^+/Li) while maintaining a uniaxial pressure of 81 MPa. Rate performance and stability tests were carried out at 0.1 C, 0.2 C, 0.5 C and 1 C, with two cycles at each rate, followed by further cycling at 0.2 C. Stability tests were performed at a rate of 1 C (1 C = 190 mA/g$_{CAM}$) for 200 cycles.

Methods

For compositional analysis, the LZNO-coated NCM-851005 was dissolved in acid using a graphite furnace. The Zn and Nb contents were determined by ICP-OES using a Thermo Fisher Scientific iCAP 7600 DUO. The C content was probed using a CS analyzer. Mass fractions represent the mean of at least three independent measurements.

SEM analysis was carried out at an accelerating voltage of 10 kV using a LEO-1530 electron microscope (Carl Zeiss AG) with a field emission source. Cross-sectional SEM images were taken from fractured electrode pellets after cycling.

ATR-IR spectroscopy was carried out using an ALPHA FT-IR spectrometer (Bruker), equipped with a Ge crystal.

TEM characterization was done using a double aberration corrected Themis-Z microscope (ThermoFisher Scientific) at an accelerating voltage of 300 kV, equipped with an OneView IS camera (AMETEK), a Super-X EDX detector (ThermoFisher Scientific) and a high-resolution GIF Continuum 970 (AMETEK) electron energy-loss spectrometer. 4D-STEM datasets were collected using the OneView IS camera with a screen current of approximately 10 pA, a small convergence semi-angle of 0.47 mrad and a camera length of 580 mm. Virtual imaging of the NBED patterns was done using DigitalMicrograph (version 3.42). Sample cross-sections were prepared using a dual-beam Ga FIB in a Strata 400 (ThermoFisher Scientific). Carbon layers were deposited by ion beam-induced deposition to protect the coating during sample preparation and processing. Initial thinning was performed at 30 kV. Final sample thinning and cleaning was done at 5 and 2 kV, respectively.

XRD patterns were collected from the samples using a Stadi-P diffractometer (STOE) with a Mo anode ($\lambda = 0.70926$ Å) and a MYTHEN 1 K strip detector (DECTRIS AG) in Debye-Scherrer geometry. The instrumental contribution to the reflection broadening was obtained by measuring a NIST 640f Si standard reference material. Rietveld refinement was performed using GSAS-II.[35] During refinement, the scale factor, zero shift and crystallite size broadening parameters were allowed to vary. Sample absorption was calculated based on the capillary diameter of 0.3 mm and a powder packing density of 1.44 g/cm^3. A Chebyshev polynomial function with 17 terms was used to fit a fixed background to the data. Unit cell parameters, oxygen site position and atomic displace parameters (isotropic, u_{iso}) for each site were refined. Atoms occupying the same site were constrained to have the same atomic parameters. Site occupancy factors were constrained such that each site remained fully occupied.

In situ heating XRD of a volume mixture of the LZNO coating was performed using a diffractometer equipped with a microfocus Mo $K_{\alpha 1,2}$ rotating anode and a Pilatus 300 K-W area detector.[36] The precursor material was prepared by combining the Li, Nb and Zn solutions, followed by 30 min ultrasonication and solvent evaporation, as described above. It was packed into a sapphire capillary and heated at 1 °C/min under O_2 flow in a custom-built gas-flow furnace based on the design of Chupas *et al.* while recording XRD patterns every 10 min.[37] Temperature calibration was carried out using the unit-cell volume evolution of an Al_2O_3 reference material during application of the same heating profile.[38]

EIS was conducted on SSB cells after 200 cycles at frequencies from 7 MHz to 100 mHz (10 mV amplitude) using an SP-300 impedance analyzer (Bio-Logic Science Instruments Ltd.).

Acknowledgements

This study was supported by BASF SE. The authors acknowledge the support from the Karlsruhe Nano Micro Facility (KNMF, www.knmf.kit.edu), a Helmholtz research infrastructure at Karlsruhe Institute of Technology (KIT, www.kit.edu). D.K. and F.S. acknowledge the Fonds der Chemischen Industrie (FCI) for financial support through Kekulé and Liebig fellowships. Y.T. acknowledges the financial support from the German Research Foundation (DFG) under project ID 390874152 (POLiS Cluster of Excellence). The authors thank Dr. Damian Goonetilleke (INT, KIT) for help with the Rietveld refinement analysis, Dr. Thomas Bergfeldt (IAM-AWP, KIT) for ICP-OES measurements, as well as Leonhard Karger (INT, KIT) and Dr. Holger Geßwein (IAM-ESS, KIT) for assistance with the in situ XRD experiment. They also thank Dr. Jörn Kulisch (BASF SE, Ludwigshafen) and Dr. Pascal Hartmann (BASF SE, Ludwigshafen) for fruitful discussions. Open Access funding enabled and organized by Projekt DEAL.

Conflict of Interest

The authors declare no conflict of interest.

Data Availability Statement

The data that support the findings of this study are available from the corresponding author upon reasonable request.

Keywords: all-solid-state battery · lithium nickel cobalt manganese oxide cathode · lithium niobate · lithium thiophosphate solid electrolyte · sol-gel coating

[1] J. Janek, W. G. Zeier, *Nat. Energy* **2016**, *1*, 16141.
[2] Y.-K. Sun, *ACS Energy Lett.* **2020**, *5*, 3221–3223.
[3] S. Randau, D. A. Weber, O. Kötz, R. Koerver, P. Braun, A. Weber, E. Ivers-Tiffée, T. Adermann, J. Kulisch, W. G. Zeier, F. H. Richter, J. Janek, *Nat. Energy* **2020**, *5*, 259–270.
[4] Y. Kato, S. Hori, T. Saito, K. Suzuki, M. Hirayama, A. Mitsui, M. Yonemura, H. Iba, R. Kanno, *Nat. Energy* **2016**, *1*, 16030.
[5] A. Banerjee, X. Wang, C. Fang, E. A. Wu, Y. S. Meng, *Chem. Rev.* **2020**, *120*, 6878–6933.
[6] J. Auvergniot, A. Cassel, J.-B. Ledeuil, V. Viallet, V. Seznec, R. Dedryvère, *Chem. Mater.* **2017**, *29*, 3883–3890.
[7] S. Sun, C.-Z. Zhao, H. Yuan, Y. Lu, J.-K. Hu, J.-Q. Huang, Q. Zhang, *Mater. Futures* **2022**, *1*, 012101.
[8] F. Walther, R. Koerver, T. Fuchs, S. Ohno, J. Sann, M. Rohnke, W. G. Zeier, J. Janek, *Chem. Mater.* **2019**, *31*, 3745–3755.
[9] F. Strauss, D. Kitsche, Y. Ma, J. H. Teo, D. Goonetilleke, J. Janek, M. Bianchini, T. Brezesinski, *Adv. Energy Sustain. Res.* **2021**, *2*, 2100004.
[10] K. J. Kim, M. Balaish, M. Wadaguchi, L. Kong, J. L. M. Rupp, *Adv. Energy Mater.* **2021**, *11*, 2002689.
[11] Y. Li, Z. Gao, F. Hu, X. Lin, Y. Wei, J. Peng, J. Yang, Z. Li, Y. Huang, H. Ding, *Small Methods* **2020**, *4*, 2000111.
[12] S. P. Culver, R. Koerver, W. G. Zeier, J. Janek, *Adv. Energy Mater.* **2019**, *9*, 1900626.
[13] K. Takada, N. Ohta, L. Zhang, K. Fukuda, I. Sakaguchi, R. Ma, M. Osada, T. Sasaki, *Solid State Ionics* **2008**, *179*, 1333–1337.
[14] F. Walther, F. Strauss, X. Wu, B. Mogwitz, J. Hertle, J. Sann, M. Rohnke, T. Brezesinski, J. Janek, *Chem. Mater.* **2021**, *33*, 2110–2125.
[15] A.-Y. Kim, F. Strauss, T. Bartsch, J. H. Teo, T. Hatsukade, A. Mazilkin, J. Janek, P. Hartmann, T. Brezesinski, *Chem. Mater.* **2019**, *31*, 9664–9672.
[16] D. Kitsche, Y. Tang, Y. Ma, D. Goonetilleke, J. Sann, F. Walther, M. Bianchini, J. Janek, T. Brezesinski, *ACS Appl. Energy Mater.* **2021**, *4*, 7338–7345.
[17] Y. Ito, Y. Sakurai, S. Yubuchi, A. Sakuda, A. Hayashi, M. Tatsumisago, *J. Electrochem. Soc.* **2015**, *162*, A1610–A1616.
[18] H. Visbal, Y. Aihara, S. Ito, T. Watanabe, Y. Park, S. Doo, *J. Power Sources* **2016**, *314*, 85–92.
[19] P. Heitjans, M. Masoud, A. Feldhoff, M. Wilkening, *Faraday Discuss.* **2007**, *134*, 67–82.
[20] V. V. Konovalova, V. V. Fomichev, D. V. Drobot, R. M. Zakalyukin, S. Yu. Stefanovich, *Russ. J. Inorg. Chem.* **2009**, *54*, 1650–1654.
[21] Y. Li, M. P. Paranthaman, L. W. Gill, E. W. Hagaman, Y. Wang, A. P. Sokolov, S. Dai, C. Ma, M. Chi, G. M. Veith, A. Manthiram, J. B. Goodenough, *J. Mater. Sci.* **2016**, *51*, 854–860.
[22] F. Strauss, J. H. Teo, J. Maibach, A.-Y. Kim, A. Mazilkin, J. Janek, T. Brezesinski, *ACS Appl. Mater. Interfaces* **2020**, *12*, 57146–57154.
[23] Y. Ma, J. H. Teo, D. Kitsche, T. Diemant, F. Strauss, Y. Ma, D. Goonetilleke, J. Janek, M. Bianchini, T. Brezesinski, *ACS Energy Lett.* **2021**, *6*, 3020–3028.
[24] S. H. Jung, K. Oh, Y. J. Nam, D. Y. Oh, P. Brüner, K. Kang, Y. S. Jung, *Chem. Mater.* **2018**, *30*, 8190–8200.
[25] J.-C. Grenier, C. Martin, A. Durif, *Bull. Soc. Fr. Mineral. Cristallogr.* **1964**, *87*, 316–320.
[26] D. R. Modeshia, R. I. Walton, M. R. Mitchell, S. E. Ashbrook, *Dalton Trans.* **2010**, *39*, 6031–6036.
[27] Y.-J. Hsiao, T.-H. Fang, S.-J. Lin, J.-M. Shieh, L.-W. Ji, *J. Lumin.* **2010**, *130*, 1863–1865.
[28] A.-Y. Kim, F. Strauss, T. Bartsch, J. H. Teo, J. Janek, T. Brezesinski, *Sci. Rep.* **2021**, *11*, 5367.
[29] F. Xin, H. Zhou, Y. Zong, M. Zuba, Y. Chen, N. A. Chernova, J. Bai, B. Pei, A. Goel, J. Rana, F. Wang, K. An, L. F. J. Piper, G. Zhou, M. S. Whittingham, *ACS Energy Lett.* **2021**, *6*, 1377–1382.
[30] F. Xin, H. Zhou, J. Bai, F. Wang, M. S. Whittingham, *J. Phys. Chem. Lett.* **2021**, *12*, 7908–7913.
[31] R. J. Clément, Z. Lun, G. Ceder, *Energy Environ. Sci.* **2020**, *13*, 345–373.
[32] N. Yabuuchi, M. Takeuchi, M. Nakayama, H. Shiiba, M. Ogawa, K. Nakayama, T. Ohta, D. Endo, T. Ozaki, T. Inamasu, K. Sato, S. Komaba, *Proc. Natl. Acad. Sci. USA* **2015**, *112*, 7650–7655.
[33] S.-K. Jung, H. Gwon, S.-S. Lee, H. Kim, J. C. Lee, J. G. Chung, S. Y. Park, Y. Aihara, D. Im, *J. Mater. Chem. A* **2019**, *7*, 22967–22976.
[34] J. H. Teo, F. Strauss, F. Walther, Y. Ma, S. Payandeh, T. Scherer, M. Bianchini, J. Janek, T. Brezesinski, *Mater. Futures* **2022**, *1*, 015102.
[35] B. H. Toby, R. B. Von Dreele, *J. Appl. Crystallogr.* **2013**, *46*, 544–549.
[36] L. de Biasi, G. Lieser, J. Rana, S. Indris, C. Dräger, S. Glatthaar, R. Mönig, H. Ehrenberg, G. Schumacher, J. R. Binder, H. Geßwein, *CrystEngComm* **2015**, *17*, 6163–6174.
[37] P. J. Chupas, K. W. Chapman, C. Kurtz, J. C. Hanson, P. L. Lee, C. P. Grey, *J. Appl. Crystallogr.* **2008**, *41*, 822–824.
[38] G. W. Stinton, J. S. O. Evans, *J. Appl. Crystallogr.* **2007**, *40*, 87–95.

Manuscript received: December 15, 2021
Revised manuscript received: February 26, 2022

3.3 Publication III: Atomic Layer Deposition Derived Zirconia Coatings on Ni-Rich Cathodes in Solid-State Batteries: Correlation Between Surface Constitution and Cycling Performance

Based on the successful use of ALD presented in Publication I, the focus was set to ZrO_2. After slight adjustments to the TEMAH/O_3 process, zirconia could be conformally coated onto NCM85 using TEMAZ and ozone, yielding a virtually constant GPC. Due to the important influence of a post-annealing step on the performance of HfO_2@NCM85 in the seminal study, the role of a heat treatment step was emphasized in this study. Therefore, a set of ZrO_2@NCM85 samples annealed at temperatures between 300 and 700 °C was studied systematically.

It was shown that heat treatment has a number of effects on the coated CAM, including changes in the ZrO_2 crystal size/structure and the coating morphology. Furthermore, Zr^{4+} ion diffusion into the NCM and the formation of a resistive interlayer were observed to result from annealing at elevated temperatures. The impact on the electrochemical performance in LPSCl-based SSB cells of the as-modified CAMs was significant. Moderate temperatures (~400 °C) proved to be beneficial while high temperatures (≥ 500 °C) turned out to affect the performance drastically in a negative way. The results show that protective surface layers need to be carefully optimized, since several coating-related phenomena are occurring in parallel upon post-heat treatment. Ultimately, the study demonstrates that ALD-derived model-type coatings represent a viable platform to study the property-performance relations of coatings.

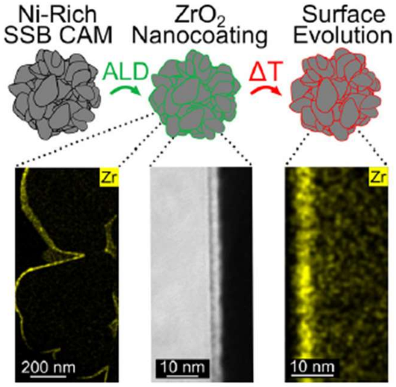

Figure 10: Table of Contents graphic of Publication III. “The secondary particles of the cathode material $LiNi_{0.85}Co_{0.10}Mn_{0.05}O_2$ are conformally coated with ZrO_2 nanoshells making use of the unique capabilities of atomic layer deposition (ALD). The multifaceted evolution of the surface structure upon post-heat treatment and its effect on the cycling performance of thiophosphate-based solid-state batteries are studied systematically.“ Reprinted from reference [80].

The experiments were planned by the first author under the supervision of M. Bianchini, A. Kondrakov, J. Janek and T. Brezesinski. The first author optimized the ALD process, prepared the modified CAM samples, performed the XRD characterization, tested their electrochemical performance in SSB cells and conducted post mortem impedance measurements and sample recovery. Y. Tang performed the TEM investigation together with the first author, including sample preparation and data analysis. H. Hemmelmann conducted the XPS experiments. F. Walther carried out the post mortem ToF-SIMS investigation and the analysis of the corresponding data. The manuscript was written by the first author and edited by Y. Tang, F. Walther, M. Bianchni, J. Janek and T. Brezesinski.

Reprinted from D. Kitsche, Y. Tang, H. Hemmelmann, F. Walther, M. Bianchini, A. Kondrakov, J. Janek, T. Brezesinski, *Small Sci.* **2022**, *2*, 2200073.

Atomic Layer Deposition Derived Zirconia Coatings on Ni-Rich Cathodes in Solid-State Batteries: Correlation Between Surface Constitution and Cycling Performance

*David Kitsche, Yushu Tang, Hendrik Hemmelmann, Felix Walther, Matteo Bianchini, Aleksandr Kondrakov, Jürgen Janek, and Torsten Brezesinski**

Protective coatings are required to address interfacial incompatibility issues in composite cathodes made from Ni-rich layered oxides and lithium thiophosphate solid electrolytes (SEs), one of the most promising combinations of materials for high energy and power density solid-state battery (SSB) applications. Herein, the preparation of conformal ZrO_2 nanocoatings on a $LiNi_{0.85}Co_{0.10}Mn_{0.05}O_2$ (NCM85) cathode-active material (CAM) by atomic layer deposition (ALD) is reported and the structural and chemical evolution of the modified NCM85 upon heat treatment—a post-processing step often required to boost battery performance—is investigated. The coating properties are shown to have a strong effect on the cyclability of high-loading SSB cells. After mild annealing (≈400 °C), the CAM delivers high specific capacities (≈200 mAh g^{-1} at C/10) and exhibits improved rate capability (≈125 mAh g^{-1} at 1C) and stability (≈78% capacity retention after 200 cycles at 0.5C), enabled by effective surface passivation. In contrast, annealing temperatures above 500 °C lead to the formation of an insulating interphase that negatively affects the cycling performance. The results of this study demonstrate that the preparation conditions for a given SE/CAM combination need to be tailored carefully and ALD is a powerful surface-engineering technique toward this goal.

1. Introduction

Solid-state batteries (SSBs) are the focus of research and public interest, especially because of the demand for safe electric vehicles with higher ranges and faster charging.[1–3] This calls for materials enabling high energy densities and high (effective) ionic conductivities. When it comes to bulk-type SSBs, the combination of thiophosphate (sulfide) solid electrolytes (SEs) and Ni-rich layered oxide cathode-active materials (CAMs), such as $LiNi_xCo_yMn_zO_2$ (commonly referred to as NMC or NCM), is among those with the best chance of meeting these requirements. The main reasons for this are the unmatched room-temperature ionic conductivities of lithium thiophosphates[4] and the high specific capacities and half-cell potentials of the technologically mature Ni-rich NCM CAMs.[5] Apart from the challenge of realizing the practical use of lithium-metal or silicon anodes, a key requirement is the successful engineering of stable interfaces in SSBs.[6] This applies especially to composite cathodes made from the aforementioned materials, which are typically operated at cell voltages above 4.0 V.

The degradation of lithium thiophosphates and potential mitigation strategies have been investigated in depth in the past decade.[6–9] Oxides, such as the prototype compound $LiNbO_3$ and related stoichiometries, have been studied most extensively as coating materials, due to their stability and relative ease of preparation.[7,10–15] For example, Zr-based coatings in the form of ZrO_x or $Li_xZr_yO_z$ have been shown to be promising, with excellent cyclability of large-format SSB cells demonstrated by Samsung.[16–21] These oxides were deposited onto the CAMs by various chemical and physical techniques.[7] Among these,

---

D. Kitsche, M. Bianchini, A. Kondrakov, J. Janek, T. Brezesinski
Battery and Electrochemistry Laboratory (BELLA)
Institute of Nanotechnology
Karlsruhe Institute of Technology (KIT)
Hermann-von-Helmholtz-Platz 1, 76344 Eggenstein-Leopoldshafen, Germany
E-mail: torsten.brezesinski@kit.edu

The ORCID identification number(s) for the author(s) of this article can be found under https://doi.org/10.1002/smsc.202200073.

DOI: 10.1002/smsc.202200073

Y. Tang
Institute of Nanotechnology
Karlsruhe Institute of Technology (KIT)
Hermann-von-Helmholtz-Platz 1, 76344 Eggenstein-Leopoldshafen, Germany

H. Hemmelmann, F. Walther, J. Janek
Institute of Physical Chemistry & Center for Materials Research (ZfM/LaMa)
Justus-Liebig-University Giessen
Heinrich-Buff-Ring 17, 35392 Giessen, Germany

M. Bianchini, A. Kondrakov
BASF SE
Carl-Bosch-Strasse 38, 67056 Ludwigshafen am Rhein, Germany

atomic layer deposition (ALD) stands out because of the unique capability of depositing conformal, (sub-)nanometer films on complex substrates.[22,23] In liquid electrolyte-based lithium-ion batteries (LIBs), ALD coatings have already been proven to increase the cycle life.[24–29] The same approach can be used for application in the SSB context, but the coating chemistry might vary.[7,29] In fact, the deposition of several Li-containing ternary oxides (attractive because of favorable ionic conductivities) has been reported.[30–32] However, only a few studies have demonstrated a beneficial effect of ALD CAM coatings in bulk-type SSB cells, e.g., for the SE/CAM combinations $Li_{3.15}Ge_{0.15}P_{0.85}S_4$ (LGPS)|Al_2O_3@$LiCoO_2$ (LCO),[33] Li_6PS_5Cl (LPSCl)|HfO_2@NCM851005,[34] LGPS|$LiNbO_x$@NCM811,[35] and LPSCl|LiO_x-ZrO_x@LCO.[20] The latter study revealed a superior performance of the Li-containing coating over the binary counterpart ZrO_x in terms of rate capability and stability, which the authors attributed to improved ion migration across the SE|CAM interface. This is usually the rationale behind using ternary oxide coatings.[7] Lithium incorporation into protective films can be achieved either directly by adding a lithium source along with the other precursors during synthesis[17,19,36] or indirectly by an annealing step after coating, aiming at the reaction of residual lithium present on the CAM surface with the initially binary oxide coating.[37] Considering that the ALD of Li-based compounds is not trivial,[38] it seems necessary to further explore the indirect route.

In the present work, we focus on ALD-derived zirconia nanocoatings on $LiNi_{0.85}Co_{0.10}Mn_{0.05}O_2$ (hereafter referred to as ZrO_2@NCM85) and systematically study the influence of post-heat treatment on the CAM surface structure, composition, and morphology. In addition, we examine its effect on the cycling performance of the resulting ZrO_2@NCM85 samples in pelletized SSB cells with an argyrodite LPSCl SE and a $Li_4Ti_5O_{12}$ (LTO) composite anode. Post-mortem investigations were also carried out to gain insights into the electro-chemo-mechanical degradation of the cathodes and to identify persisting stability issues.

2. Results and Discussion

Prior to ALD, the NCM85 CAM was heated for 3 h in O_2 flow at 750 °C, resulting in a carbonate content of ≈0.5 wt%.[34,39] This step helped to avoid too high levels of residual lithium, which has been shown to limit the performance both in LIB and SSB cells,[17,40] and further to improve the reliability of the coating process. Tetrakis(ethylmethylamido)zirconium(IV) (TEMAZ) and ozone were used to deposit ZrO_2 onto the CAM secondary particles at a reactor temperature of 250 °C, an established procedure for the preparation of high-quality zirconia films.[41] Although ZrO_2 ALD with H_2O as a counter reactant is feasible, O_3 was chosen based on previous cycling data obtained on HfO_2-coated NCM85 in analogous SSB cells.[34] **Figure 1** shows a plot of the mass fraction of ZrO_2 determined by inductively coupled plasma-optical emission spectroscopy (ICP-OES) and the corresponding estimated film thickness on the CAM substrate as a function of the number of ALD cycles. The relationship was virtually linear, with a growth per cycle of ≈0.09 wt% ZrO_2. Depositions on 2–8 g batches were found to follow the same trend, suggesting good saturation of the NCM85 surface by the

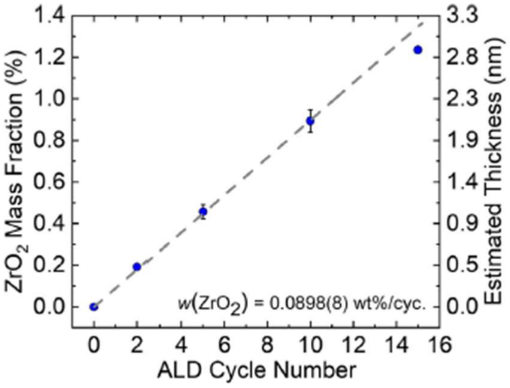

Figure 1. ZrO_2 mass fraction and estimated film thickness on the NCM85 substrate depending on the number of tetrakis(ethylmethylamido) zirconium(IV) (TEMAZ)/O_3 atomic layer deposition (ALD) cycles. The error bars indicate the standard deviation of measurements conducted on different batches of the ZrO_2@NCM85. The gray dashed line is a linear fit to the data with a fixed *y*-axis intercept at zero.

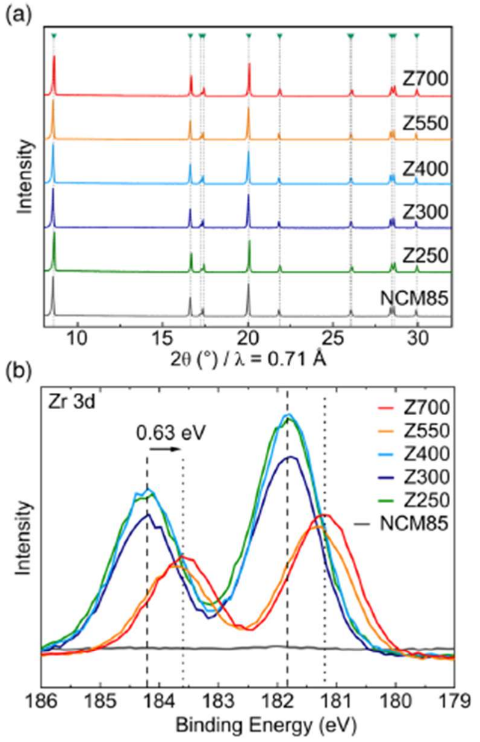

Figure 2. a) X-ray diffraction (XRD) patterns of the uncoated NCM85 CAM and the ZrO_2@NCM85 sample series. The arrows and drop lines indicate the expected Bragg positions (*R*−3 *m* space group). b) X-ray photoelectron spectroscopy (XPS) data (Zr 3d core-level region) collected from the uncoated and coated materials. The dashed and dotted lines denote the shift in binding energy between the peak maxima for Z250 and Z700.

pulsing sequence utilized in this work. The method is therefore suited for precisely tailoring the coating content/thickness. The thickness t can be estimated as follows: $t = wm/\rho A$, where A and m represent the free surface area and total mass of the sample, respectively, and ρ and w are the density and mass fraction of the coating material. The growth rate amounted to ≈0.21 nm per ALD cycle. However, estimates using the Brunauer–Emmett–Teller (BET) surface area of the substrate, $A_{\mathrm{BET}} = 0.71\ \mathrm{m}^2\,\mathrm{g}_{\mathrm{NCM85}}{}^{-1}$, and the crystallographic density of tetragonal ZrO_2, $\rho = 6.1\ \mathrm{g\,cm}^{-3}$, should be considered as lower bounds, since the actual coating density and area are probably somewhat lower.

Screening of the cycling performance in SSB cells revealed major improvements in capacity and rate capability for the as-coated CAMs (after 5, 10, and 15 TEMAZ/O_3 ALD cycles, see Figure S1, Supporting Information). While showing similar initial specific capacities, the 10 ALD cycle sample (≈0.9 wt% ZrO_2) delivered larger reversible capacities in the later cycles, especially at higher rates. Because previous studies have shown that the post-treatment has a strong effect on the performance of CAMs coated with binary oxides,[34,37,42] we decided to investigate the impact of such a processing step in a systematic manner, with emphasis placed on the annealing temperature.

To facilitate characterization of the protective coating while maintaining good cyclability, the 15 ALD cycle sample (with ≈1.2 wt% ZrO_2) was selected for post-treatment in O_2 at temperatures of 300, 400, 550, and 700 °C (hereafter referred to as Z300–Z700, with Z250 denoting the as-coated ZrO_2@NCM85). The crystal structure of the resulting CAMs was examined by X-ray diffraction (XRD, **Figure 2**a). The experimental patterns can be indexed in the space group $R-3\,m$. Furthermore, Rietveld refinement analysis of the diffraction data indicated that the bulk structure remains virtually unaffected by ALD coating and annealing (see Table S1 and Figure S2, Supporting Information).

The surface of the ZrO_2@NCM85 CAMs was probed using X-ray photoelectron spectroscopy (XPS). Figure 2b shows detailed spectra of the Zr 3d core-level regions. The presence of ZrO_2 (Zr^{4+}) is evident from the characteristic doublet peak, with the $3d_{5/2}$ line centered at ≈181.8 eV and the $3d_{3/2}$ line at ≈184.2 eV for Z250, Z300, and Z400. The spectrum barely changed upon annealing at moderate temperatures, suggesting a similar chemical environment of the zirconium ions at the

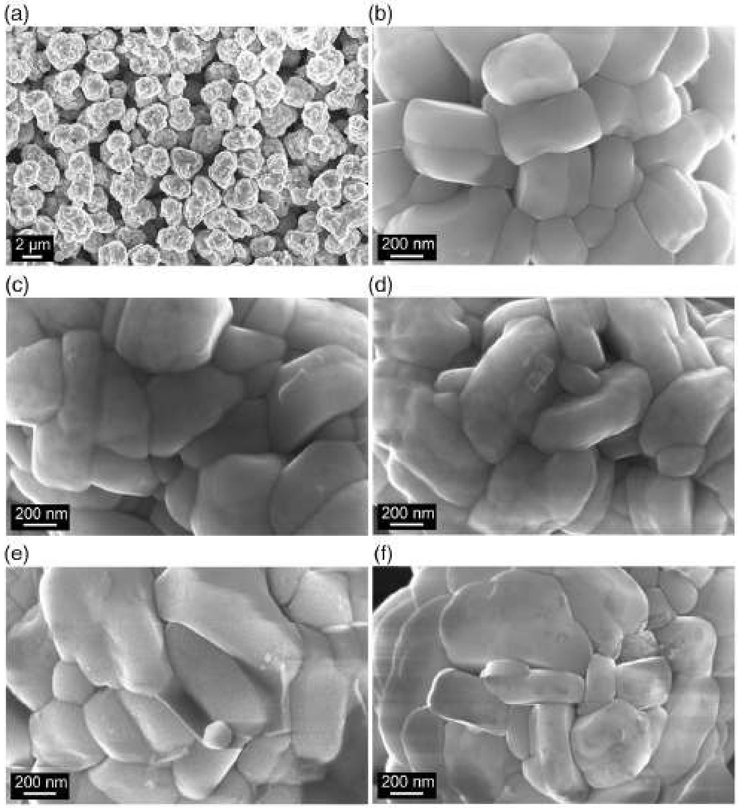

Figure 3. a–f) Top-view scanning electron microscopy (SEM) images of: the uncoated NCM85 (a,b) and ZrO_2@NCM85 (c–f) CAMs, with Z250 (c), Z400 (d), Z550 (e), and Z700 (f).

surface. However, there was a distinct peak shift toward lower binding energies for Z550 and Z700, possibly indicating a reaction and/or interaction of the coating with the NCM85 substrate. Recent reports on similar systems have shown that this decrease in binding energy results from the formation of lithium metal oxides.[37] Such compounds are believed to be beneficial to the CAM performance, due to superior ionic conductivity over the respective (Li-free) binary oxides. Nevertheless, it should be noted that Zr^{4+} diffusion into the outermost layer of the NCM85 would also result in a detectable change in the zirconium environment.

The different samples were further investigated by scanning electron microscopy (SEM, **Figure** 3a–f). Neither coating nor post-annealing was found to have a direct effect on the CAM morphology. Closer inspection at higher magnification revealed the presence of a surface shell. In addition, increasing surface roughness was noticed for Z550 and Z700, suggesting an altered coating microstructure and decreasing uniformity above a certain threshold temperature.

Furthermore, transmission electron microscopy (TEM) imaging was done on focused ion beam (FIB)-prepared particle cross-sections to gain more detailed insights into the nature of the nanocoating (**Figure** 4a–d). Uniform secondary particle coverage was confirmed by high-angle annular dark-field scanning TEM (HAADF-STEM) combined with energy-dispersive X-ray spectroscopy (EDS). Deposition onto the grain boundaries in the particle interior was not observed. At first glance, the Zr signal in Figure 4a may suggest otherwise, but it originated from areas (on the secondary particle surface) that were not removed during FIB preparation. The coating had a thickness of 4–5 nm, thus exceeding the 2.9 nm estimate, as expected. HAADF-STEM corroborated the SEM observation of increasing surface roughness with increasing annealing temperature (see Figure 4b and Figure S3, Supporting Information). High-resolution TEM (HRTEM) investigations indicated that the coating consists of tetragonal ZrO_2 nanoparticles (Figure 4c) (space group $P4_2/nmc$, see fast Fourier transform (FFT) pattern in the inset), which grow with increasing post-treatment temperature, from 4 to 5 nm for Z250 to 7 to 8 nm for Z550 (see Figure S4, Supporting Information). This kind of crystal growth/coalescence apparently gives rise to increasing surface roughness. After heating at 550 °C, some of the crystals appeared to have undergone a phase transition toward monoclinic ZrO_2. This is indicated by an additional reflection in the FFT pattern pointing at the baddeleyite structure (space group $P2_1/c$, see Figure S5, Supporting Information). We note that the phase transformation is in agreement with the dependency of the ZrO_2 crystal structure on particle size.[43,44] Surprisingly, the crystallinity of the protective coating was partially lost at 700 °C (see Figure S6, Supporting Information). From the data, it appears that an amorphous layer formed in some regions of the surface that cannot be easily distinguished from the bulk NCM85. Unlike other studies, no

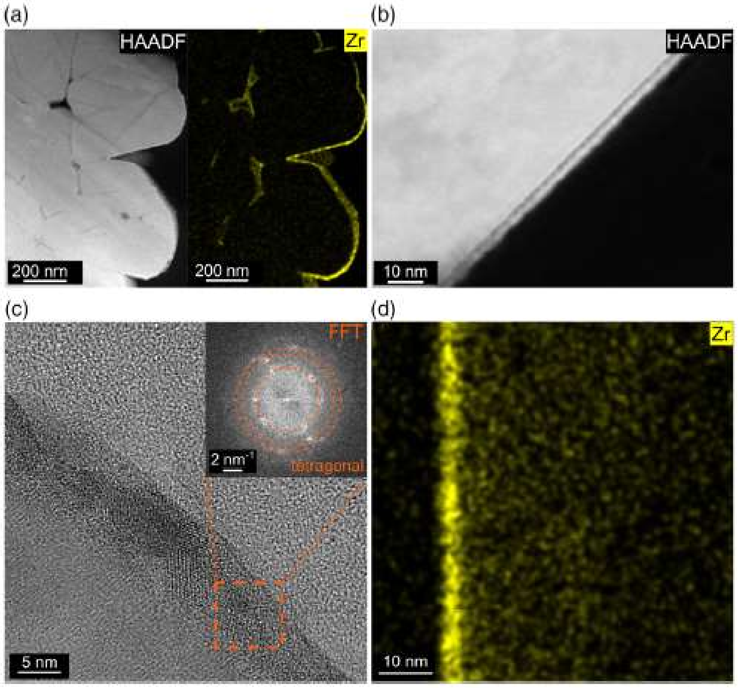

Figure 4. Electron microscopy of focused ion beam (FIB)-prepared particle cross-sections of the ZrO_2@NCM85 CAMs. a) Low-magnification high-angle annular dark-field scanning TEM (HAADF-STEM) image of Z550 and corresponding elemental map of Zr. b) High-magnification HAADF-STEM image showing the surface layer for Z400. c) HRTEM image of Z250 with fast Fourier transform (FFT) pattern (inset) of the crystalline coating. d) Zr elemental map collected from Z700.

evidence for the formation of crystalline Li_2ZrO_3 was found.[26] Instead, zirconium diffused into the subsurface volume of the layered oxide, as indicated by EDS (Figure 4d).

The zirconium concentration was found to decrease with increasing depth from the NCM85 (outer) surface (**Figure 5**a,b), eventually reaching the physical detection limit after ≈40 nm. The diffusion coefficient (700 °C) was estimated at $D \approx 3.8 \times 10^{-16}$ cm^2 s^{-1} from the corresponding STEM-EDS data (see Supporting Information for details). In contrast, there was no (detectable) zirconium diffusion for annealing temperatures of $\vartheta \leq 550$ °C. Zr^{4+} doping of layered Ni-rich cathodes at elevated temperatures (starting from NCM with a Zr-containing surface layer) has been reported previously.[26,45] In a study by Aurbach et al., diffusion into $LiNi_{0.8}Co_{0.1}Mn_{0.1}O_2$ was observed at 700 °C.[45] In another work on ALD-derived ZrO_2 coatings on $LiNi_{0.6}Co_{0.2}Mn_{0.2}O_2$, the authors found signs of minor diffusion into the outer surface of the CAM at 500 °C already.[26] While these studies reported on bulk diffusion (on the micrometer scale) with annealing of the coated materials at $\vartheta \geq 700$ °C, the lower diffusion depths observed here probably result from shorter dwell times. Overall, our findings agree with the trend that (Zr-based) coatings can act as dopants, at least to some degree, depending on the temperature.

The TEM characterization was further complemented by electron energy loss spectroscopy (EELS) studies to learn about potential reactions/interactions between coating and CAM. Specifically, STEM-EELS measurements were conducted on both Z250 and Z700, focusing on the Ni and O states in the surface and subsurface regions of the NCM85 (**Figure 6**a,b). The spectra collected from Z700 showed clear signs of altered chemical environments. The pre-peak of the O-K edge at ≈529 eV was strongly suppressed over the first 8 nm from the surface toward the bulk (denoted by the dotted rectangle), while this only applied to 2 nm for Z250. The suppression of the pre-peak, which represents a transition into a σ^* hybrid orbital of O 2p and Ni 3d states, was suggested to originate from the presence of oxygen vacancies.[46] These vacancies result from oxygen release, which becomes increasingly favorable with progressing delithiation.[47] Recently, (sub)surface oxygen loss during battery operation has been identified as a degradation mechanism in $Li(Ni_{1/3}Co_{1/3}Mn_{1/3})O_2$ cathodes using a $Li_2S-P_2S_5$ SE.[48] For Z700, this might be due to maintaining charge balance upon lithium migration into or reaction with the ZrO_2, which has been reported previously for protective alumina coatings on NCM.[37] The spectra also showed partial suppression of the right shoulder of the Ni–L3 edge (≈855.5 eV, denoted by blue arrows) and a more pronounced low-loss portion of the peak (≈854 eV) compared with Z250, especially in the first 10 nm. This is indicative of surface Ni reduction and formation of a rocksalt-like NiO layer, which could be explained by the aforementioned oxygen release.[49] The presence of such an insulating phase has been shown to negatively affect the cycling performance.[47] Apart from that, a structurally

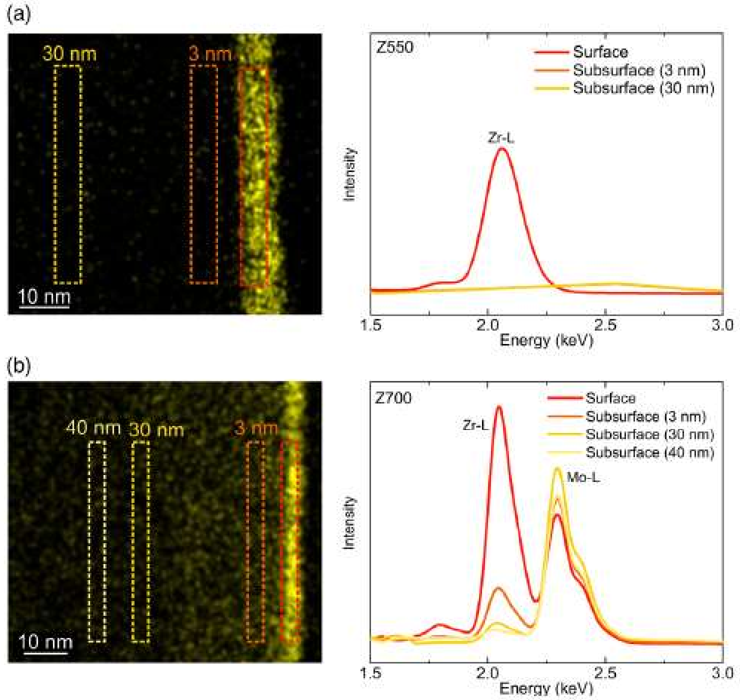

Figure 5. a,b) Zr elemental maps for FIB-prepared particle cross-sections of Z550 (a) and Z700 (b) with corresponding spectra from STEM-EDS in the energy range of the Zr–L edge. The colored rectangles indicate the areas on and below the NCM85 surface, where the spectra were acquired. The Mo signal originates from the sample holder.

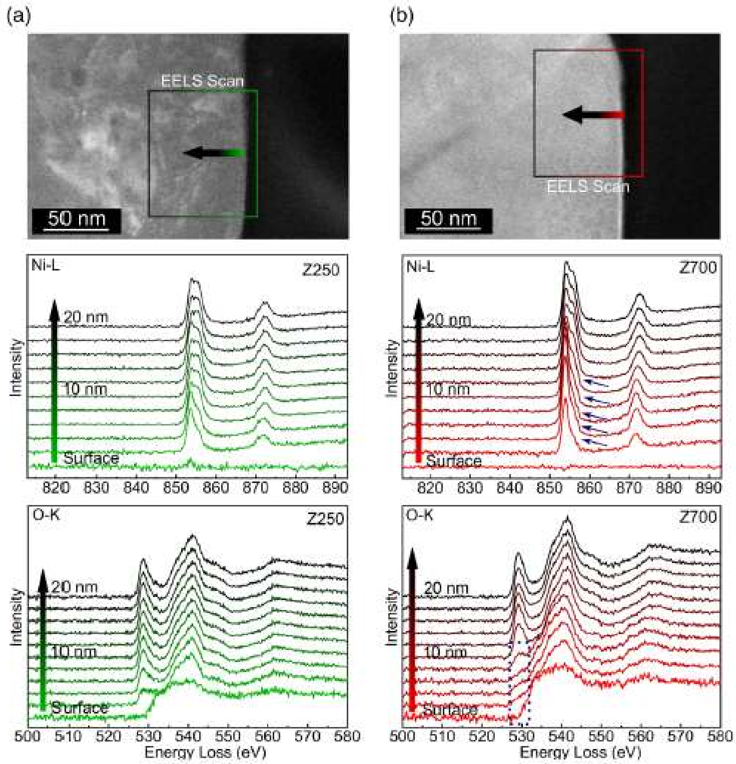

Figure 6. a,b) Electron energy loss (EEL) spectra at the Ni–L and O–K edges of the NCM85 (sub)surface for Z250 (a) and Z700 (b). The green and red squares indicate the areas probed. Spectra were recorded every 2 nm. Evident changes to the near-surface region of the CAM annealed at 700 °C are highlighted.

distorted (dislocations, etc.) interlayer between coating and CAM was found by high-resolution STEM (see Figure S7, Supporting Information).

The materials prior to and after coating were tested electrochemically in bulk-type SSBs at 45 °C using argyrodite LPSCl ($\sigma_{\mathrm{ion}} \approx 2\ \mathrm{mS\ cm^{-1}}$ at room temperature) as SE in the separator and the electrodes. LTO served as anode-active material in this work. XRD patterns of both LPSCl and LTO are shown in Figure S8, Supporting Information. The cells were cycled in the voltage range 1.35–2.75 V (≈2.9–4.3 V vs Li^+/Li) to explore the influence of the CAM coating and post-treatment on the cycling performance and stability. **Figure 7**a shows the voltage profiles of representative cells in the initial cycle at 0.1C. As expected, the specific charge capacity was reduced for the ZrO_2@NCM85 samples, especially for Z550 and Z700. However, the reversible capacities achieved with Z250, Z300, and Z400 were larger than that of the uncoated CAM, with up to $199\ \mathrm{mAh\ g_{CAM}}^{-1}$ for Z400, corresponding to $\approx 2.1\ \mathrm{mAh\ cm^{-2}}$. The reason is the higher Coulomb efficiency of cells using these materials (81.2% for uncoated NCM85, compared to 86.6% for Z250 and >90% for Z300 and Z400) or, in other words, the lower tendency for SE degradation (oxidation), a well-documented problem of thiophosphate-based SSBs.[6–9,50] The increase in Coulomb efficiency with annealing at $250\ °C < \vartheta \leq 400\ °C$ suggests more effective surface passivation, probably because of densification of the coating, and points at a high degree of coverage of the NCM85 surface.[7,8] While low electronic conductivity is a desirable property of coatings for mitigating interfacial degradation, loss of electronic contact between CAM particles must be avoided.[7] Interestingly, the electronic conductivity in the composite cathode was not affected much compared with the uncoated NCM85, despite the relatively dense nature of the ALD-derived ZrO_2 nanocoating. The voltage profiles further revealed that the "additional" discharge capacity for Z250, Z300, and Z400 can be attributed to improved lithiation at low voltages. This is also apparent from the peak at ≈1.95 V in the corresponding differential capacity curves (see Figure S9, Supporting Information). The presence of this peak depends upon the C-rate; hence, it is clearly associated with the kinetics of the re-intercalation reaction. Cells using Z550 and Z700 delivered considerably lower specific capacities due to high overpotentials, as well as irreversibilities similar to the uncoated NCM85.

The cycling performance of the ZrO_2@NCM85 CAMs was tested at rates ranging from 0.1C to 1C, corresponding to current densities of ≈0.2 and $\approx 2\ \mathrm{mA\ cm^{-2}}$, respectively. The general

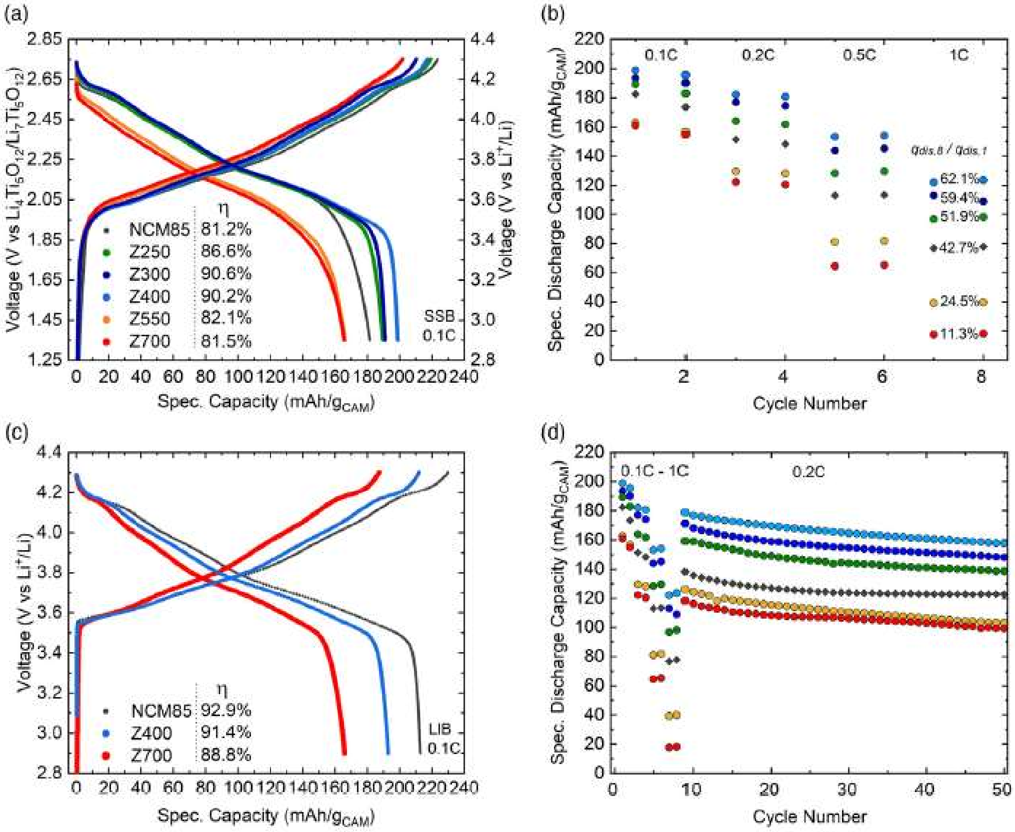

Figure 7. Electrochemical performance of the uncoated NCM85 and ZrO$_2$@NCM85 CAMs in solid-state battery (SSB) cells at 45 °C in the voltage range 1.35–2.75 versus Li$_4$Ti$_5$O$_{12}$/Li$_7$Ti$_5$O$_{12}$ (≈2.9–4.3 V vs Li$^+$/Li). a) First-cycle voltage profiles at 0.1C and corresponding Coulomb efficiencies. b) Specific discharge capacities during rate testing and capacity ratios for the 8th cycle@1C/1st cycle@0.1C. c) First-cycle voltage profiles for the uncoated NCM85, Z400, and Z700 in LIB cells at 0.1C and 45 °C in the voltage range 2.9–4.3 V versus Li$^+$/Li and corresponding Coulomb efficiencies. d) Specific discharge capacities during rate testing (see (b)) and subsequent cycling at 0.2C.

trends (Figure 7b) were similar to that observed in the initial cycle. While the charge-storage properties improved with coating and post-annealing at moderate temperatures, they were adversely affected for both Z550 and Z700. The differences in cell capacity increased with increasing current density. At 1C, Z400 performed best in absolute and relative terms, with a specific discharge capacity of 124 mAh g_{CAM}^{-1} (≈62% of the initial capacity at 0.1C), compared to 78 mAh g_{CAM}^{-1} (≈43%) for uncoated NCM85 and only 18 mAh g_{CAM}^{-1} (≈11%) for Z700. The differences in rate capability can be explained in part by the level of side reactions. This holds for the improvements observed for Z300 and Z400 over Z250. Oxidative SE degradation has been shown to increase the cathode resistance, which is directly reflected in the capacity, especially at high rates.[7,50] However, the poor performance of both Z550 and Z700 cannot be explained by unwanted side reactions only. Likewise, their behavior cannot be explained by the presence of abundant unprotected CAM, as argued in previous studies.[26] The latter would not be expected to result in a worse performance than for the uncoated NCM85. Furthermore, Zr^{4+} doping, which occurs above a certain threshold temperature, has been reported to be beneficial to the cyclability of layered metal oxides and other CAMs.[45,51] Instead, the performance decay appears to be due to impeded ion transport. These considerations led to the STEM-EELS investigations described above, revealing the formation of a rocksalt-like NiO layer and helping to explain the resistive nature of the modified CAM surface. The CAM-inherent performance limitations are corroborated by their cyclability in liquid electrolyte-based LIB cells (Figure 7c). Z700 was found to deliver a similarly low first-cycle specific capacity under identical conditions. Notably, the phase transitions occurred at the same voltages for the uncoated NCM85, Z400, and Z700. This result thus suggests that redox inactivity rather than overpotential (as in the case of SSB cells) plays a role in the differences seen in capacity among the samples. Apart from that, a comparison of the Coulomb efficiencies confirmed that SSB cells using the uncoated NCM85 suffer strongly from (electro)chemical side reactions at the SE|CAM interface in the initial cycle.

After rate performance testing, the SSB cells were subjected to cycling at 0.2C. As can be seen from the data in Figure 7d, only Z250, Z300, and Z400 were capable of delivering larger specific capacities than the uncoated CAM (by 16–35 mAh g_{CAM}^{-1} in the 50th cycle), which stabilized at 124 mAh g_{CAM}^{-1} after 30 cycles. They also showed a more gradual fading with cycling. Taken together, the results demonstrate that good cycling performance is achievable by proper post-treatment, without adding an additional lithium source during coating or the presence of abundant $Li_xZr_yO_z$.

The long-term cycling performance of SSB cells using a selected ZrO_2@NCM85 CAM (10 ALD cycle sample, 350 °C post-annealing) was studied at a rate of 0.5C in some more detail. This sample was chosen based on initial results from electrochemical testing. Nevertheless, its cyclability is very similar to that of Z300/Z400. As expected from the aforementioned data, the coated material delivered a larger initial specific discharge capacity (172 vs 164 mAh g_{CAM}^{-1}) and showed better capacity retention (≈78% vs ≈68% of the initial capacity after 200 cycles) than the uncoated NCM85 (**Figure** 8a). Similar to the cycling at 0.2C, the fading was more gradual compared to that of the uncoated CAM, where the majority of the capacity degradation occurred over the first 25 cycles, due to increasing overpotential resulting from side reactions at the SE|CAM interface. The latter is corroborated by the data shown in Figure 8b. The Coulomb efficiency of cells with the ZrO_2@NCM85 CAM was much higher during the first few cycles (e.g., 85.2% vs 75.5% in the initial cycle). The different extent of SE oxidation was also evident from electrochemical impedance spectroscopy (EIS) analysis. Semi-quantitative comparison of Nyquist plots of the electrochemical impedance for the respective cells after 200 cycles (Figure 8c) revealed a difference in cathode interfacial resistance by a factor of about two (EIS data collected prior to cycling are shown in Figure S10, Supporting Information).

Time-of-flight secondary-ion mass spectrometry (ToF-SIMS) was applied to link the electrochemical data with the interfacial degradation. Investigations on electrodes prior to and after cycling (200 cycles at 0.5C and 45 °C) provided direct evidence of a larger amount of oxygen-containing phosphorus and sulfur species in cycled SSB cathodes containing the uncoated NCM85. The measured intensities for the PO_3^- and SO_4^- fragments are shown in **Figure** 9a,b (see Figure S11, Supporting Information for other species). Such species are formed exclusively at the SE|CAM interface, since the NCM85 represents the only oxygen source in the system. While mitigating interfacial degradation, complete suppression could not be achieved by ALD coating of the CAM secondary particles. This result agrees well with the large number of available literature reports on (oxide) coatings, from which no conclusion can be drawn as to what composition/morphology is most effective in suppressing side reactions.[6,7,12] Interestingly, there were no significant differences in the amount of polysulfide species, which can probably be explained by the fact that they are also formed at the interfaces of the SE with the current collector and carbon black.

In addition to the chemical degradation, the mechanical integrity of the CAMs was studied by cross-sectional SEM of FIB-prepared SSB cathodes prior to (see Figure S12, Supporting Information) and after cycling (see Figure 9c,d and Figure S13, Supporting Information). After 200 cycles, both the coated and uncoated samples showed signs of particle fracture typical of polycrystalline Ni-rich NCM due to anisotropic volume variations upon (de)lithiation. The cracking occurred primarily at the grain boundaries of the primary particles. Visual/qualitative comparison indicated similar or slightly lower mechanical degradation for the ZrO_2@NCM85, thereby suggesting that the coating helps indirectly to provide some degree of stabilization. Note that Han et al. showed that particle fracture in SSB cells is also determined by the (electro)chemical side reactions occurring at the SE|CAM interface.[52] For more detailed insights into the mechanical behavior, other techniques, such as tomography and/or specific electrochemical methods, would be required. In general, it is difficult to suppress the cracking of polycrystalline NCM CAMs,[7] which explains the increasing interest in their single-crystalline counterparts.[53–56]

Although the evolution of the SE|CAM interface is known to have a considerable effect on battery performance, it is challenging to visualize, requiring inert and cryo conditions during

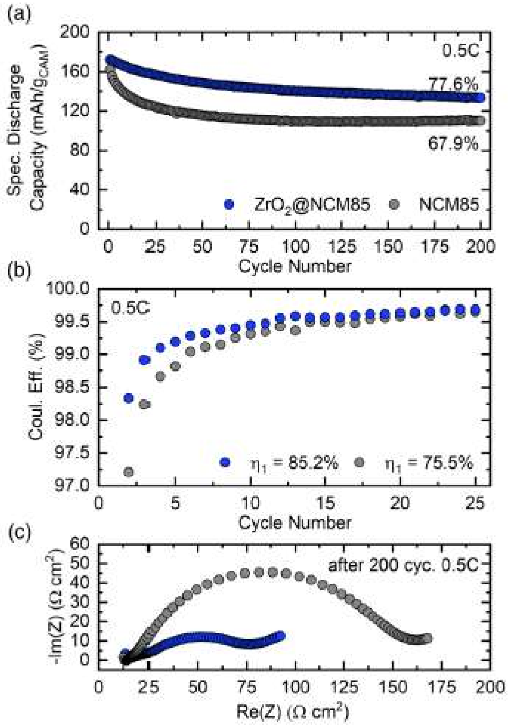

Figure 8. Long-term cycling performance of the uncoated NCM85 and a selected ZrO_2@NCM85 CAM (10 ALD cycle sample, 350 °C post-annealing) in SSB cells at 0.5C and 45 °C in the voltage range 1.35–2.75 versus $Li_4Ti_5O_{12}/Li_7Ti_5O_{12}$ (≈2.9–4.3 V vs Li^+/Li). a) Specific discharge capacities over 200 cycles. b) Coulomb efficiencies for cycles 2–25. The first-cycle values are denoted in the figure. c) Nyquist plots of the electrochemical impedance of representative cells after 200 cycles.

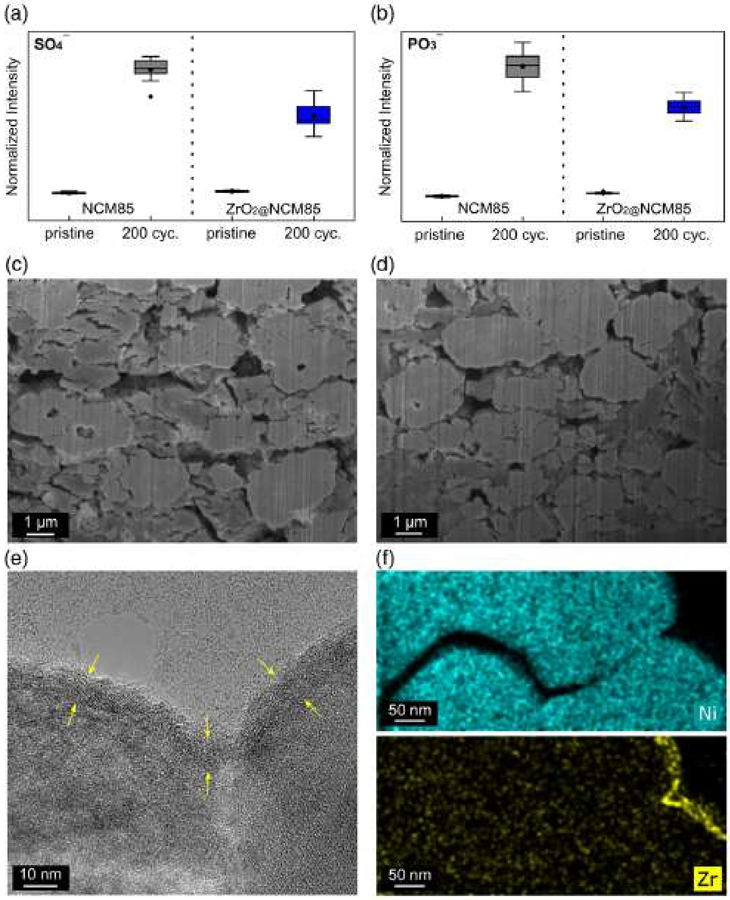

Figure 9. Chemical and morphological analysis of the SSB cathodes after 200 cycles at 0.5C and 45 °C. a,b) Box plots of measured intensities for PO_3^- and SO_4^- fragments from time-of-flight secondary-ion mass spectrometry (ToF-SIMS). c,d) Cross-sectional SEM images of electrodes containing: c) the uncoated NCM85 and d) ZrO_2@NCM85 (10 ALD cycle sample, 350 °C post-annealing). e) HRTEM image with arrows indicating the intact coating. f) Elemental maps of Ni and Zr collected from a FIB-prepared cross-section of a ZrO_2@NCM85 particle.

preparation and imaging. Apart from that, in situ/operando investigations would be desirable to rule out relaxation effects.[57] However, mechanical degradation probably played a minor role in the capacity decay considering the relatively low state-of-charge achieved under the cycling conditions used here. The coating (morphology, crystallinity, and conformity) was preserved well after cycling, as is evident from the HRTEM image and elemental maps in Figure 9e,f. This is notable because coating segregation, aggregation, and "breakdown" (e.g., for $Li_2S–P_2S_5$|Li_2ZrO_3@$LiNi_{0.5}Co_{0.2}Mn_{0.3}O_2$)[21] as well as exfoliation (e.g., for Li_3PS_4|$LiNbO_3$@$LiNi_{1/3}Co_{1/3}Mn_{1/3}O_2$)[48] have been identified as degradation modes in the past. Stable contact between CAM and coating is crucial for maintaining good battery performance, given that separation would create a physical barrier for charge transport and could lead to local oxygen release, as shown recently.[48] Furthermore, delithiation of Li_2ZrO_3 at voltages ≥4.3 V versus Li^+/Li has been demonstrated,[21] making more inert binary oxide coatings, such as ZrO_2, advantageous over Li-containing (ternary) ones.

3. Conclusion

ZrO_2-modified NCM85 CAMs were characterized for use in bulk-type SSB cells. Conformal secondary particle coatings were grown by ALD. Such prototype (protective) nanocoatings allow investigating how their properties affect the cycling performance without the confounding influence of other factors, such as ill-defined morphology or nonuniform coverage. Investigations into the effect of post-heat treatment revealed: 1) nanocrystal growth below 550 °C; 2) partial transformation from tetragonal to monoclinic ZrO_2 at 550 °C and amorphization at higher temperatures;

3) ion diffusion into subsurface regions of the NCM85 at 700 °C; as well as 4) formation of a rocksalt-like NiO layer (along with a distorted interlayer) above 550 °C, due to unfavorable interactions between coating and CAM. The modified NCM85 after "mild" annealing exhibited a promising cycling performance. High specific discharge capacities of 199 and 124 mAh g_{CAM}^{-1} at ≈0.2 and ≈2 mA cm^{-2}, respectively, and a good cycling stability with 77.6% capacity retention after 200 cycles at ≈1 mA cm^{-2} were achieved. Unlike reported previously, the improvement in cyclability did not result from the formation of a ternary oxide coating, but instead from more effective surface passivation. Post-mortem analysis revealed that the extent of SE oxidation is lower for the modified NCM85, while there were only minor differences in mechanical integrity between the coated and uncoated CAM particles. The coating morphology and crystallinity were found to be retained after cycling.

Overall, this study provides insights into the processes occurring during the preparation/post-modification of Zr-based electrode coatings and their effect on the battery performance. It highlights the overlapping phenomena that need to be considered when applying a secondary particle coating for stabilizing cathode interfaces in thiophosphate-based SSB cells. To the best of our knowledge, there is still no protective coating available that allows operation with high Coulomb efficiency beyond 99.9%, low overpotential, and low capacity fading, all of which is needed to compete with the cathode performance in state-of-the-art LIBs.

4. Experimental Section

Cathode Coating and Post-Treatment: Prior to the coating process, $LiNi_{0.85}Co_{0.10}Mn_{0.05}O_2$ (NCM85, $d_{50} \approx 3.5\,\mu m$, $d_{90} \approx 5.0\,\mu m$; BASF SE) CAM was heated for 3 h in O_2 flow at 750 °C (heating and cooling rates set to 5 °C min^{-1}). For the ZrO_2 deposition, 2–8 g NCM85 CAM was encased in a gas-permeable powder holder and introduced into the ALD reactor (Picosun), followed by flushing with N_2 and stabilization at 250 °C for 1 h. The coating process comprised 2–15 ALD cycles, with the same pulse sequence for O_3 (ozone generator from IN USA Inc.) and $Zr[N(CH_2CH_3)(CH_3)]_4$ (TEMAZ, 99.99%; Sigma-Aldrich) and the precursor container heated at 105 °C. A typical sequence consisted of 100 pulses of 0.1 s duration, each followed by 2 s reactor purging and 60 s purging after the last pulse. The N_2 carrier-gas flow in the TEMAZ and ozone lines was set to 200 sccm. Finally, the ZrO_2@NCM85 CAM was heated in O_2 flow at temperatures ranging from 300 to 700 °C for 30 min (heating and cooling rates set to 10 °C min^{-1}).

Elemental Analysis: For compositional analysis, the ZrO_2@NCM85 CAM was dissolved in acid using a pressurized and heated digestion system. The Zr content was determined by ICP-OES using a Thermo Fisher Scientific iCAP 7600 DUO. The carbon content was probed using a CS analyzer.

XRD: XRD data were collected in Debye–Scherrer geometry using an STOE Stadi-P diffractometer with a DECTRIS MYTHEN 1K strip detector and a Mo anode ($\lambda = 0.70926$ Å). The instrumental contribution to the peak broadening was determined by measuring a NIST 660c LaB_6 standard as a line broadening reference. Rietveld refinement analysis was performed using the software FullProf. NCM structural models were refined against the data, where the scale factor, zero shift, and peak shape parameters U and Y were allowed to vary. In the structural model, the unit-cell parameters, oxygen z-coordinate, isotropic temperature factors (B_{iso}) of the oxygen and transition-metal atoms (with fixed $B_{iso,Li} = 1.0$ Å^2), and occupancy of the Li site were refined. All sites were constrained to be fully occupied and atoms occupying the same site were constrained to have the same atomic parameters. The confidence intervals were determined by multiplying error outputs from the program by a factor of three.

XPS: XPS measurements were carried out on a PHI VersaProbe II instrument (ULVAC-PHI, Inc.) using monochromatic Al-Kα radiation ($E = 1486.6$ eV). The power of the X-ray source was set to 100 W. The powder samples were pressed into a Teflon cup holder, which was mounted on a sample holder using insulating double-sided tape (inert sample transfer). The examined area had a size of 1.3 mm × 0.1 mm. For survey and detailed spectra, pass energies of 117.4 and 23.5 eV, respectively, were used. For charge neutralization, the PHI dual-beam charge neutralization was employed, consisting of a 20 nA and 10 V Ar-ion beam in combination with a 20 μA and 3 V electron beam and effectively pinning the sample potential at −3 V versus ground potential. Data evaluation was done with the software CasaXPS (version 2.3.25; Casa Software Ltd.). The spectra were calibrated in relation to the signal of adventitious carbon at 284.8 eV. A Shirley background was used and the spectra were fitted assuming GL(30) line shape.

SEM: SEM analysis was carried out using an LEO-1530 electron microscope (Carl Zeiss AG) with a field emission source at an accelerating voltage of 10 kV. Cross-sections of pristine cathodes were prepared by ion milling using an IB-19510CP cross-section polisher (JEOL). Cross-sections of cycled cathodes were prepared and examined using a Strata 400S (FEI Company).

TEM: TEM specimens were prepared by the lift-out technique using a Strata 400S focused Ga-ion beam. The area of interest was coated with a carbon film to protect the samples from beam damage. The samples were milled and thinned at 30 kV and polished at 5 and 2 kV to clean the surface. The prepared lamellae were attached to Mo or Cu half grids for the TEM characterization. A probe-corrected Themis 300 TEM and a double aberration-corrected Themis Z TEM (Thermo Fisher Scientific) were used to image the specimens, both at an accelerating voltage of 300 kV. HAADF-STEM images were collected using a HAADF detector with a collection semi-angle range from 60 to 200 mrad. The EDS mapping was done using an EDAX SuperX EDS detector. EELS data were acquired by a Gatan image filter with a K3 camera (Gatan Inc.) using a camera length of 29.5 mm, a screen current of 20 pA, and an energy dispersion of 0.18 eV/channel. The energy resolution estimated from the FWHM of the zero-loss peak is ≈1.7 eV. The NBED patterns were acquired in micro-STEM mode with a convergence semi-angle of 0.2 mrad and a camera length of 380 mm.

ToF-SIMS: ToF-SIMS measurements were performed on a TOF-SIMS 5–100 system (IONTOF GmbH). The samples were prepared and transferred to the device under an inert atmosphere. All measurements were performed in negative ion mode using Bi_3^+ (25 keV) as primary ions. The surface of the samples was flooded with low-energy electrons for charge compensation. The cycle time was set to 60 μs. Surface analysis was performed in spectrometry mode (bunched mode) to enable high signal intensities and high mass resolution. The analysis area was 150 μm × 150 μm and rasterized with 256 pixels × 256 pixels (random mode). Every patch was analyzed with 1 frame and 1 shot per pixel and frame. The measurement was stopped after a primary ion dose of 10^{12} ions cm^{-2} was reached (static condition). The primary ion current was ≈0.5 pA. Data evaluation was carried out using the software SurfaceLab 7.1 from IONTOF GmbH.

Preparation of Electrode Composites: The cathode composites were prepared by mixing the uncoated NCM85 or ZrO_2@NCM85 CAMs with LPSCl SE (NEI Corp.), and Super C65 carbon black (Timcal) in a ratio of 69:30:1 by weight using 10 zirconia balls in a planetary mill (Fritsch) at 140 rpm for 30 min under an Ar atmosphere. Analogously, the anode composites were prepared from carbon-coated LTO (NEI Corp.), LPSCl SE, and Super C65 carbon black at a weight ratio of 30:65:5.

SSB Assembly and Testing: The electrochemical performance of the uncoated NCM85 and ZrO_2@NCM85 CAMs was tested in bulk-type SSB cells as described previously.[39] The separator layer of diameter 10 mm was produced by compacting 100 mg LPSCl SE at a uniaxial pressure of 62 MPa. The pellet stack was completed by adding 65 mg anode composite and 11–12 mg cathode composite (≈2.9 mAh cm^{-2} for $q_{th} = 274$ mAh g_{CAM}^{-1}) on either side and pressing the stack at

437 MPa. The cells were galvanostatically cycled at 45 °C in a voltage range between 1.35 and 2.75 versus $Li_4Ti_5O_{12}/Li_7Ti_5O_{12}$ while maintaining a uniaxial pressure of 81 MPa. Rate performance tests were carried out at 0.1, 0.2, 0.5, and 1C (with 1C = 190 mA g_{CAM}^{-1}), with two charge/discharge cycles at each C-rate, followed by cycling at 0.2C. Stability tests were carried out at 0.5C for 200 cycles.

LIB Assembly and Testing: Cathodes for testing in LIB half-cells were produced by casting an *N*-methyl-2-pyrrolidone (NMP)-based slurry onto Al foil, followed by vacuum-drying at 120 °C and calendering at 15 N mm^{-1}. The cathodes consisted of CAM, Super C65 carbon black, and polyvinylidene fluoride (PVDF) binder in a 94:3:3 weight ratio. Circular electrodes of 12 mm diameter with an areal loading of ≈8 mg_{CAM} cm^{-2} were punched out from the as-prepared tapes and used to assemble 2032 coin cells. The cells comprised a glass fiber separator (GF/D; Whatman), 95 μL electrolyte (1 M $LiPF_6$ in 3:7 by weight ethylene carbonate and ethyl methyl carbonate; BASF SE), and a Li-metal anode (Albemarle Germany GmbH). They were cycled at 0.1C and 45 °C in the same voltage range as the SSB cells.

EIS: EIS was conducted on SSB cells in the discharged state prior to cycling and after 200 cycles at frequencies ranging from 7 MHz to 100 mHz with an amplitude of 10 mV using an SP-300 impedance analyzer (Bio-Logic Science Instruments Ltd.)

Statistical Analysis: Electrochemical cycling data are averaged from at least three independent measurements. Mean values were determined via "Statistics on Rows" using OriginPro 2018b (OriginLab Corp.). Zr mass fraction data for 5 and 10 ALD cycles are the average from two or more independent experiments on different batches of NCM85 (using the same synthesis parameters). Both mean values and standard deviations were determined via "Statistics on Rows" using OriginPro 2018b (OriginLab Corp.). Mass fractions from ICP-OES analysis represent the average of three independent measurements on samples from the same batch. For ToF-SIMS, 13 mass spectra were collected in different areas on the sample surface to ensure the reproducibility of results.

Supporting Information

Supporting Information is available from the Wiley Online Library or from the author.

Acknowledgements

This study was supported by BASF SE. The authors acknowledge the support from the Karlsruhe Nano Micro Facility (KNMFi, www.knmf.kit.edu), a Helmholtz research infrastructure at Karlsruhe Institute of Technology (KIT, www.kit.edu). D.K. acknowledges the Fonds der Chemischen Industrie (FCI) for financial support through a Kekulé fellowship. Y.T. acknowledges the financial support from the German Research Foundation (DFG) under project ID 390874152 (POLiS Cluster of Excellence). The authors thank Dr. Thomas Bergfeldt and colleagues (IAM-AWP, KIT) for compositional analysis, Ruizhuo Zhang (BELLA-INT, KIT) for collecting supplementary SEM data, and Prof. Christian Kübel (INT, KIT) for fruitful discussions.

Conflict of Interest

The authors declare no conflict of interest.

Data Availability Statement

The data that support the findings of this study are available from the corresponding author upon reasonable request.

Keywords

atomic layer deposition, cathode materials, electro-chemo-mechanical degradation, solid-state batteries, surface characterization

Received: September 21, 2022
Revised: October 24, 2022

---

[1] J. Janek, W. G. Zeier, *Nat. Energy* **2016**, *1*, 16141.
[2] Y.-K. Sun, *ACS Energy Lett.* **2020**, *5*, 3221.
[3] T. Famprikis, P. Canepa, J. A. Dawson, M. S. Islam, C. Masquelier, *Nat. Mater.* **2019**, *18*, 1278.
[4] Y. Kato, S. Hori, T. Saito, K. Suzuki, M. Hirayama, A. Mitsui, M. Yonemura, H. Iba, R. Kanno, *Nat. Energy* **2016**, *1*, 16030.
[5] D. Andre, S.-J. Kim, P. Lamp, S. F. Lux, F. Maglia, O. Paschos, B. Stiaszny, *J. Mater. Chem. A* **2015**, *3*, 6709.
[6] A. Banerjee, X. Wang, C. Fang, E. A. Wu, Y. S. Meng, *Chem. Rev.* **2020**, *120*, 6878.
[7] S. P. Culver, R. Koerver, W. G. Zeier, J. Janek, *Adv. Energy Mater.* **2019**, *9*, 1900626.
[8] Y. Zhu, X. He, Y. Mo, *ACS Appl. Mater. Interfaces* **2015**, *7*, 23685.
[9] R. Koerver, F. Walther, I. Aygün, J. Sann, C. Dietrich, W. G. Zeier, J. Janek, *J. Mater. Chem. A* **2017**, *5*, 22750.
[10] N. Ohta, K. Takada, I. Sakaguchi, L. Zhang, R. Ma, K. Fukuda, M. Osada, T. Sasaki, *Electrochem. Commun.* **2007**, *9*, 1486.
[11] A.-Y. Kim, F. Strauss, T. Bartsch, J. H. Teo, T. Hatsukade, A. Mazilkin, J. Janek, P. Hartmann, T. Brezesinski, *Chem. Mater.* **2019**, *31*, 9664.
[12] F. Walther, F. Strauss, X. Wu, B. Mogwitz, J. Hertle, J. Sann, M. Rohnke, T. Brezesinski, J. Janek, *Chem. Mater.* **2021**, *33*, 2110.
[13] K. Takada, N. Ohta, L. Zhang, K. Fukuda, I. Sakaguchi, R. Ma, M. Osada, T. Sasaki, *Solid State Ionics* **2008**, *179*, 1333.
[14] H. Kitaura, A. Hayashi, K. Tadanaga, M. Tatsumisago, *Solid State Ionics* **2011**, *192*, 304.
[15] S. H. Jung, K. Oh, Y. J. Nam, D. Y. Oh, P. Brüner, K. Kang, Y. S. Jung, *Chem. Mater.* **2018**, *30*, 8190.
[16] Y.-G. Lee, S. Fujiki, C. Jung, N. Suzuki, N. Yashiro, R. Omoda, D.-S. Ko, T. Shiratsuchi, T. Sugimoto, S. Ryu, J. H. Ku, T. Watanabe, Y. Park, Y. Aihara, D. Im, I. T. Han, *Nat. Energy* **2020**, *5*, 299.
[17] F. Strauss, J. H. Teo, J. Maibach, A.-Y. Kim, A. Mazilkin, J. Janek, T. Brezesinski, *ACS Appl. Mater. Interfaces* **2020**, *12*, 57146.
[18] C. Wang, L. Chen, H. Zhang, Y. Yang, F. Wang, F. Yin, G. Yang, *Electrochim. Acta* **2014**, *119*, 236.
[19] S. Ito, S. Fujiki, T. Yamada, Y. Aihara, Y. Park, T. Y. Kim, S.-W. Baek, J.-M. Lee, S. Doo, N. Machida, *J. Power Sources* **2014**, *248*, 943.
[20] F. Zhao, Y. Zhao, J. Wang, Q. Sun, K. Adair, S. Zhang, J. Luo, J. Li, W. Li, Y. Sun, X. Li, J. Liang, C. Wang, R. Li, H. Huang, L. Zhang, S. Zhao, S. Lu, X. Sun, *Energy Storage Mater.* **2020**, *33*, 139.
[21] Y.-Q. Zhang, Y. Tian, Y. Xiao, L. J. Miara, Y. Aihara, T. Tsujimura, T. Shi, M. C. Scott, G. Ceder, *Adv. Energy Mater.* **2020**, *10*, 1903778.
[22] M. Leskelä, M. Ritala, *Angew. Chem., Int. Ed.* **2003**, *42*, 5548.
[23] R. W. Johnson, A. Hultqvist, S. F. Bent, *Mater. Today* **2014**, *17*, 236.
[24] D. Weber, Đ. Tripković, K. Kretschmer, M. Bianchini, T. Brezesinski, *Eur. J. Inorg. Chem.* **2020**, *2020*, 3117.
[25] S. Neudeck, A. Mazilkin, C. Reitz, P. Hartmann, J. Janek, T. Brezesinski, *Sci. Rep.* **2019**, *9*, 5328.
[26] W. Bao, G. Qian, L. Zhao, Y. Yu, L. Su, X. Cai, H. Zhao, Y. Zuo, Y. Zhang, H. Li, Z. Peng, L. Li, J. Xie, *Nano Lett.* **2020**, *20*, 8832.
[27] J. Xie, A. D. Sendek, E. D. Cubuk, X. Zhang, Z. Lu, Y. Gong, T. Wu, F. Shi, W. Liu, E. J. Reed, Y. Cui, *ACS Nano* **2017**, *11*, 7019.

[28] D. Mohanty, K. Dahlberg, D. M. King, L. A. David, A. S. Sefat, D. L. Wood, C. Daniel, S. Dhar, V. Mahajan, M. Lee, F. Albano, *Sci. Rep.* **2016**, *6*, 26532.

[29] Y. Zhao, K. Zheng, X. Sun, *Joule* **2018**, *2*, 2583.

[30] B. Wang, Y. Zhao, M. N. Banis, Q. Sun, K. R. Adair, R. Li, T.-K. Sham, X. Sun, *ACS Appl. Mater. Interfaces* **2018**, *10*, 1654.

[31] J. Liu, M. N. Banis, X. Li, A. Lushington, M. Cai, R. Li, T.-K. Sham, X. Sun, *J. Phys. Chem. C* **2013**, *117*, 20260.

[32] A. C. Kozen, A. J. Pearse, C.-F. Lin, M. Noked, G. W. Rubloff, *Chem. Mater.* **2015**, *27*, 5324.

[33] J. H. Woo, J. E. Trevey, A. S. Cavanagh, Y. S. Choi, S. C. Kim, S. M. George, K. H. Oh, S.-H. Lee, *J. Electrochem. Soc.* **2012**, *159*, A1120.

[34] D. Kitsche, Y. Tang, Y. Ma, D. Goonetilleke, J. Sann, F. Walther, M. Bianchini, J. Janek, T. Brezesinski, *ACS Appl. Energy Mater.* **2021**, *4*, 7338.

[35] X. Li, Z. Ren, M. N. Banis, S. Deng, Y. Zhao, Q. Sun, C. Wang, X. Yang, W. Li, J. Liang, X. Li, Y. Sun, K. Adair, R. Li, Y. Hu, T.-K. Sham, H. Huang, L. Zhang, S. Lu, J. Luo, X. Sun, *ACS Energy Lett.* **2019**, *4*, 2480.

[36] J. W. Lee, Y. J. Park, *J. Electrochem. Sci. Technol.* **2018**, *9*, 176.

[37] R. S. Negi, E. Celik, R. Pan, R. Stäglich, J. Senker, M. T. Elm, *ACS Appl. Energy Mater.* **2021**, *4*, 3369.

[38] M. Putkonen, T. Aaltonen, M. Alnes, T. Sajavaara, O. Nilsen, H. Fjellvåg, *J. Mater. Chem.* **2009**, *19*, 8767.

[39] D. Kitsche, F. Strauss, Y. Tang, N. Bartnick, A.-Y. Kim, Y. Ma, C. Kübel, J. Janek, T. Brezesinski, *Batteries Supercaps* **2022**, *5*, e202100397.

[40] T. Hatsukade, A. Schiele, P. Hartmann, T. Brezesinski, J. Janek, *ACS Appl. Mater. Interfaces* **2018**, *10*, 38892.

[41] D. M. Hausmann, E. Kim, J. Becker, R. G. Gordon, *Chem. Mater.* **2002**, *14*, 4350.

[42] Y. Ma, J. H. Teo, F. Walther, Y. Ma, R. Zhang, A. Mazilkin, Y. Tang, D. Goonetilleke, J. Janek, M. Bianchini, T. Brezesinski, *Adv. Funct. Mater.* **2022**, *32*, 2111829.

[43] G. Skandan, H. Hahn, M. Roddy, W. R. Cannon, *J. Am. Ceram. Soc.* **1994**, *77*, 1706.

[44] G. Baldinozzi, D. Simeone, D. Gosset, M. Dutheil, *Phys. Rev. Lett.* **2003**, *90*, 216103.

[45] F. Schipper, H. Bouzaglo, M. Dixit, E. M. Erickson, T. Weigel, M. Talianker, J. Grinblat, L. Burstein, M. Schmidt, J. Lampert, C. Erk, B. Markovsky, D. T. Major, D. Aurbach, *Adv. Energy Mater.* **2018**, *8*, 1701682.

[46] P. Mukherjee, P. Lu, N. Faenza, N. Pereira, G. Amatucci, G. Ceder, F. Cosandey, *ACS Appl. Mater. Interfaces* **2021**, *13*, 17478.

[47] F. Lin, I. M. Markus, D. Nordlund, T.-C. Weng, M. D. Asta, H. L. Xin, M. M. Doeff, *Nat. Commun.* **2014**, *5*, 3529.

[48] S. Kobayashi, H. Watanabe, T. Kato, F. Mizuno, A. Kuwabara, *ACS Appl. Mater. Interfaces* **2022**, *14*, 39459.

[49] G. H. Aydogdu, D. Ruzmetov, S. Ramanathan, *J. Appl. Phys.* **2010**, *108*, 113702.

[50] J. Auvergniot, A. Cassel, J.-B. Ledeuil, V. Viallet, V. Seznec, R. Dedryvère, *Chem. Mater.* **2017**, *29*, 3883.

[51] C. S. Yoon, U.-H. Kim, G.-T. Park, S. J. Kim, K.-H. Kim, J. Kim, Y.-K. Sun, *ACS Energy Lett.* **2018**, *3*, 1634.

[52] Y. Han, S. H. Jung, H. Kwak, S. Jun, H. H. Kwak, J. H. Lee, S.-T. Hong, Y. S. Jung, *Adv. Energy Mater.* **2021**, *11*, 2100126.

[53] S. Payandeh, D. Goonetilleke, M. Bianchini, J. Janek, T. Brezesinski, *Curr. Opin. Electrochem.* **2022**, *31*, 100877.

[54] P. Minnmann, F. Strauss, A. Bielefeld, R. Ruess, P. Adelhelm, S. Burkhardt, S. L. Dreyer, E. Trevisanello, H. Ehrenberg, T. Brezesinski, F. H. Richter, J. Janek, *Adv. Energy Mater.* **2022**, *12*, 2201425.

[55] C. Doerrer, I. Capone, S. Narayanan, J. Liu, C. R. M. Grovenor, M. Pasta, P. S. Grant, *ACS Appl. Mater. Interfaces* **2021**, *13*, 37809.

[56] X. Liu, B. Zheng, J. Zhao, W. Zhao, Z. Liang, Y. Su, C. Xie, K. Zhou, Y. Xiang, J. Zhu, H. Wang, G. Zhong, Z. Gong, J. Huang, Y. Yang, *Adv. Energy Mater.* **2021**, *11*, 2003583.

[57] F. Strauss, D. Kitsche, Y. Ma, J. H. Teo, D. Goonetilleke, J. Janek, M. Bianchini, T. Brezesinski, *Adv. Energy Sustainability Res.* **2021**, *2*, 2100004.

4 Conclusions and Outlook

The combination of thiophosphates and Ni-rich NCM materials has the potential to enable safe batteries with high energy and power density. However, the realization of this potential requires solving a number of challenges, including engineering stable interfaces. Based on a wide body of literature that was briefly summarized here, it is evident that relevant cathodes with oxide CAM and thiophosphate SE suffer from various instability issues and thus need a protective layer to mitigate degradation. As further explained, such layers can have a range of functionalities. Moreover, common methods to fabricate CAM coatings were summarized and new trends and approaches in the literature were surveyed.

The main focus of this doctoral thesis was to prepare, optimize, characterize and test protective coatings to improve the interfacial compatibility of a Ni-rich NCM CAM with the thiophosphate Li_6PS_5Cl, aiming at enhancing the performance of SSB cells using these materials. The atomic layer deposition technique was expected to be ideally suited to deposit highly uniform, conformal and nanometer-thin layers on CAMs, but barely any studies had reported on its application for this purpose in the SSB field at the beginning of this project.

Therefore, ALD was adopted to prepare HfO_2 and ZrO_2 coatings on NCM851005 via the TEMAH/O_3 and TEMAZ/O_3 processes. Initial work, reported in Publication I, could establish appropriate deposition conditions, pulsing sequences, the preferable selection of ozone as oxidant etc. TEM revealed that these coatings are uniform and consist of nanoparticles (e.g., ~3 nm-sized monoclinic HfO_2 crystals). Furthermore, testing of the modified CAMs in SSB cells revealed that a post-heat treatment had the biggest impact on performance. For example, reversible specific capacities of ~200 mAh/g_{CAM} (more than 20 mAh/g_{CAM} higher than the bare NCM85) and an 80% improvement in rate performance compared to the uncoated CAM could be achieved. This was suggested to result from Li^+ incorporation into the hafnia by reaction with residual Li present on the NCM surface, based on the shift of Hf4f binding energies observed by XPS.

Publication III aimed at gaining more detailed insights into the post-annealing step by systematically investigating a series of ZrO_2@NCM85 samples heated at 300-700 °C. This revealed a multifaceted evolution of the (sub)surface layer, comprising many phenomena: The zirconia nanocrystals were observed to grow (250-550 °C), partially change their structure (550 °C) and undergo partial amorphization (700 °C). Moreover, annealing at 700 °C leads to Zr^{4+} ion diffusion into the NCM subsurface region. Apart from that, adverse reactions between the NCM and ZrO_2 result in the formation of a rocksalt-like layer and a distorted interlayer. Similar to the case of HfO_2@NCM, the performance reaches an optimum when the coated CAM is heated at ~400 °C. Again, this is probably due to more effective surface passivation resulting from the densified surface layer. Interestingly, differing from the HfO_2 case, there was no sign of Li^+ incorporation into the ZrO_2 at that temperature yet. The sharp decline in cycling performance over 500 °C, due to high overpotential, indicates a highly resistive nature of the rocksalt-like interlayer. The strong changes in surface morphology, crystallinity and composition as well as the high variation of the cell performance show that coating preparation parameters need to be carefully optimized and controlled. It could be shown that ALD is well-suited for this aim.

Overall, Publications I and III have shown that ALD is a suitable technique to produce high-quality (model) coatings that allow for better investigation of the relationship between the properties of the modified CAM surface and the cycling behavior (with no or little confounding influences by coating imperfections). Despite the common expectation that binary oxides are inappropriate for the use in SSB coatings, due to their low ionic conductivity, rather well-performing cells could be obtained based on the here presented surface modifications. A likely reason for this is the low thickness of the coatings, which limits the charge-transfer resistance they add. Apart from that, the concern that continuous layers of such electronically insulating materials would interrupt electronic percolation within the cathode did not materialize here. This leads to the question whether the coatings are still fully covering the CAM after cell assembly and during cycling. The evidence gathered suggests that the coatings are continuous and remain in contact during cell operation. However, these statements are based on TEM and, thus, small investigated sample regions, so further investigations are required to evaluate whether they apply in general. ALD of Li-containing oxide coatings has been applied in recent years and there are certainly reasons to expect that they are superior to their binary counterparts. Nevertheless, systematic comparisons between optimized representatives of both classes of coatings in combination with state-of-the-art CAMs and SEs would be of high value. Such a comparison would help deciding whether the use of difficile ALD processes with lithium compounds is warranted, or if indirect approaches via the post-annealing of binary oxides suffice to generate adequate Li-transfer capabilities of such protective layers. The latter option could be advanced by identifying the amounts of residual Li on the NCM surface that are ideal for a Li^+ incorporation into the coating. They could then be targeted by adjusting the excess of the precursor in the CAM synthesis accordingly.

In Publication II, a promising sol-gel-derived coating was presented. The targeted phase $Li_6ZnNb_4O_{14}$ was not formed, but a composite coating consisting of Li_3NbO_4 nanocrystals and Li_2CO_3. The coating shows similarities to previously reported $Li_2CO_3/LiNbO_3$ hybrid coatings prepared by wet chemical methods. However, excellent electrochemical performance could be achieved. For example, LZNO@NCM85 delivered reversible specific capacities of 212 and 150 mAh/g_{CAM} (compared to 178 and 57 mAh/g_{CAM} for the bare NCM) at 0.2 and 2.0 mA/g_{CAM}, respectively. Moreover, ~81% of the initial capacity could be retained after 200 cycles. Notably, the coating was also superior to conventional lithium niobate coatings of different compositions. While the role of Zn could not be fully elucidated, testing of Zn-free reference materials showed that it was instrumental in achieving the aforementioned performance. The study points out several questions for future research: i) Are disordered rocksalt (DRX) materials viable CAM coatings for SSBs? The presence of cubic Li_3NbO_4 is of interest, since this material has recently been identified as a host structure for DRX CAMs.[141,142] ii) How do small additions, like the zinc acetate used here, exert such a big influence on the CAM performance? Do they, for example, act as a dopant of the coating/CAM, or do they influence the crystallization behavior of the main coating constituents? Answering this requires characterization with very high resolution and sensitivity, as the TEM experiments in Publication II have shown. iii) Is the sol-gel technique sufficient to produce coatings that reduce interfacial degradation to an acceptable level and enable high-performance thiophosphate|NCM cathodes? Some of the best reported coatings, such as the LZO layer in a very well-performing cell presented recently by Samsung, were fabricated using this technique. Therefore, maybe other techniques to optimize coating quality in terms of uniformity, conformity etc. are not necessarily needed. This in turn means that it would be worthwhile to investigate how such processes can be improved on, for example, by changing the solvent and using other precursors, process temperatures etc.

Overall, it has to be said that, despite all the progress made in the field, still no protective CAM coating has been proposed that enables operation of SSB cells with high reversibility (Coulomb efficiencies higher than 99.9%), low overpotential and low capacity fading. However, all these aspects are mandatory if SSBs are to compete with conventional state-of-the-art LIBs (or their even more developed future versions, which will be available by the time SSB cells are approaching commercialization). Obviously, CAM coatings cannot solve all problems in SSB cathodes. For example, mechanical degradation caused by the anisotropic volume changes of polycrystalline Ni-rich NCMs might lead to interparticle cracking, which in turn results in contact loss and increases tortuosity. There are indications that coatings can reduce such processes, however, most likely only partially.[53] Therefore, several strategies on tailoring the CAM morphology to alleviate these issues. For example, full-concentration gradient or single-crystalline CAMs have been proposed. Furthermore, the use of polymer binders, which are typically employed in LIB electrodes, can contribute to alleviate mechanical instabilities.[60] These routes are likely to be popular topics of future SSB research.

The much-needed future research on CAM coatings should emphasize a more systematic evaluation of the performance afforded by the various coating compounds and methods. Currently, the comparison of data on supposedly similar (sometimes even compositionally identical) coatings obtained across research labs reveals large discrepancies. Therefore, in the short-term, it would be valuable if studies could carefully analyze the properties and performance of similar or (if possible) identical coatings prepared by different deposition methods. This would enable testing under comparable conditions regarding the used SEs and electrode materials, cell assembly procedures, applied stack pressures, cycling protocols etc. Admittedly, this is demanding in terms of time and resources. Hence, it should be at least considered to compare newly proposed coatings to benchmark coatings such as the prototype material lithium niobate. The mere performance improvement compared to an uncoated reference might be a first hurdle to take but can be achieved by a wide range of materials and does usually not require high-quality surface layers. Apart from that, the experimental parameters of the coating synthesis and the testing conditions should be reported in more detail. In the long-term, increasingly standardized test setups and conditions (that are application-relevant) would be of value.

In conclusion, the quest for viable cathode active material coatings will continue since any successful future (thiophosphate-based) SSB cell will require engineered interfaces.

5 Bibliography

[1] J. B. Goodenough, *Nat. Electron.* **2018**, *1*, 204.

[2] J. B. Goodenough, K. S. Park, *J. Am. Chem. Soc.* **2013**, *135*, 1167.

[3] M. Li, J. Lu, Z. Chen, K. Amine, *Adv. Mater.* **2018**, *30*, 1800561.

[4] M. Winter, B. Barnett, K. Xu, *Chem. Rev.* **2018**, *118*, 11433.

[5] J. Xie, Y. C. Lu, *Nat. Commun.* **2020**, *11*, 2499.

[6] IPCC, *Climate Change 2022, Mitigation of Climate Change Summary for Policymakers (SPM)*, Intergovernmental Panel On Climate Change, **2022**.

[7] Roland-Berger, "E-Mobility Index 2021," https://www.rolandberger.com/publications/publication_pdf/roland_berger_e_mobility_index_2021_en.pdf, **2021**.

[8] The Economist, "The death of the internal combustion engine," https://www.economist.com/leaders/2017/08/12/the-death-of-the-internal-combustion-engine, **2017**.

[9] Neweurope, "The end of the internal combustion engine," https://www.neweurope.eu/article/the-end-of-the-internal-combustion-engine/, **2021**.

[10] European Commission, "Fit for 55: Delivering the EU's 2030 Climate Target on the way to climate neutrality," **2021**.

[11] Chargemap, "Number of charging pools," https://chargemap.com/about/stats, **2022**.

[12] J. Janek, W. G. Zeier, *Nat. Energy* **2016**, *1*, 16141.

[13] M. Bianchini, M. Roca-Ayats, P. Hartmann, T. Brezesinski, J. Janek, *Angew. Chemie - Int. Ed.* **2019**, *58*, 10434.

[14] H. J. Peng, J. Q. Huang, X. B. Cheng, Q. Zhang, *Adv. Energy Mater.* **2017**, *7*, 1700260.

[15] J. Christensen, P. Albertus, R. S. Sanchez-Carrera, T. Lohmann, B. Kozinsky, R. Liedtke, J. Ahmed, A. Kojic, *J. Electrochem. Soc.* **2011**, *159*, R1.

[16] T. Famprikis, P. Canepa, J. A. Dawson, M. S. Islam, C. Masquelier, *Nat. Mater.* **2019**, *18*, 1278.

[17] Y.-K. Sun, *ACS Energy Lett.* **2020**, *5*, 3221.

[18] R. C. Agrawal, G. P. Pandey, *J. Phys. D. Appl. Phys.* **2008**, *41*, 223001.

[19] A. Manthiram, X. Yu, S. Wang, *Nat. Rev. Mater.* **2017**, *2*, 16103.

[20] Y. Nikodimos, W. N. Su, B. J. Hwang, *Adv. Energy Mater.* **2022**, *2202854*, 2202854.

[21] K. J. Kim, M. Balaish, M. Wadaguchi, L. Kong, J. L. M. Rupp, *Adv. Energy Mater.* **2021**, *11*, 2002689.

[22] S. Nanda, A. Gupta, A. Manthiram, *Adv. Energy Mater.* **2021**, *11*, 2000804.

[23] F. Han, A. S. Westover, J. Yue, X. Fan, F. Wang, M. Chi, D. N. Leonard, N. J. Dudney, H. Wang, C. Wang, *Nat. Energy* **2019**, *4*, 187.

[24] T. Krauskopf, F. H. Richter, W. G. Zeier, J. Janek, *Chem. Rev.* **2020**, *120*, 7745.

[25] A. Kato, M. Suyama, C. Hotehama, H. Kowada, A. Sakuda, A. Hayashi, M. Tatsumisago, *J. Electrochem. Soc.* **2018**, *165*, A1950.

[26] Y. Kato, S. Hori, T. Saito, K. Suzuki, M. Hirayama, A. Mitsui, M. Yonemura, H. Iba, R. Kanno, *Nat. Energy* **2016**, *1*, 16030.

[27] P. Minnmann, F. Strauss, A. Bielefeld, R. Ruess, P. Adelhelm, S. Burkhardt, S. L. Dreyer, E. Trevisanello, H. Ehrenberg, T. Brezesinski, F. H. Richter, J. Janek, *Adv. Energy Mater.* **2022**, *12*, 2201425.

[28] P. Minnmann, L. Quillman, S. Burkhardt, F. H. Richter, J. Janek, *J. Electrochem. Soc.* **2021**, *168*, 040537.

[29] A. Bielefeld, D. A. Weber, J. Janek, *ACS Appl. Mater. Interfaces* **2020**, *12*, 12821.

[30] S. P. Culver, R. Koerver, W. G. Zeier, J. Janek, *Adv. Energy Mater.* **2019**, *9*, 1900626.

[31] Y. Wang, W. D. Richards, S. P. Ong, L. J. Miara, J. C. Kim, Y. Mo, G. Ceder, *Nat. Mater.* **2015**, *14*, 1026.

[32] A. Banerjee, X. Wang, C. Fang, E. A. Wu, Y. S. Meng, *Chem. Rev.* **2020**, *120*, 6878.

[33] Y. Zhu, X. He, Y. Mo, *ACS Appl. Mater. Interfaces* **2015**, *7*, 23685.

[34] Y. Zhu, X. He, Y. Mo, *J. Mater. Chem. A* **2016**, *4*, 3253.

[35] B. V. Lotsch, J. Maier, *J. Electroceramics* **2017**, *38*, 128.

[36] Y. Xiao, L. J. Miara, Y. Wang, G. Ceder, *Joule* **2019**, *3*, 1252.

[37] W. D. Richards, L. J. Miara, Y. Wang, J. C. Kim, G. Ceder, *Chem. Mater.* **2016**, *28*, 266.

[38] G. F. Dewald, S. Ohno, M. A. Kraft, R. Koerver, P. Till, N. M. Vargas-Barbosa, J. Janek, W. G. Zeier, *Chem. Mater.* **2019**, *31*, 8328.

[39] F. Strauss, D. Stepien, J. Maibach, L. Pfaffmann, S. Indris, P. Hartmann, T. Brezesinski, *RSC Adv.* **2019**, *10*, 1114.

[40] F. Walther, S. Randau, Y. Schneider, J. Sann, M. Rohnke, F. H. Richter, W. G. Zeier, J. Janek, *Chem. Mater.* **2020**, *32*, 6123.

[41] R. Koerver, F. Walther, I. Aygün, J. Sann, C. Dietrich, W. G. Zeier, J. Janek, *J. Mater. Chem. A* **2017**, *5*, 22750.

[42] F. Walther, R. Koerver, T. Fuchs, S. Ohno, J. Sann, M. Rohnke, W. G. Zeier, J. Janek, *Chem. Mater.* **2019**, *31*, 3745.

[43] J. Auvergniot, A. Cassel, J.-B. Ledeuil, V. Viallet, V. Seznec, R. Dedryvère, *Chem. Mater.* **2017**, *29*, 3883.

[44] J. Auvergniot, A. Cassel, D. Foix, V. Viallet, V. Seznec, R. Dedryvère, *Solid State Ionics* **2017**, *300*, 78.

[45] J. Haruyama, K. Sodeyama, L. Han, K. Takada, Y. Tateyama, *Chem. Mater.* **2014**, *26*, 4248.

[46] N. Ohta, K. Takada, L. Zhang, R. Ma, M. Osada, T. Sasaki, *Adv. Mater.* **2006**, *18*, 2226.

[47] T. Nakamura, K. Amezawa, J. Kulisch, W. G. Zeier, J. Janek, *ACS Appl. Mater. Interfaces* **2019**, *11*, 19968.

[48] S. W. Park, G. Oh, J. W. Park, Y. C. Ha, S. M. Lee, S. Y. Yoon, B. G. Kim, *Small* **2019**, *15*, 1900235.

[49] F. Walther, F. Strauss, X. Wu, B. Mogwitz, J. Hertle, J. Sann, M. Rohnke, T. Brezesinski, J. Janek, *Chem. Mater.* **2021**, *33*, 2110.

[50] F. Strauss, J. H. Teo, J. Maibach, A.-Y. Y. Kim, A. Mazilkin, J. Janek, T. Brezesinski, *ACS Appl. Mater. Interfaces* **2020**, *12*, 57146.

[51] T.-T. Zuo, R. Rueß, R. Pan, F. Walther, M. Rohnke, S. Hori, R. Kanno, D. Schröder, J. Janek, *Nat. Commun.* **2021**, *12*, 6669.

[52] S. K. Jung, H. Gwon, S. S. Lee, H. Kim, J. C. Lee, J. G. Chung, S. Y. Park, Y. Aihara, D. Im, *J. Mater. Chem. A* **2019**, *7*, 22967.

[53] S. H. Jung, U. H. Kim, J. H. Kim, S. Jun, C. S. Yoon, Y. S. Jung, Y. K. Sun, *Adv. Energy Mater.* **2020**, *10*, 1903360.

[54] Y. Ma, R. Zhang, Y. Tang, Y. Ma, J. H. Teo, T. Diemant, D. Goonetilleke, J. Janek, M. Bianchini, A. Kondrakov, T. Brezesinski, *ACS Nano* **2022**, *16*, 18682.

[55] Y. K. Sun, Z. Chen, H. J. Noh, D. J. Lee, H. G. Jung, Y. Ren, S. Wang, C. S. Yoon, S. T. Myung, K. Amine, *Nat. Mater.* **2012**, *11*, 942.

[56] C. S. Yoon, K. J. Park, U. H. Kim, K. H. Kang, H. H. Ryu, Y. K. Sun, *Chem. Mater.* **2017**, *29*, 10436.

[57] T. Bartsch, F. Strauss, T. Hatsukade, A. Schiele, A. Y. Kim, P. Hartmann, J. Janek, T. Brezesinski, *ACS Energy Lett.* **2018**, *3*, 2539.

[58] F. Strauss, J. H. Teo, A. Schiele, T. Bartsch, T. Hatsukade, P. Hartmann, J. Janek, T. Brezesinski, *ACS Appl. Mater. Interfaces* **2020**, *12*, 20462.

[59] J. H. Teo, F. Strauss, Đ. Tripković, S. Schweidler, Y. Ma, M. Bianchini, J. Janek, T. Brezesinski, *Cell Reports Phys. Sci.* **2021**, 100465.

[60] J. H. Teo, F. Strauss, F. Walther, Y. Ma, S. Payandeh, T. Scherer, M. Bianchini, J. Janek, T. Brezesinski, *Mater. Futur.* **2022**, *1*, 015102.

[61] Y. Ma, J. H. Teo, D. Kitsche, T. Diemant, F. Strauss, Y. Ma, D. Goonetilleke, J. Janek, M. Bianchini, T. Brezesinski, *ACS Energy Lett.* **2021**, *6*, 3020.

[62] F. Strauss, D. Kitsche, Y. Ma, J. H. Teo, D. Goonetilleke, J. Janek, M. Bianchini, T. Brezesinski, *Adv. Energy Sustain. Res.* **2021**, *2*, 2100004.

[63] Y. Y. Ma, J. H. Teo, F. Walther, Y. Y. Ma, R. Zhang, A. Mazilkin, Y. Tang, D. Goonetilleke, J. Janek, M. Bianchini, T. Brezesinski, *Adv. Funct. Mater.* **2022**,

32, 2111829.

[64] J. Wandt, A. T. S. Freiberg, A. Ogrodnik, H. A. Gasteiger, *Mater. Today* **2018**, *21*, 825.

[65] A. Sakuda, A. Hayashi, M. Tatsumisago, *Chem. Mater.* **2010**, *22*, 949.

[66] J. M. Doux, Y. Yang, D. H. S. Tan, H. Nguyen, E. A. Wu, X. Wang, A. Banerjee, Y. S. Meng, *J. Mater. Chem. A* **2020**, *8*, 5049.

[67] A. O. Kondrakov, H. Geßwein, K. Galdina, L. De Biasi, V. Meded, E. O. Filatova, G. Schumacher, W. Wenzel, P. Hartmann, T. Brezesinski, J. Janek, *J. Phys. Chem. C* **2017**, *121*, 24381.

[68] L. De Biasi, A. O. Kondrakov, H. Geßwein, T. Brezesinski, P. Hartmann, J. Janek, *J. Phys. Chem. C* **2017**, *121*, 26163.

[69] R. Koerver, I. Aygün, T. Leichtweiß, C. Dietrich, W. Zhang, J. O. Binder, P. Hartmann, W. G. Zeier, J. Janek, *Chem. Mater.* **2017**, *29*, 5574.

[70] S. Jun, Y. J. Nam, H. Kwak, K. T. Kim, D. Y. Oh, Y. S. Jung, *Adv. Funct. Mater.* **2020**, *30*, 2002535.

[71] F. Strauss, L. de Biasi, A.-Y. Kim, J. Hertle, S. Schweidler, J. Janek, P. Hartmann, T. Brezesinski, *ACS Mater. Lett.* **2020**, *2*, 84.

[72] R. Koerver, W. Zhang, L. De Biasi, S. Schweidler, A. O. Kondrakov, S. Kolling, T. Brezesinski, P. Hartmann, W. G. Zeier, J. Janek, *Energy Environ. Sci.* **2018**, *11*, 2142.

[73] S. Schweidler, L. De Biasi, G. Garcia, A. Mazilkin, P. Hartmann, T. Brezesinski, J. Janek, *ACS Appl. Energy Mater.* **2019**, *2*, 7375.

[74] D. Goonetilleke, F. Riewald, A. O. Kondrakov, J. Janek, T. Brezesinski, M. Bianchini, *J. Phys. Chem. C* **2022**, *126,* 16952.

[75] G. Conforto, R. Ruess, D. Schröder, E. Trevisanello, R. Fantin, F. H. Richter, J. Janek, *J. Electrochem. Soc.* **2021**, *168*, 070546.

[76] L. R. Mangani, C. Villevieille, *J. Mater. Chem. A* **2020**, *8*, 10150.

[77] Y. Han, S. H. Jung, H. Kwak, S. Jun, H. H. Kwak, J. H. Lee, S. T. Hong, Y. S. Jung, *Adv. Energy Mater.* **2021**, *11*, 2100126.

[78] S. Kobayashi, H. Watanabe, T. Kato, F. Mizuno, A. Kuwabara, *ACS Appl. Mater. Interfaces* **2022**, *14*, 39459.

[79] J. H. Woo, J. E. Trevey, A. S. Cavanagh, Y. S. Choi, S. C. Kim, S. M. George, K. H. Oh, S.-H. Lee, *J. Electrochem. Soc.* **2012**, *159*, A1120.

[80] W. Zhang, F. H. Richter, S. P. Culver, T. Leichtweiss, J. G. Lozano, C. Dietrich, P. G. Bruce, W. G. Zeier, J. Janek, *ACS Appl. Mater. Interfaces* **2018**, *10*, 22226.

[81] Y. Liu, Q. Sun, J. Liu, M. Norouzi Banis, Y. Zhao, B. Wang, K. Adair, Y. Hu, Q. Xiao, C. Zhang, L. Zhang, S. Lu, H. Huang, X. Song, X. Sun, *ACS Appl. Mater. Interfaces* **2020**, *12*, 2293.

[82] Y. Q. Zhang, Y. Tian, Y. Xiao, L. J. Miara, Y. Aihara, T. Tsujimura, T. Shi, M. C.

Scott, G. Ceder, *Adv. Energy Mater.* **2020**, *10*, 1903778.

[83] J. Cho, Y. J. Kim, T. J. Kim, B. Park, *Angew. Chemie - Int. Ed.* **2001**, *40*, 3367.

[84] S. H. Jung, K. Oh, Y. J. Nam, D. Y. Oh, P. Brüner, K. Kang, Y. S. Jung, *Chem. Mater.* **2018**, *30*, 8190.

[85] C. Wang, X. Li, Y. Zhao, M. N. Banis, J. Liang, X. Li, Y. Sun, K. R. Adair, Q. Sun, Y. Liu, F. Zhao, S. Deng, X. Lin, R. Li, Y. Hu, T. K. Sham, H. Huang, L. Zhang, R. Yang, S. Lu, X. Sun, *Small Methods* **2019**, *3*, 1900261.

[86] C. J. Brinker, G. W. Scherer, *Sol-Gel Science: The Physics and Chemistry of Sol-Gel Processing*, Academic Press, New York, **1990**.

[87] R. W. Johnson, A. Hultqvist, S. F. Bent, *Mater. Today* **2014**, *17*, 236.

[88] H. H. Sønsteby, A. Yanguas-Gil, J. W. Elam, *J. Vac. Sci. Technol. A* **2020**, *38*, 020804.

[89] S. M. George, *Chem. Rev.* **2010**, *110*, 111.

[90] N. E. Richey, C. De Paula, S. F. Bent, *J. Chem. Phys.* **2020**, *152*, 040902.

[91] M. Leskelä, M. Ritala, *Angew. Chemie, Int. Ed.* **2003**, *42*, 5548.

[92] V. Miikkulainen, M. Leskelä, M. Ritala, R. L. Puurunen, *J. Appl. Phys.* **2013**, *113*, 021301.

[93] R. L. Puurunen, *J. Appl. Phys.* **2005**, *97*, 121301.

[94] J. Bachman (ed.), *Atomic Layer Depositions in Energy Conversion Applications*, Wiley-VCH, Weinheim, **2017**.

[95] D. Weber, Đ. Tripković, K. Kretschmer, M. Bianchini, T. Brezesinski, *Eur. J. Inorg. Chem.* **2020**, *2020*, 3117.

[96] S. Neudeck, A. Mazilkin, C. Reitz, P. Hartmann, J. Janek, T. Brezesinski, *Sci. Rep.* **2019**, *9*, 5328.

[97] J. S. Park, A. U. Mane, J. W. Elam, J. R. Croy, *Chem. Mater.* **2015**, *27*, 1917.

[98] D. Mohanty, K. Dahlberg, D. M. King, L. A. David, A. S. Sefat, D. L. Wood, C. Daniel, S. Dhar, V. Mahajan, M. Lee, F. Albano, *Sci. Rep.* **2016**, *6*, 26532.

[99] Y. Su, J. Hao, X. Liu, Y. Yang, *Batter. Supercaps* **2022**, https://doi.org/10.1002/batt.202200359.

[100] X. Han, Y. Gong, K. Fu, X. He, G. T. Hitz, J. Dai, A. Pearse, B. Liu, H. Wang, G. Rubloff, Y. Mo, V. Thangadurai, E. D. Wachsman, L. Hu, *Nat. Mater.* **2017**, *16*, 572.

[101] B. Wang, Y. Zhao, M. N. Banis, Q. Sun, K. R. Adair, R. Li, T.-K. Sham, X. Sun, *ACS Appl. Mater. Interfaces* **2018**, *10*, 1654.

[102] J. Liu, M. N. Banis, X. Li, A. Lushington, M. Cai, R. Li, T.-K. Sham, X. Sun, *J. Phys. Chem. C* **2013**, *117*, 20260.

[103] A. C. Kozen, A. J. Pearse, C.-F. Lin, M. Noked, G. W. Rubloff, *Chem. Mater.* **2015**, *27*, 5324.

[104] D. M. Hausmann, E. Kim, J. Becker, R. G. Gordon, *Chem. Mater.* **2002**, *14*, 4350.

[105] D. M. Hausmann, R. G. Gordon, *J. Cryst. Growth* **2003**, *249*, 251.

[106] X. Liu, S. Ramanathan, A. Longdergan, A. Srivastava, E. Lee, T. E. Seidel, J. T. Barton, D. Pang, R. G. Gordon, *J. Electrochem. Soc.* **2005**, *152*, G213.

[107] S. D. Elliott, G. Scarel, C. Wiemer, M. Fanciulli, G. Pavia, *Chem. Mater.* **2006**, *18*, 3764.

[108] W. Weinreich, T. Tauchnitz, P. Polakowski, M. Drescher, S. Riedel, J. Sundqvist, K. Seidel, M. Shirazi, S. D. Elliott, S. Ohsiek, E. Erben, B. Trui, *J. Vac. Sci. Technol. A Vacuum, Surfaces, Film.* **2013**, *31*, 01A123.

[109] D. Kitsche, Y. Tang, Y. Ma, D. Goonetilleke, J. Sann, F. Walther, M. Bianchini, J. Janek, T. Brezesinski, *ACS Appl. Energy Mater.* **2021**, *4*, 7338.

[110] R. S. Negi, E. Celik, R. Pan, R. Stäglich, J. Senker, M. T. Elm, *ACS Appl. Energy Mater.* **2021**, *4*, 3369.

[111] W. Bao, G. Qian, L. Zhao, Y. Yu, L. Su, X. Cai, H. Zhao, Y. Zuo, Y. Zhang, H. Li, Z. Peng, L. Li, J. Xie, *Nano Lett.* **2020**, *20*, 8832.

[112] F. Schipper, H. Bouzaglo, M. Dixit, E. M. Erickson, T. Weigel, M. Talianker, J. Grinblat, L. Burstein, M. Schmidt, J. Lampert, C. Erk, B. Markovsky, D. T. Major, D. Aurbach, *Adv. Energy Mater.* **2018**, *8*, 1701682.

[113] S. Liu, Z. Dang, D. Liu, C. Zhang, T. Huang, A. Yu, *J. Power Sources* **2018**, *396*, 288.

[114] C. S. Yoon, U. H. Kim, G. T. Park, S. J. Kim, K. H. Kim, J. Kim, Y. K. Sun, *ACS Energy Lett.* **2018**, *3*, 1634.

[115] D. Kitsche, Y. Tang, H. Hemmelmann, F. Walther, M. Bianchini, A. Kondrakov, J. Janek, T. Brezesinski, *Small Sci.* **2022**, *2*, 2200073.

[116] Y. Gao, R. Jiang, Z. Dai, Z. Du, Y. Jin, G. Li, S. Hou, *ACS Appl. Energy Mater.* **2022**, *5*, 15069.

[117] A. M. Nolan, Y. Liu, Y. Mo, *ACS Energy Lett.* **2019**, 2444.

[118] S. Randau, D. A. Weber, O. Kötz, R. Koerver, P. Braun, A. Weber, E. Ivers-Tiffée, T. Adermann, J. Kulisch, W. G. Zeier, F. H. Richter, J. Janek, *Nat. Energy* **2020**, *5*, 259.

[119] S. Deng, Y. Sun, X. Li, Z. Ren, J. Liang, K. Doyle-Davis, J. Liang, W. Li, M. Norouzi Banis, Q. Sun, R. Li, Y. Hu, H. Huang, L. Zhang, S. Lu, J. Luo, X. Sun, *ACS Energy Lett.* **2020**, *5*, 1243.

[120] S. Deng, X. Li, Z. Ren, W. Li, J. Luo, J. Liang, J. Liang, M. N. Banis, M. Li, Y. Zhao, X. Li, C. Wang, Y. Sun, Q. Sun, R. Li, Y. Hu, H. Huang, L. Zhang, S. Lu, J. Luo, X. Sun, *Energy Storage Mater.* **2020**, *27*, 117.

[121] F. Zhao, Y. Zhao, J. Wang, Q. Sun, K. Adair, S. Zhang, J. Luo, J. Li, W. Li, Y. Sun, X. Li, J. Liang, C. Wang, R. Li, H. Huang, L. Zhang, S. Zhao, S. Lu, X. Sun, *Energy Storage Mater.* **2020**, *33*, 139.

[122] M. Putkonen, T. Aaltonen, M. Alnes, T. Sajavaara, O. Nilsen, H. Fjellvåg, *J.*

Mater. Chem. **2009**, *19*, 8767.

[123] A. Y. Kim, F. Strauss, T. Bartsch, J. H. Teo, T. Hatsukade, A. Mazilkin, J. Janek, P. Hartmann, T. Brezesinski, *Chem. Mater.* **2019**, *31*, 9664.

[124] A. Y. Kim, F. Strauss, T. Bartsch, J. H. Teo, J. Janek, T. Brezesinski, *Sci. Rep.* **2021**, *11*, 5367.

[125] D. Kitsche, F. Strauss, Y. Tang, N. Bartnick, A. Kim, Y. Ma, C. Kübel, J. Janek, T. Brezesinski, *Batter. Supercaps* **2022**, *5*, e202100397.

[126] Y.-G. Lee, S. Fujiki, C. Jung, N. Suzuki, N. Yashiro, R. Omoda, D.-S. Ko, T. Shiratsuchi, T. Sugimoto, S. Ryu, J. H. Ku, T. Watanabe, Y. Park, Y. Aihara, D. Im, I. T. Han, *Nat. Energy* **2020**, *5*, 299.

[127] S. Ito, S. Fujiki, T. Yamada, Y. Aihara, Y. Park, T. Y. Kim, S. W. Baek, J.-M. Lee, S. Doo, N. Machida, *J. Power Sources* **2014**, *248*, 943.

[128] R. S. Negi, Y. Yusim, R. Pan, S. Ahmed, K. Volz, R. Takata, F. Schmidt, A. Henss, M. T. Elm, *Adv. Mater. Interfaces* **2022**, *9*, 2101428.

[129] R. S. Negi, P. Minnmann, R. Pan, S. Ahmed, M. J. Herzog, K. Volz, R. Takata, F. Schmidt, J. Janek, M. T. Elm, *Chem. Mater.* **2021**, *33*, 6713.

[130] Y. J. Kim, R. Rajagopal, S. Kang, K. S. Ryu, *Chem. Eng. J.* **2020**, *386*, 123975.

[131] X. Liu, J. Shi, B. Zheng, Z. Chen, Y. Su, M. Zhang, C. Xie, M. Su, Y. Yang, *ACS Appl. Mater. Interfaces* **2021**, *13*, 41669.

[132] R. Jung, R. Morasch, P. Karayaylali, K. Phillips, F. Maglia, C. Stinner, Y. Shao-Horn, H. A. Gasteiger, *J. Electrochem. Soc.* **2018**, *165*, A132.

[133] S. E. Renfrew, B. D. McCloskey, *J. Am. Chem. Soc.* **2017**, *139*, 17853.

[134] J. Kim, O. Kim, C. Park, G. Lee, D. Shin, *J. Electrochem. Soc.* **2015**, *162*, A1041.

[135] J. Kim, M. Kim, S. Noh, G. Lee, D. Shin, *Ceram. Int.* **2016**, *42*, 2140.

[136] M. Bianchini, F. Fauth, P. Hartmann, T. Brezesinski, J. Janek, *J. Mater. Chem. A* **2020**, *8*, 1808.

[137] A. M. Ealias, M. P. Saravanakumar, *IOP Conf. Ser. Mater. Sci. Eng.* **2017**, *263*, 032019.

[138] M. J. Herzog, N. Gauquelin, D. Esken, J. Verbeeck, J. Janek, *Energy Technol.* **2021**, *9*, 2100028.

[139] J. G. Osorio, F. J. Muzzio, *Powder Technol.* **2015**, *278*, 46.

[140] M. J. Herzog, N. Gauquelin, D. Esken, J. Verbeeck, J. Janek, *ACS Appl. Energy Mater.* **2021**, *4*, 8832.

[141] R. J. Clément, Z. Lun, G. Ceder, *Energy Environ. Sci.* **2020**, *13*, 345.

[142] N. Yabuuchi, M. Takeuchi, M. Nakayama, H. Shiiba, M. Ogawa, K. Nakayama, T. Ohta, D. Endo, T. Ozaki, T. Inamasu, K. Sato, S. Komaba, *Proc. Natl. Acad. Sci. U. S. A.* **2015**, *112*, 7650.

6 Appendix

6.1 Supporting Information

6.1.1 Publication I

Supporting Information

A High Performance All-Solid-State Battery with Ni-Rich NCM Cathode Coated by ALD and Lithium Thiophosphate Solid Electrolyte

David Kitsche,[†] Yushu Tang,[‡] Yuan Ma,[†] Damian Goonetilleke,[†] Joachim Sann,[#] Felix Walther,[#] Matteo Bianchini,[†,§] Jürgen Janek,[†,#,*] and Torsten Brezesinski[†,*]

[†] Battery and Electrochemistry Laboratory, Institute of Nanotechnology, Karlsruhe Institute for Technology (KIT), Hermann-von-Helmholtz-Platz 1, 76344 Eggenstein-Leopoldshafen, Germany.

[‡] Institute of Nanotechnology, Karlsruhe Institute for Technology (KIT), Hermann-von-Helmholtz-Platz 1, 76344 Eggenstein-Leopoldshafen, Germany.

[#] Institute of Physical Chemistry & Center for Materials Science (ZfM/LaMa), Justus-Liebig-University Giessen, Heinrich-Buff-Ring 17, 35392 Giessen, Germany.

[§] BASF SE, Carl-Bosch-Str. 38, 67056 Ludwigshafen, Germany.

*Email: juergen.janek@kit.edu, torsten.brezesinski@kit.edu

The data shown in **Figures S1**-**S3** are based on a different ALD pulse protocol. Here, each cycle consisted of five consecutive 0.1 s pulses of H_2O or O_3, with 2 s reactor purging in between and 60 s purging before switching to the TEMAH precursor.

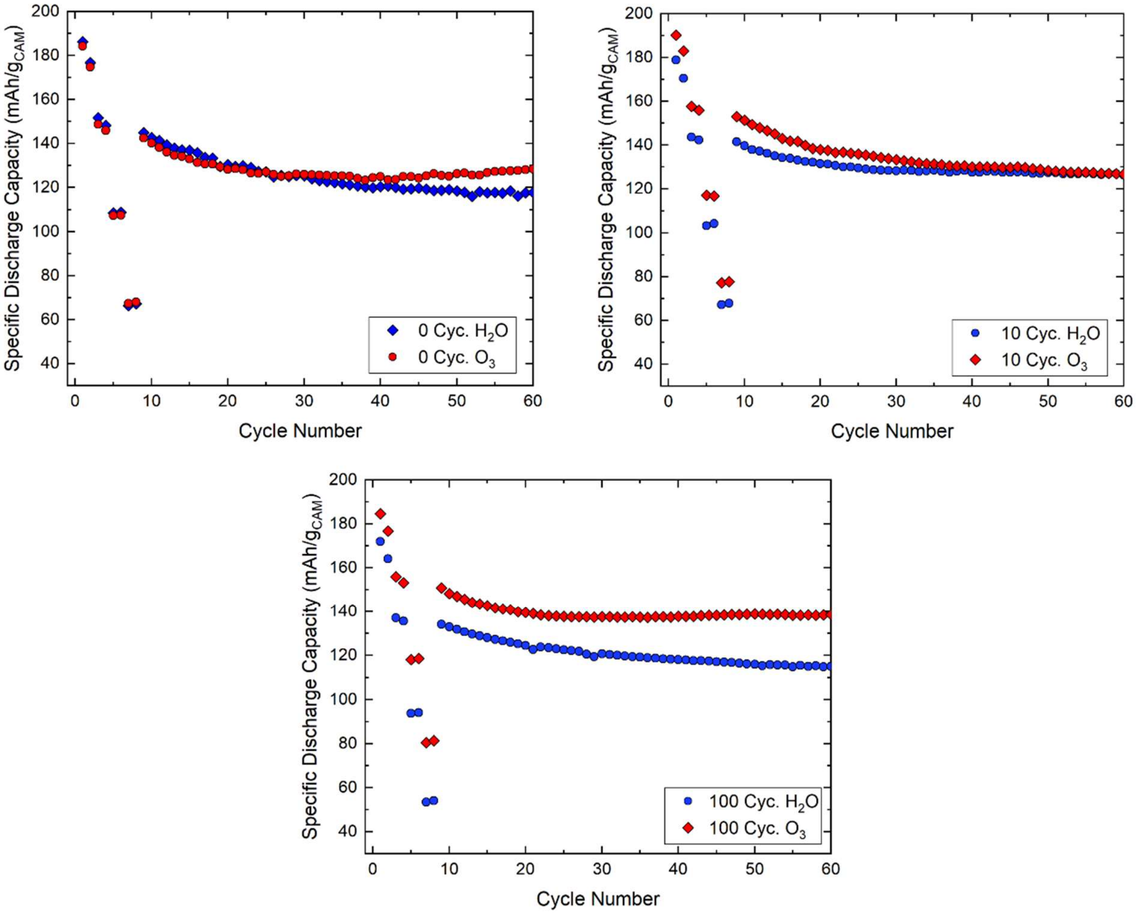

Figure S1. Comparison of cycling performance of the NCM-851005 CAM coated by ALD of TEMAH/H_2O or TEMAH/O_3 with 0 (no TEMAH exposure), 10, or 100 ALD cycles in SSB cells at 45 °C. The cells were cycled at rates of 0.1C, 0.2C, 0.5C, and 1C (two cycles at each C-rate), followed by 0.2C.

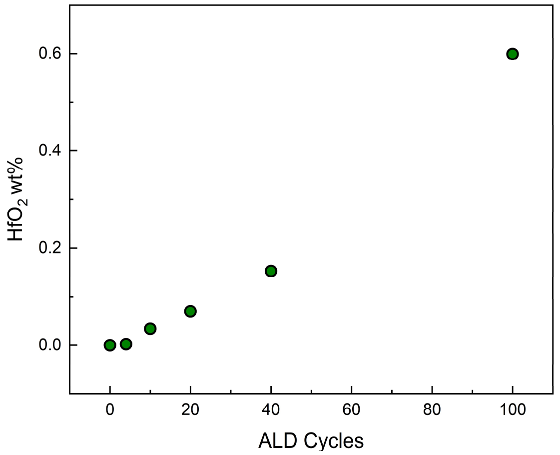

Figure S2. HfO_2 content of the NCM-851005 CAM versus the number of TEMAH/O_3 ALD cycles.

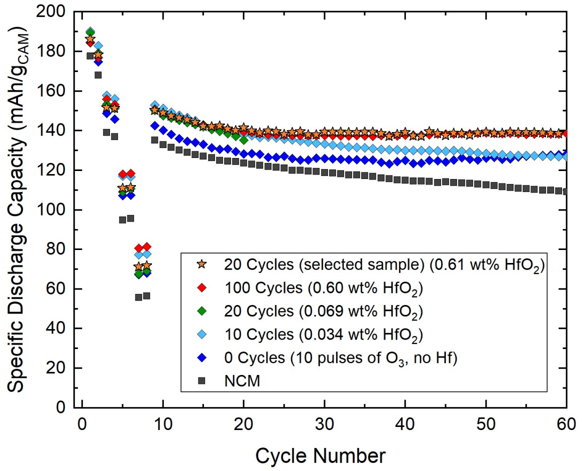

Figure S3. Electrochemical performance of the HfO_2-coated NCM-851005 CAM in SSB cells at 45 °C. The cells were cycled at rates of 0.1C, 0.2C, 0.5C, and 1C (two cycles at each C-rate), followed by 0.2C. The coating was prepared with varying numbers of TEMAH/O_3 ALD cycles. Each ALD cycle consisted of five pulses of both precursors (100 pulses in case of the sample discussed in the main text).

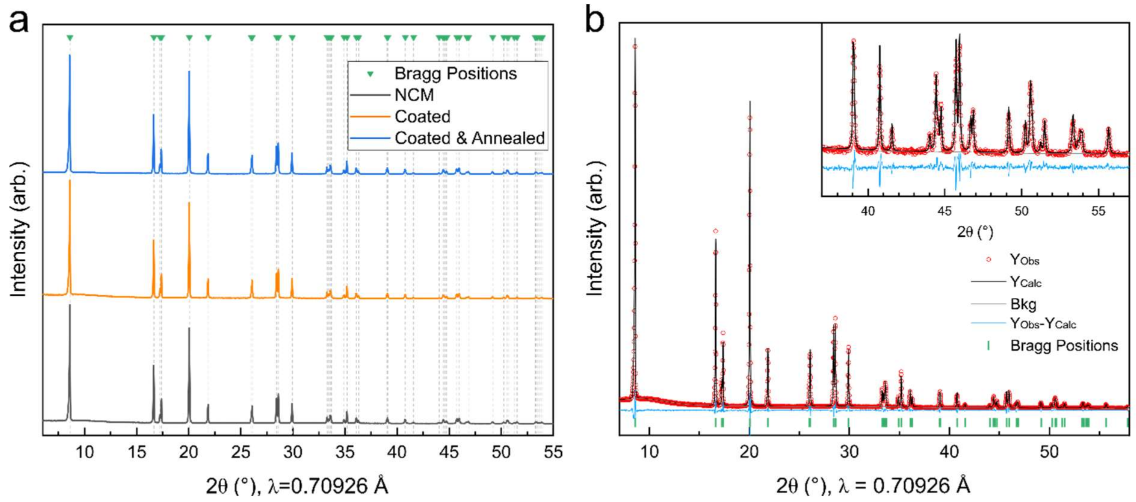

Figure S4. (a) Normalized XRD patterns collected from the NCM-851005 CAM before and after coating, as well as after subsequent annealing. (b) Rietveld refinement profile of NCM structural model against experimental diffraction data showing a satisfactory agreement between observed and calculated data.

Table S1. Refined structural parameters of the NCM-851005 CAMs.

Sample	Rf (%)	*a* (Å)	*c* (Å)	*V* ($Å^3$)	*z* of O	u_{iso} Li site ($Å^2$)	u_{iso} TM site ($Å^2$)
NCM	2.07	2.86993 (7)	14.1872 (3)	101.197 (4)	0.2420 (2)	0.018 (2)	0.0052 (2)
Coated	2.52	2.86995 (7)	14.1867 (3)	101.195 (4)	0.2424 (2)	0.023 (3)	0.0063 (2)
Coated & Annealed	1.81	2.87013 (7)	14.1865 (3)	101.207 (4)	0.2418 (2)	0.019 (2)	0.0055 (2)

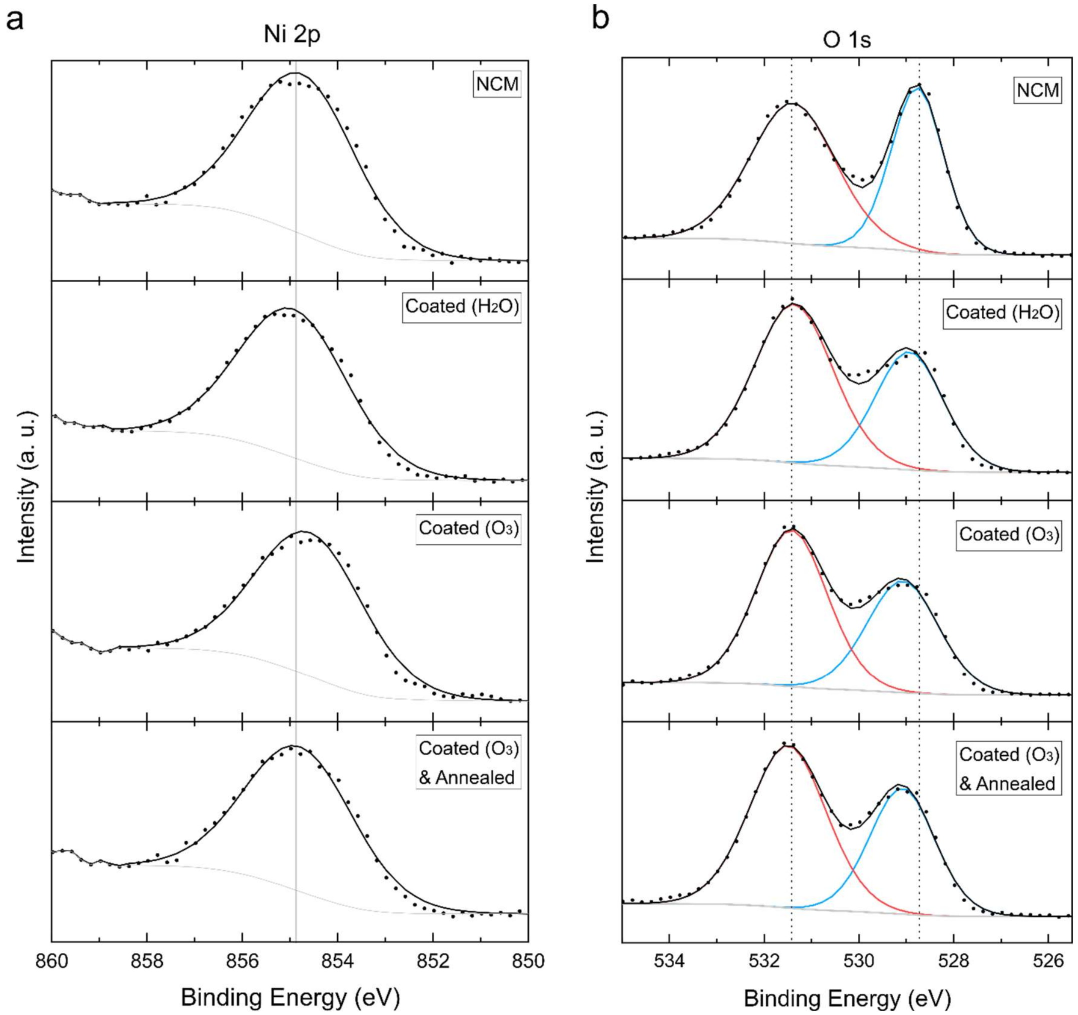

Figure S5. XP detail spectra of the (a) Ni 2p and (b) O 1s core levels. The O 1s spectra revealed an increase in surface carbonate and other adsorbed species (for the ALD-derived samples) typical of Ni-rich NCMs. This was corroborated by elemental analysis and is most likely due to reaction of the NCM-851005 CAM with CO_2 during the short exposure to ambient air upon sample loading and unloading into/from the ALD reactor. Furthermore, the peak at ~529 eV in the O 1s spectra of the ALD-derived samples smeared out towards higher binding energies while the Ni $2p_{3/2}$ signal smeared out (slightly) towards lower binding energies. This might be indicative of the formation of an oxygen-depleted surface layer.[1] However, it should be noted that the HfO_2 coating also contributes to the difference in peak intensity ratio.[2]

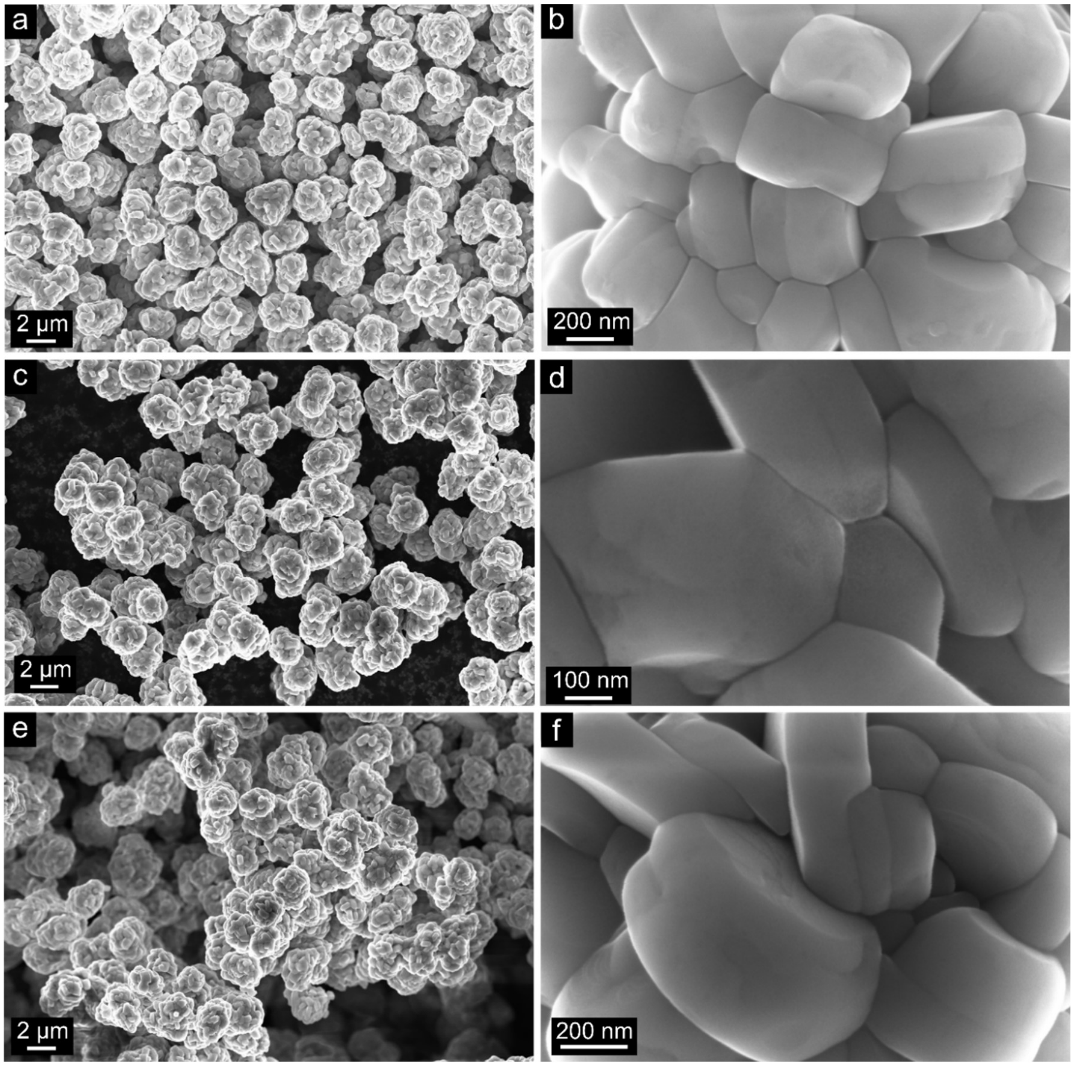

Figure S6. SEM images at different magnifications of the (a, b) uncoated, (c, d) as-prepared HfO_2-coated, and (e, f) annealed HfO_2-coated NCM-851005 CAMs.

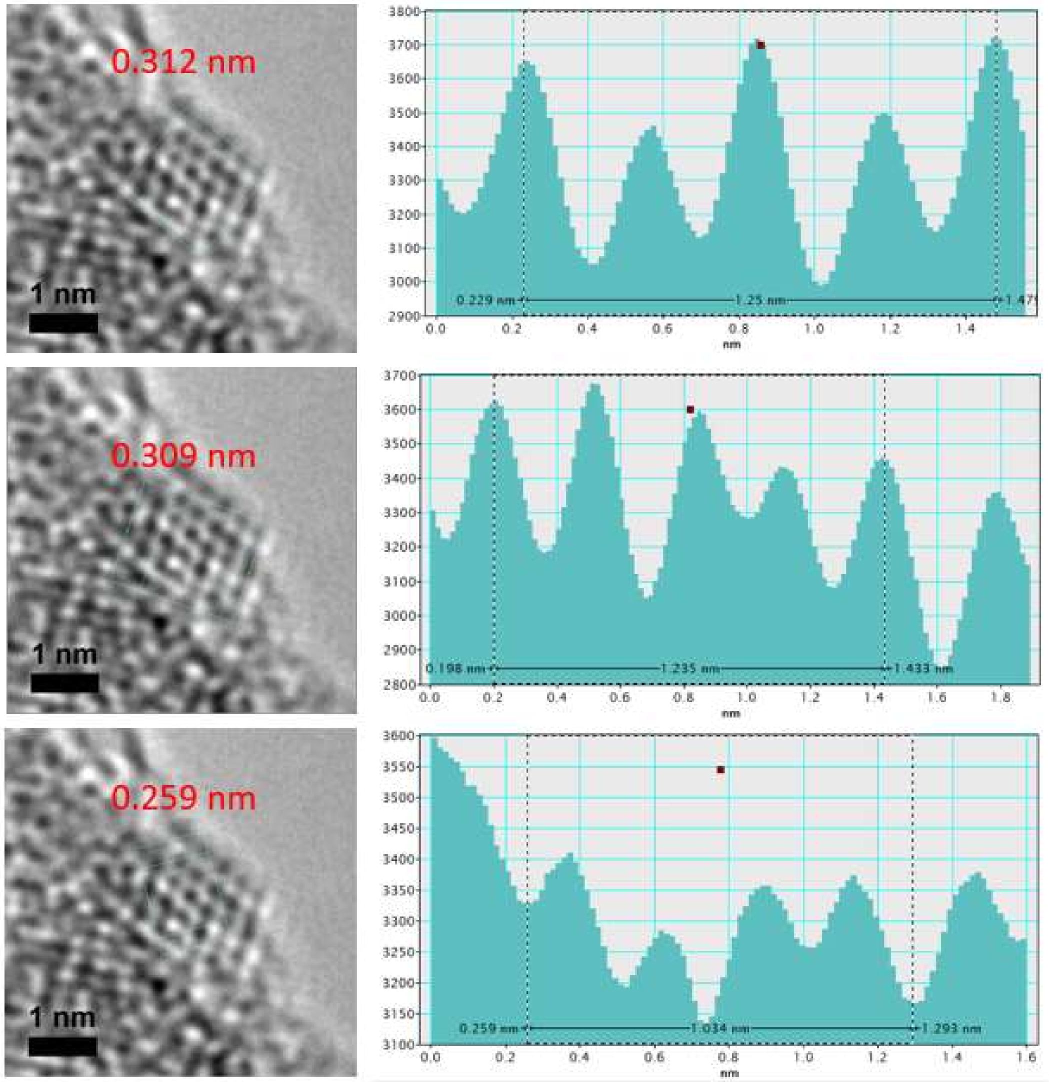

Figure S7. Calculation of lattice spacings to identify the crystal structure of HfO_2 nanoparticles on the surface of the as-prepared HfO_2-coated NCM-851005 CAM.

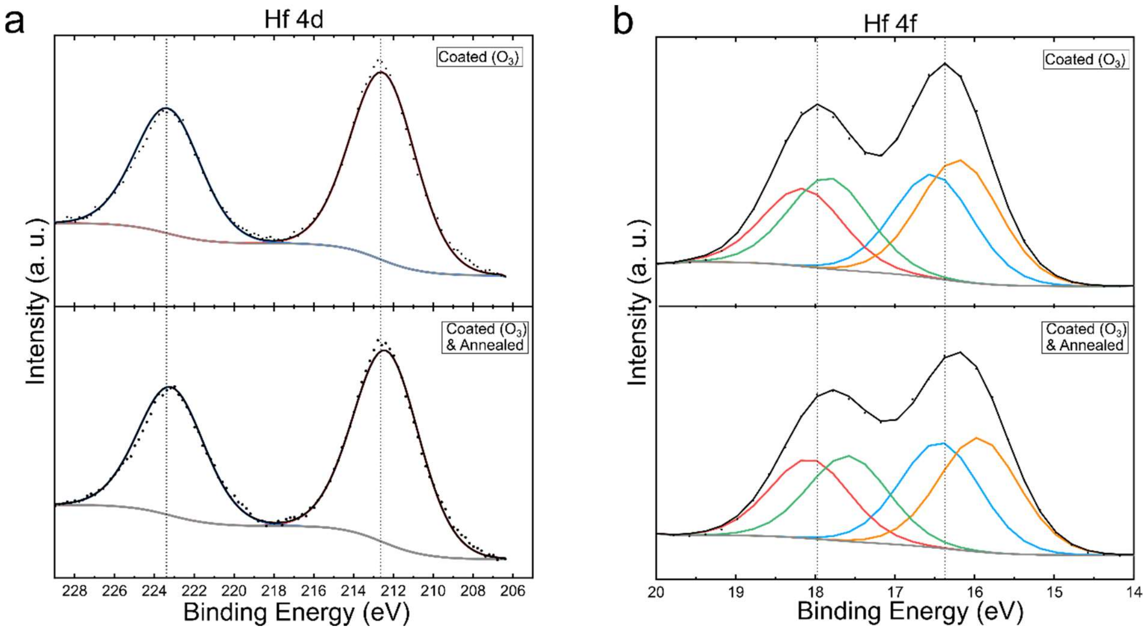

Figure S8. XP detail spectra of the (a) Hf 4d and (b) Hf 4f core levels.

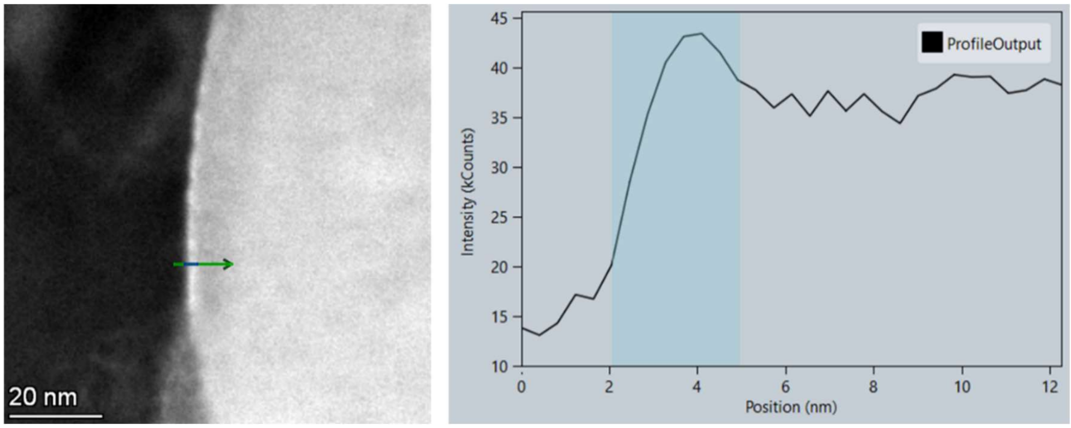

Figure S9. HAADF STEM image and determination of the coating thickness (line scan indicated by the green arrow) for the annealed HfO_2-coated NCM-851005 CAM.

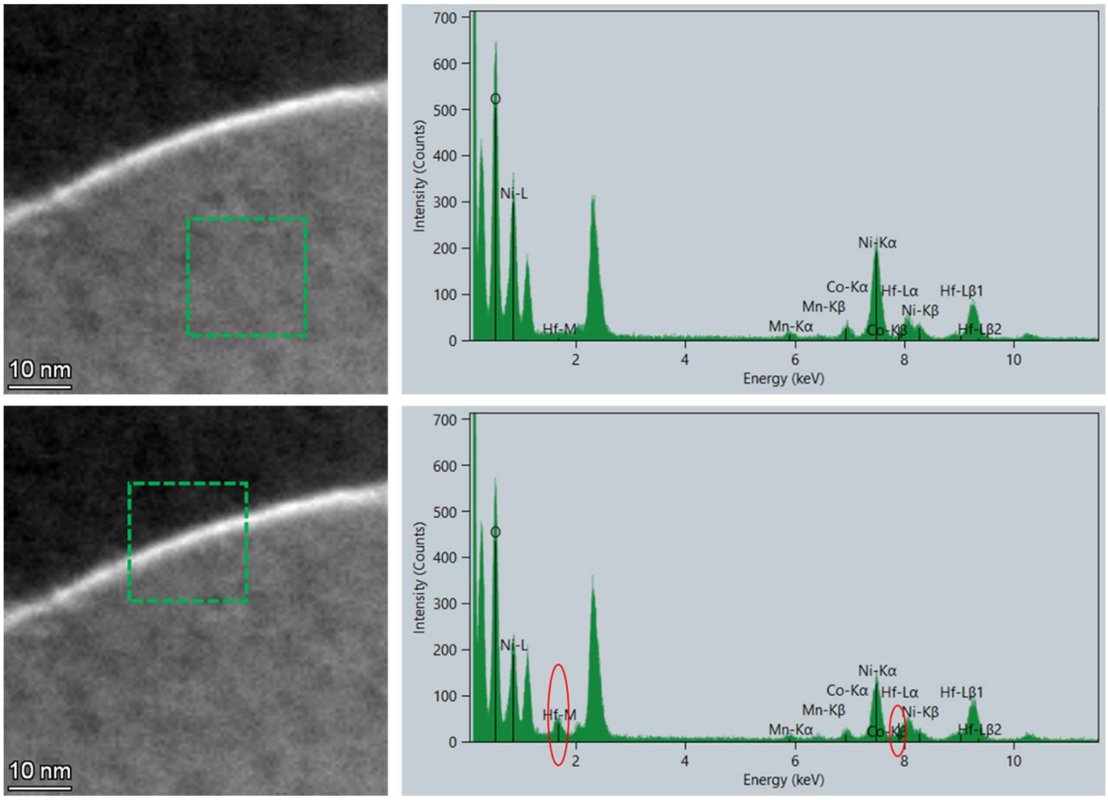

Figure S10. HAADF STEM images and EDX spectra of selected areas at or close to the surface of an annealed HfO_2-coated NCM-851005 CAM particle.

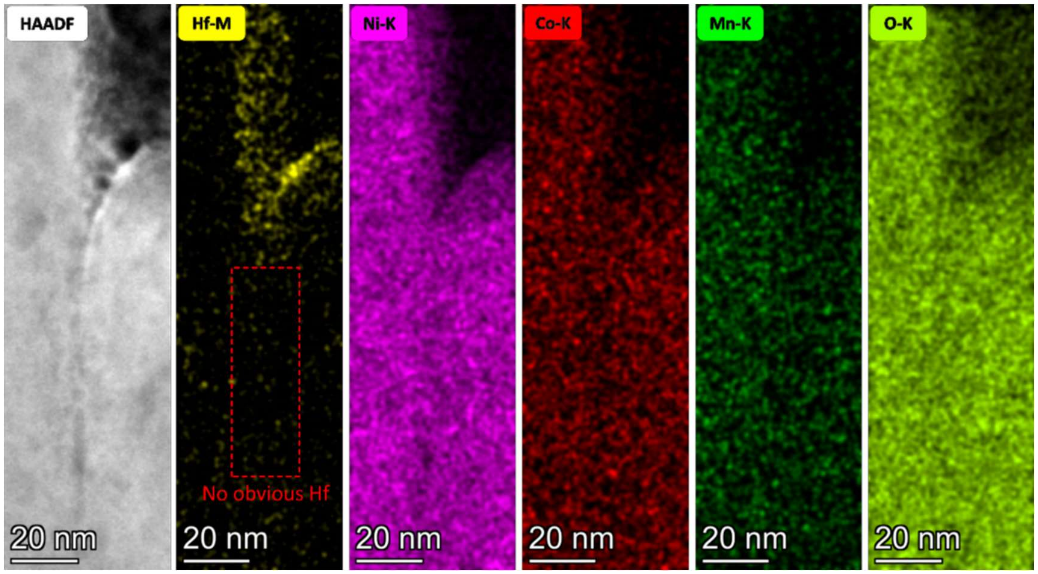

Figure S11. HAADF STEM image and elemental mapping of a FIB-cut cross section of an annealed HfO_2-coated NCM-851005 CAM particle (primary particle grain boundary).

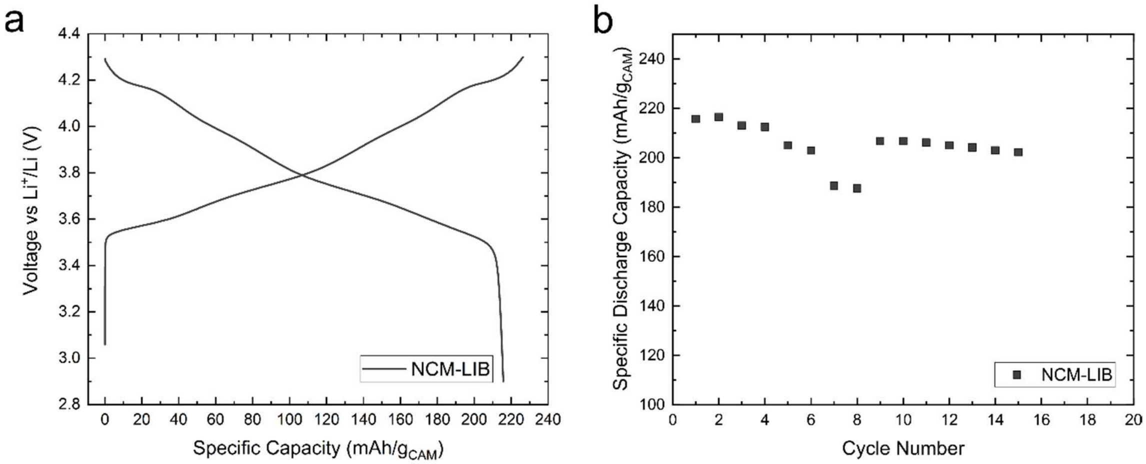

Figure S12. Electrochemical performance of the uncoated NCM-851005 CAM in liquid-electrolyte-based LIB coin cells at 45 °C. (a) First-cycle voltage profile at a rate of 0.1C. (b) Specific discharge capacity at 0.1C, 0.2C, 0.5C, and 1C (two cycles at each C-rate), followed by 0.2C cycling (with $j_{1C,LIB}$ = 2.0 mA/cm^2 vs $j_{1C,SSB}$ = 2.6 mA/cm^2). Similar initial specific charge capacities were achieved with the LIB cells (~226 mAh/g_{CAM} [LIB] vs ~219 mAh/g_{CAM} [SSB]). However, because of improved Coulombic efficiencies (~95 and 99% [LIB] vs ~81 and 96% [SSB] in the first two cycles), they delivered larger reversible capacities (~216 mAh/g_{CAM} [LIB] vs ~178 mAh/g_{CAM} [SSB]). Furthermore, as somewhat expected, their rate performance was superior (~188 mAh/g_{CAM} [LIB] vs ~56 mAh/g_{CAM} [SSB] at 1C).

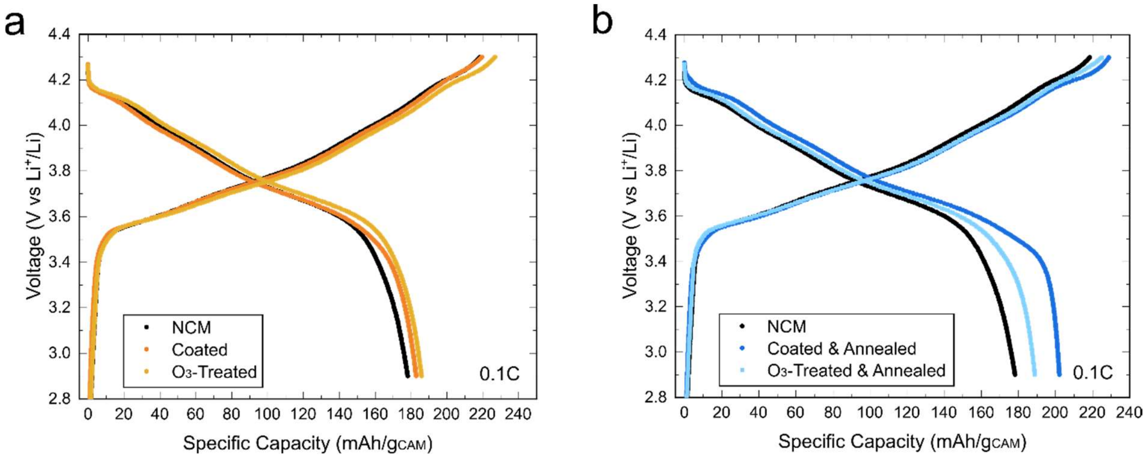

Figure S13. First-cycle voltage profiles of SSB cells at 45 °C. (a) HfO_2-coated NCM-851005 versus O_3-treated NCM-851005 (containing no Hf). (b) Annealed HfO_2-coated NCM-851005 versus annealed O_3-treated NCM-851005. Uncoated CAM is shown as a reference.

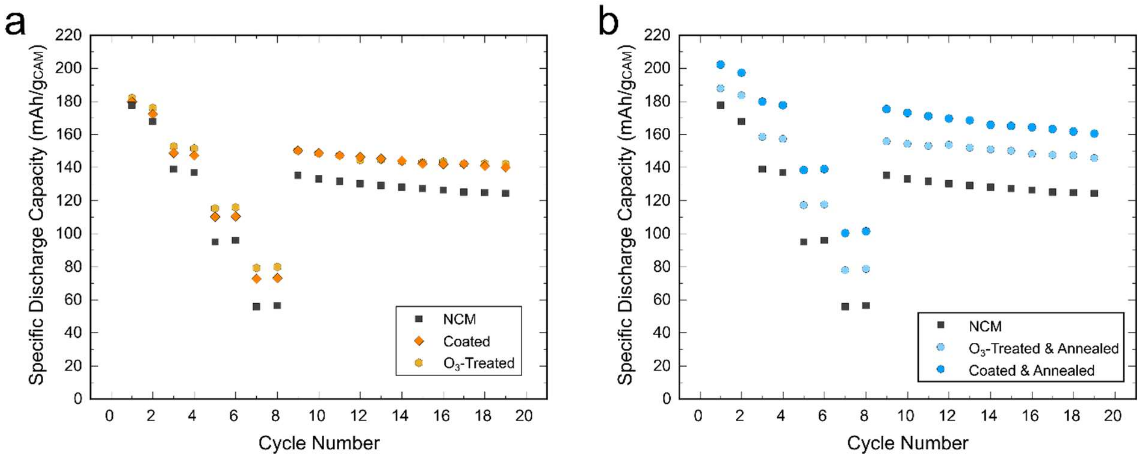

Figure S14. Cycling performance of the NCM-851005 CAMs in SSB cells at 45 °C. The cells were galvanostatically charged and discharged at 0.1C, 0.2C, 0.5C, and 1C (two cycles at each C-rate), followed by 0.2C cycling. (a) HfO_2-coated NCM-851005 versus O_3-treated NCM-851005 (containing no Hf). (b) Annealed HfO_2-coated NCM-851005 versus annealed O_3-treated NCM-851005. Uncoated CAM is shown as a reference.

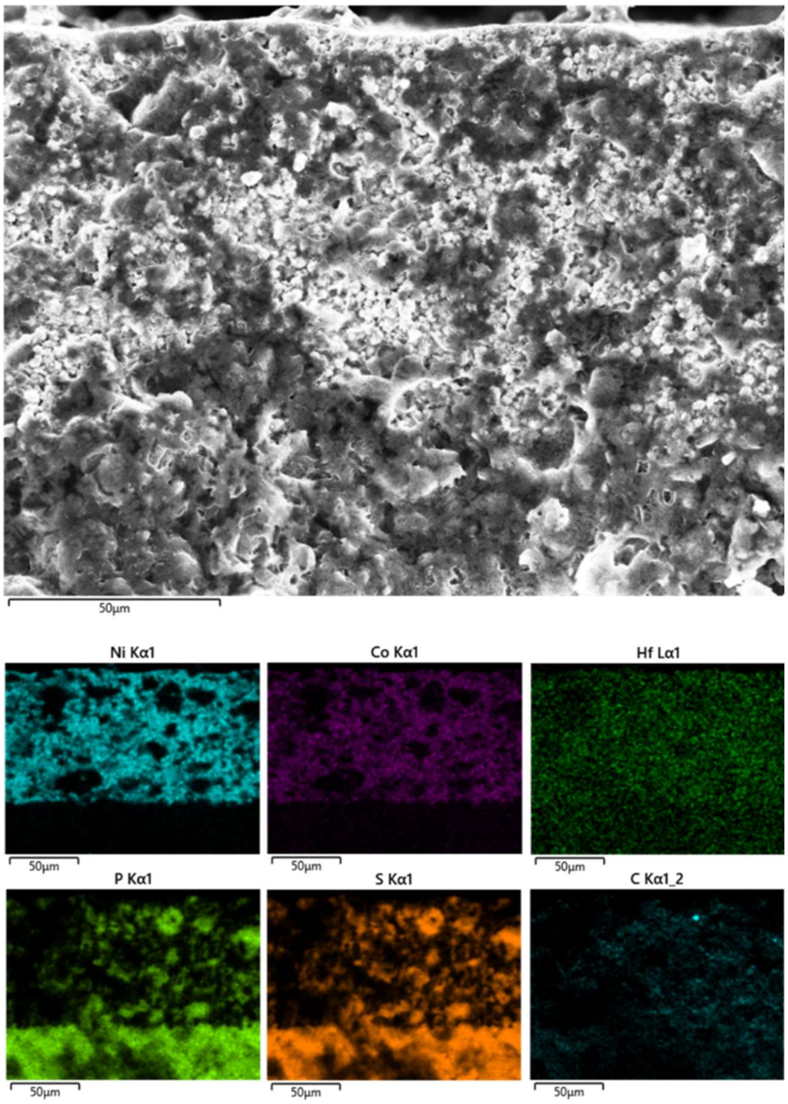

Figure S15. Cross-sectional SEM image and corresponding elemental maps of the cathode (including cathode/separator interface) of a SSB cell using the annealed HfO_2-coated NCM-851005 CAM before cycling.

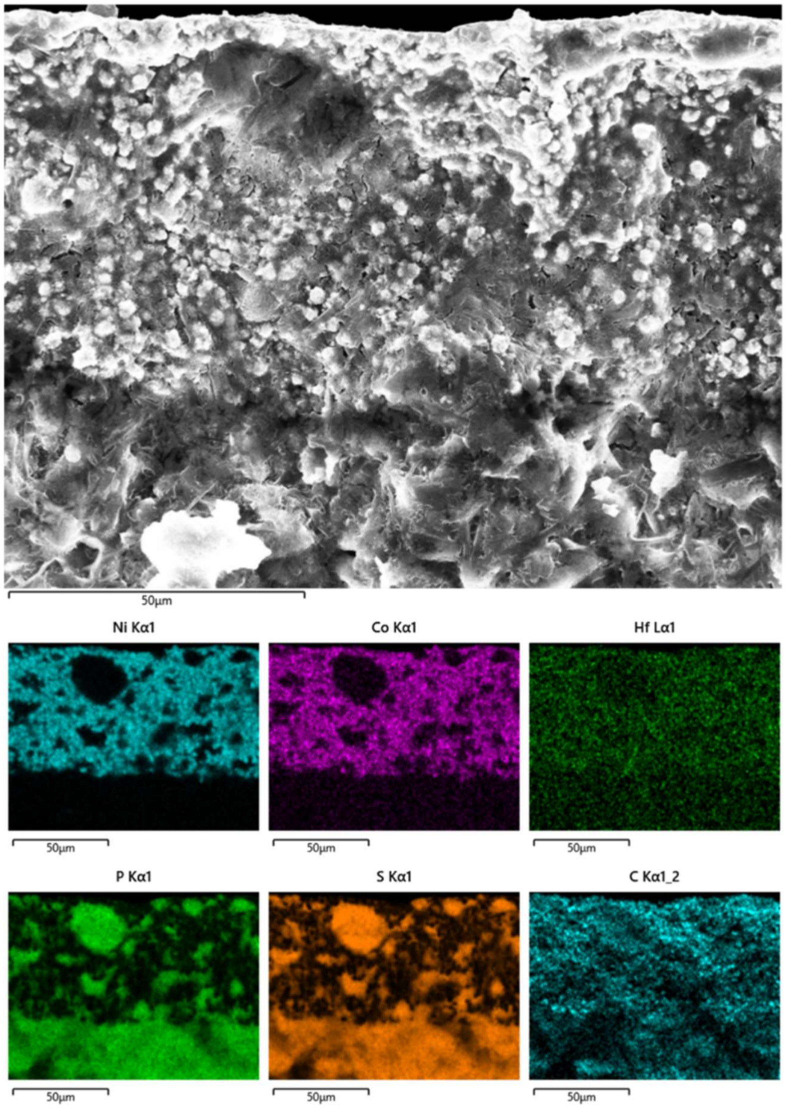

Figure S16. Cross-sectional SEM image and corresponding elemental maps of the cathode (including cathode/separator interface) of a SSB cell using the annealed HfO_2-coated NCM-851005 CAM after cycling (60 cycles at 0.5C rate and 45 °C).

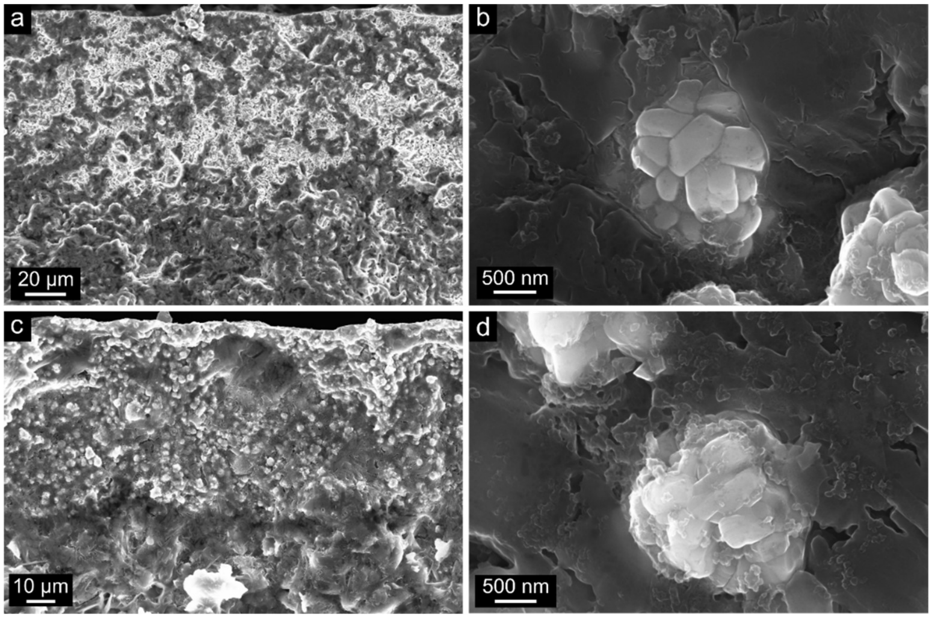

Figure S17. Cross-sectional SEM images at different magnifications of the cathode (including cathode/separator interface) of SSB cells using the annealed HfO_2-coated NCM-851005 CAM (a, b) before and (c, d) after cycling (60 cycles at 0.5C rate and 45 °C).

References

(1) Friedrich, F.; Strehle, B.; Freiberg, A. T. S.; Kleiner, K.; Day, S. J.; Erk, C.; Piana, M.; Gasteiger, H. A. Editors' Choice—Capacity Fading Mechanisms of NCM-811 Cathodes in Lithium-Ion Batteries Studied by X-ray Diffraction and Other Diagnostics. *J. Electrochem. Soc.* **2019**, *166*, A3760.

(2) Won, Y.; Park, S.; Koo, J.; Kim, S.; Kim, J.; Jeon, H. Initial Reaction of Hafnium Oxide Deposited by Remote Plasma Atomic Layer Deposition Method. *Appl. Phys. Lett.* **2005**, *87*, 262901.

6.1.2 Publication II

Supplementary Information (SI)

A Quasi-Multinary Composite Coating on a Ni-rich NCM Cathode Material for All-Solid-State Batteries

David Kitsche,[a] Florian Strauss,*[a] Yushu Tang,[b] Nikolai Bartnick,[a] A-Young Kim,[a] Yuan Ma,[a] Christian Kübel,[b, c, d, e] Jürgen Janek[a, f] and Torsten Brezesinski*[a]

[a] D. Kitsche, Dr. F. Strauss, N. Bartnick, Dr. A.-Y. Kim, Dr. Y. Ma, Prof. J. Janek, Dr. T. Brezesinski

Battery and Electrochemistry Laboratory, Institute of Nanotechnology, Karlsruhe Institute for Technology (KIT), Hermann-von-Helmholtz-Platz 1, 76344 Eggenstein-Leopoldshafen, Germany

Email: florian.strauss@kit.edu, torsten.brezesinski@kit.edu

[b] Dr. Y. Tang, Prof. C. Kübel

Institute of Nanotechnology, Karlsruhe Institute for Technology (KIT), Hermann-von-Helmholtz-Platz 1, 76344 Eggenstein-Leopoldshafen, Germany

[c] Prof. C. Kübel

Karlsruhe Nano Micro Facility (KNMF), Karlsruhe Institute for Technology (KIT), Hermann-von-Helmholtz-Platz 1, 76344 Eggenstein-Leopoldshafen, Germany

[d] Prof. C. Kübel

Helmholtz Institute Ulm (HIU), Helmholtzstr. 11, 89081 Ulm, Germany

[e] Prof. C. Kübel

Technical University Darmstadt, Department of Materials and Earth Sciences, Alarich-Weiss-Str. 2, 64287 Darmstadt

[f] Prof. J. Janek

Institute of Physical Chemistry & Center for Materials Research (ZfM/LaMa), Justus-Liebig-University Giessen, Heinrich-Buff-Ring 17, 35392 Giessen, Germany

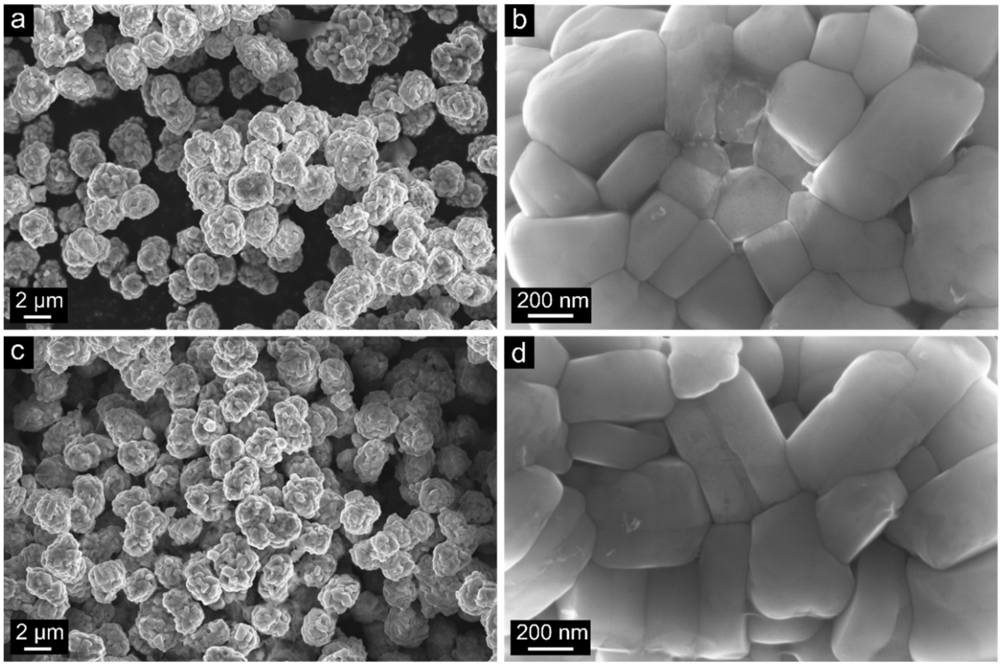

Figure S1. SEM images at different magnifications of LZNO-coated NCM-851005 CAMs. (a, b) LZNO-NCM-100, (c, d) LZNO-NCM-300.

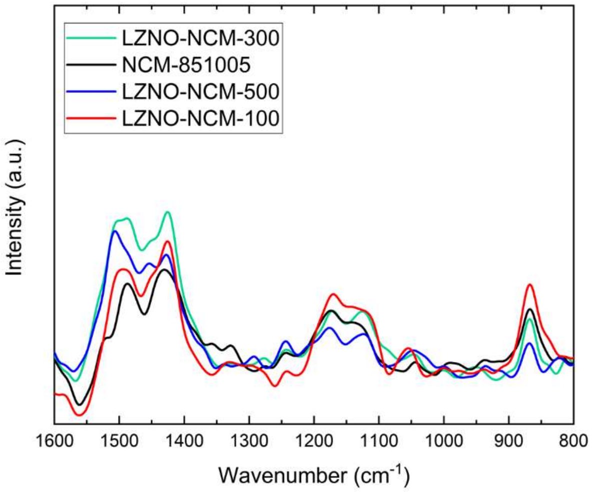

Figure S2. ATR-IR spectra of bare and LZNO-coated NCM-851005 CAMs. The vibrational bands at 1490/1430 cm^{-1} and 870 cm^{-1} represent stretching vibrations and in-plane deformations, respectively, confirming the presence of carbonate surface impurities. The bands at 1170 and 1130 cm^{-1} probably originate from the NCM-851005. Note that the raw spectra were background-corrected and smoothed using an FFT filter. According to elemental analysis, the Li_2CO_3 content is about 0.5 wt.%.

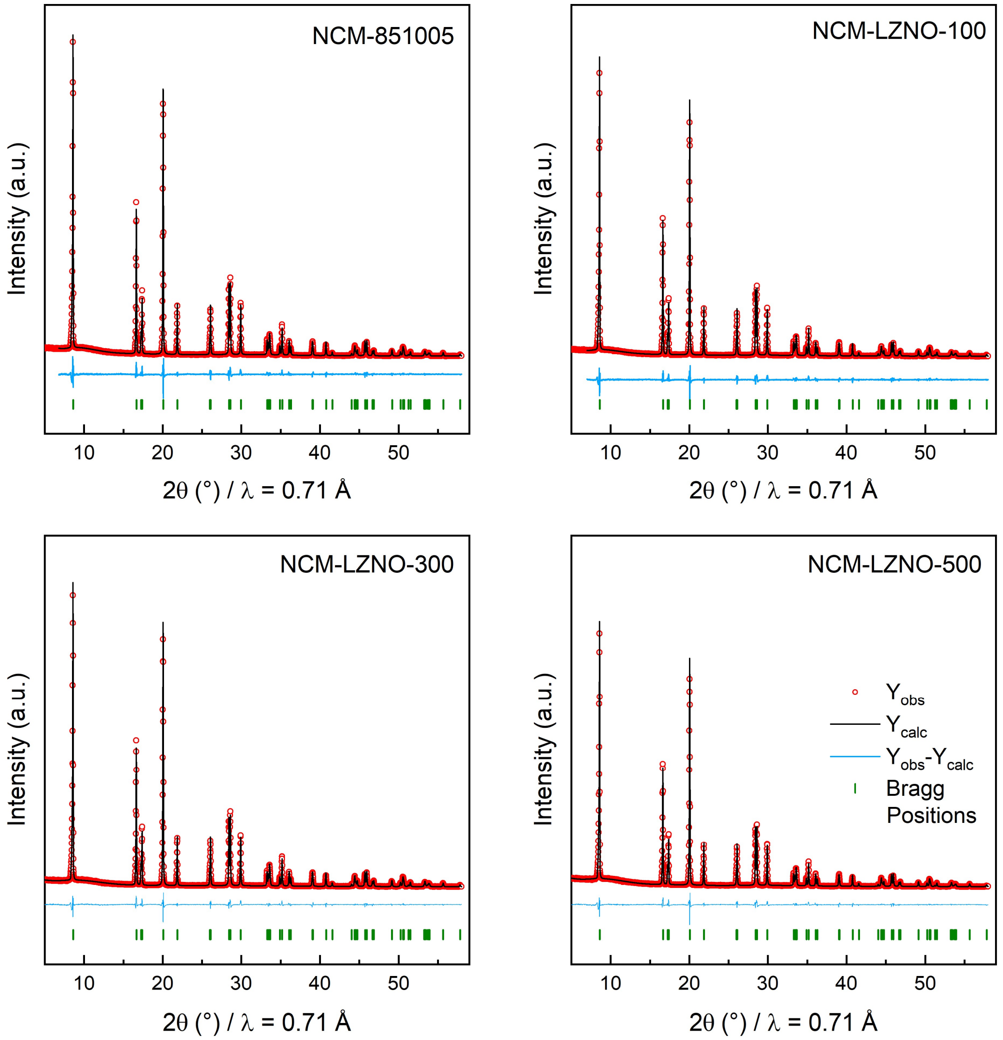

Figure S3. XRD patterns collected from bare and LZNO-coated NCM-851005 CAMs and corresponding Rietveld refinement profiles.

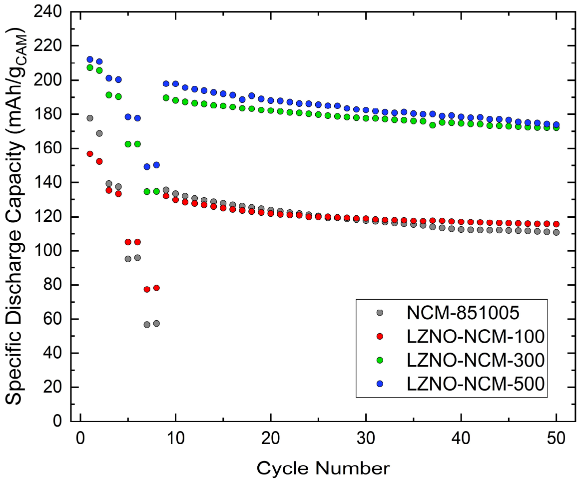

Figure S4. Electrochemical performance of bare and LZNO-coated NCM-851005 CAMs at 45 °C. The SSB cells were cycled in the voltage range 1.35-2.75 V vs $Li_4Ti_5O_{12}/Li_7Ti_5O_{12}$ (approximately 2.9-4.3 V vs Li^+/Li) at the rates of 0.1C, 0.2C, 0.5C and 1C (two cycles each), followed by 0.2C cycling.

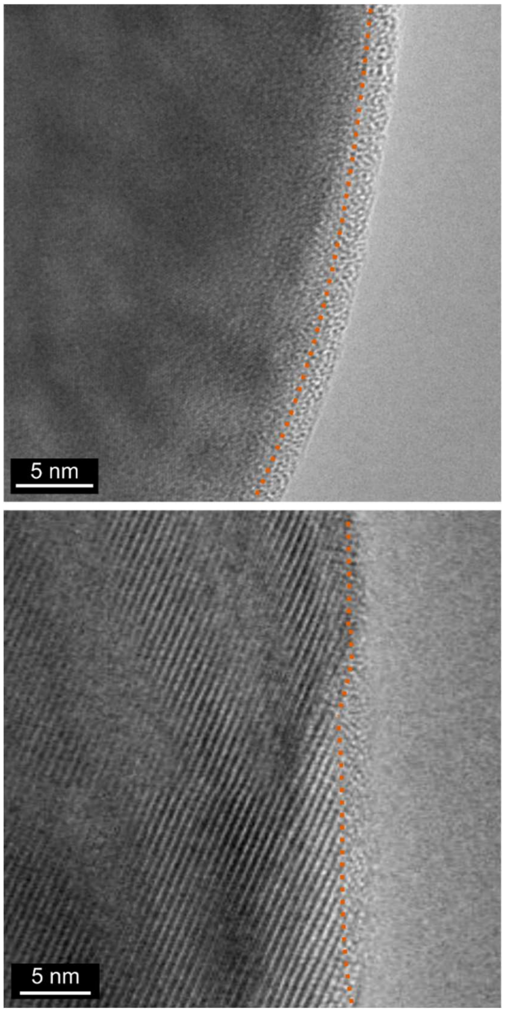

Figure S5. High-resolution TEM images of the LZNO-NCM-500 CAM particle surface. The dotted orange lines indicate the NCM-851005|LZNO interface.

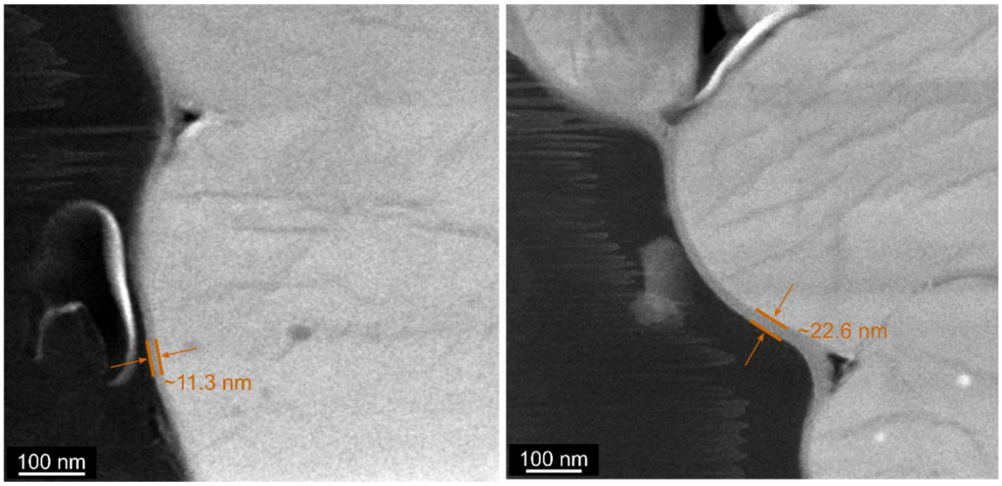

Figure S6. HAADF-STEM images of FIB-prepared LZNO-NCM-500 CAM particle cross-sections showing some thickness variation of the surface coating.

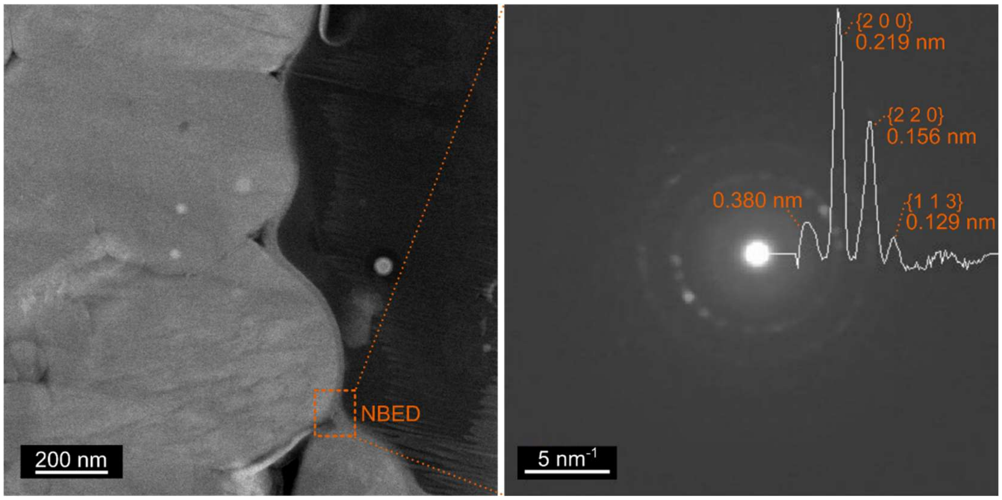

Figure S7. Left: HAADF-STEM image of a FIB-prepared LZNO-NCM-500 CAM particle cross-section. Right: NBED pattern indicating the presence of crystalline species in the surface coating. Reflections related to Li_3NbO_4 are indexed in the *Fm*−3*m* space group.

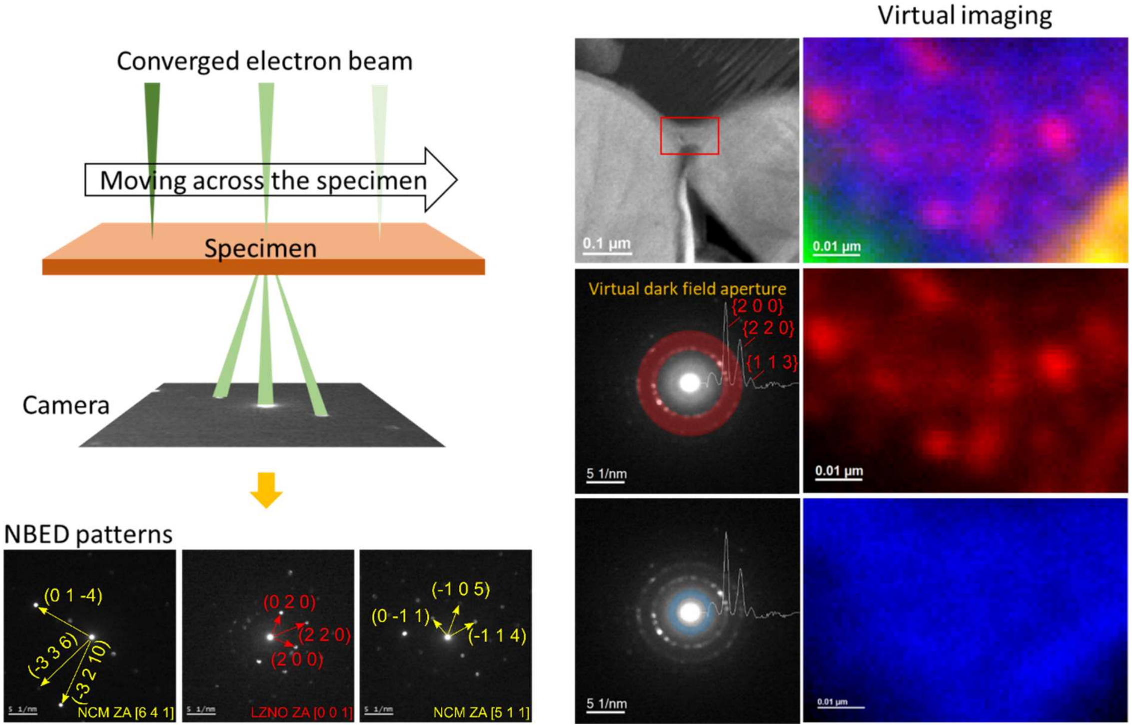

Figure S8. Schematic of the 4D-STEM analysis. For every pixel of the 2D real image of the region of interest (ROI, red rectangle), a 2D NBED pattern is recorded. A virtual dark-field aperture (red and blue circles) can be applied to generate a virtual image with contrast based on the areas contributing to the selected angular range. Selected reflections are indexed in the *R*−3*m* space group for NCM-851005 (yellow) and the *Fm*−3*m* space group for Li_3NbO_4 (red).

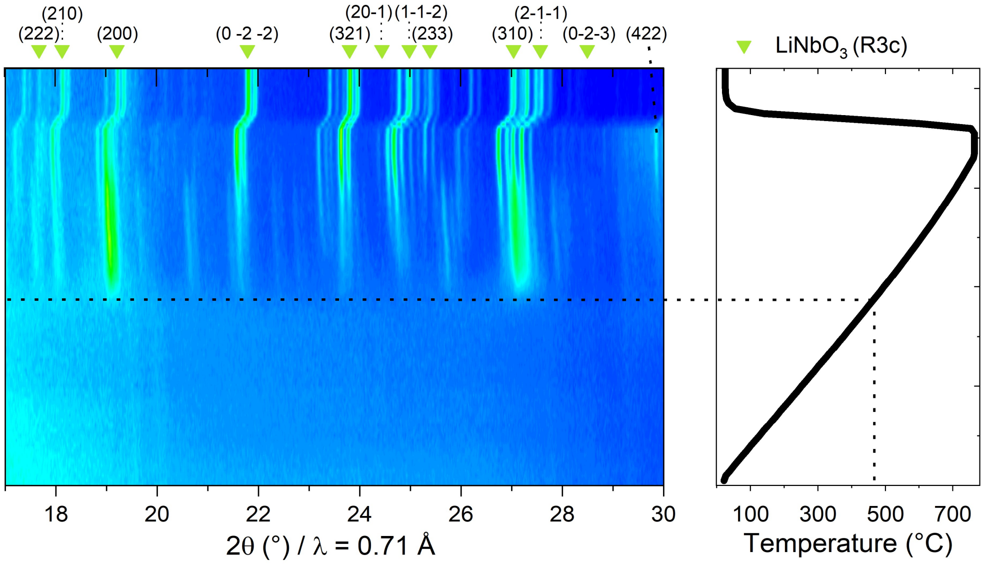

Figure S9. Left: Contour plot of XRD patterns from an *in situ* heating experiment. The reflections of the main component, $LiNbO_3$, are labeled and indexed in the space group *R*3*c*. The presence of at least one additional unknown phase is indicated. Right: Corresponding temperature profile. The dotted line indicates the onset of crystallization.

Comparison of LZNO with Li-Nb-O-based reference coatings

Figure S10 shows cycling data for SSB cells using the NCM-851005 CAM with LZNO and different reference coatings. The materials and chemicals used and the preparation of LZNO-NCM-300/500 are outlined in the experimental section of the manuscript.

LZNO coating without Zn

The reference sample “NCM-LZNO-no Zn” was prepared by adding the CAM powder (5.94 g) to a mixture of lithium ethoxide (512 µL), niobium ethoxide (683 µL) and 8500 µL absolute ethanol in an Ar-filled glovebox, followed by 30 min ultrasonication of the dispersion. Subsequently, the reaction mixture was dried in a vacuum overnight. The resultant powder was ground using a mortar and pestle and heated in an O_2 flow.

Lithium niobate coating with 3:1 Li:Nb ratio

The reference sample “NCM-“Li_3NbO_4”” was prepared by adding the CAM powder (5.94 g) to a mixture of lithium ethoxide (1024 µL), niobium ethoxide (683 µL) and 8500 µL absolute ethanol in an Ar-filled glovebox, followed by 30 min ultrasonication of the dispersion. Subsequently, the reaction mixture was dried in a vacuum overnight. The resultant powder was ground using a mortar and pestle and heated in an O_2 flow.

Lithium niobate coating with 1:1 Li:Nb ratio

The reference sample "NCM-$LiNbO_3$" was prepared by adding the CAM powder (5.94 g) to a mixture of lithium ethoxide (406 µL), niobium ethoxide (812 µL) and 1000 µL absolute ethanol in an Ar-filled glovebox, followed by 30 min ultrasonication of the dispersion. Subsequently, the reaction mixture was dried in a vacuum overnight. The resultant powder was ground using a mortar and pestle and heated in an O_2 flow.

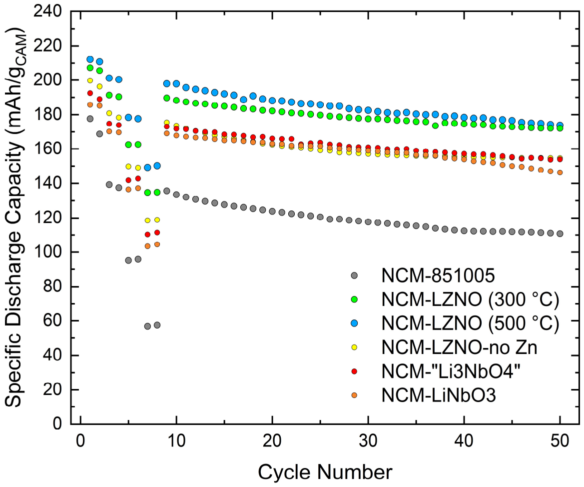

Figure S10. Electrochemical performance of bare and coated NCM-851005 CAMs (with LZNO and different Li-Nb-O-based reference coatings) at 45 °C. The SSB cells were cycled in the voltage range 1.35-2.75 V vs $Li_4Ti_5O_{12}/Li_7Ti_5O_{12}$ (approximately 2.9-4.3 V vs Li^+/Li) at the rates of 0.1C, 0.2C, 0.5C and 1C (two cycles each), followed by 0.2C cycling.

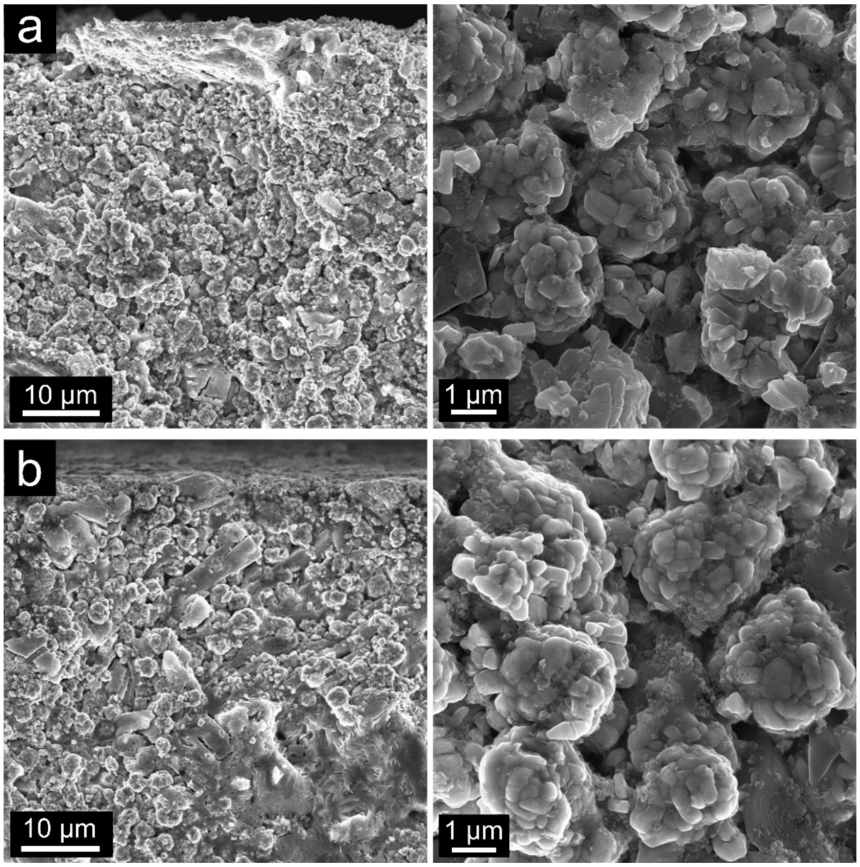

Figure S11. Cross-sectional SEM images at different magnifications of cathodes using (a) bare NCM-851005 and (b) LZNO-NCM-500 after 200 cycles at 45 °C and 1C rate.

6.1.3 Publication III

Supporting Information

Atomic Layer Deposition Derived Zirconia Coatings on Ni-Rich Cathodes in Solid-State Batteries: Correlation Between Surface Constitution and Cycling Performance

David Kitsche,[a] Yushu Tang,[b] Hendrik Hemmelmann,[c] Felix Walther,[c] Matteo Bianchini,[a,d] Aleksandr Kondrakov,[a,d] Jürgen Janek[a,c] and Torsten Brezesinski*[a]

[a] D. Kitsche, Prof. Matteo Bianchini, Dr. A. Kondrakov, Prof. J. Janek, Dr. T. Brezesinski

Battery and Electrochemistry Laboratory (BELLA), Institute of Nanotechnology, Karlsruhe Institute of Technology (KIT), Hermann-von-Helmholtz-Platz 1, 76344 Eggenstein-Leopoldshafen, Germany

Email: torsten.brezesinski@kit.edu

[b] Dr. Y. Tang

Institute of Nanotechnology, Karlsruhe Institute of Technology (KIT), Hermann-von-Helmholtz-Platz 1, 76344 Eggenstein-Leopoldshafen, Germany

[c] H. Hemmelmann, Dr. F. Walther, Prof. J. Janek

Institute of Physical Chemistry & Center for Materials Research (ZfM/LaMa), Justus-Liebig-University Giessen, Heinrich-Buff-Ring 17, 35392 Giessen, Germany

[d] Prof. Matteo Bianchini, Dr. A. Kondrakov

BASF SE, Carl-Bosch-Str. 38, 67056 Ludwigshafen, Germany

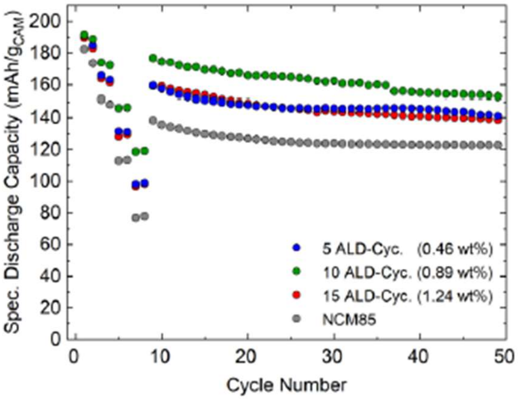

Figure S1. Electrochemical performance of the uncoated NCM85 and (as-coated) ZrO$_2$@NCM85 CAMs in SSB cells depending on the number of TEMAZ/O$_3$-ALD cycles. The cells were cycled at 45 °C in the voltage range 1.35-2.75 vs Li$_4$Ti$_5$O$_{12}$/Li$_7$Ti$_5$O$_{12}$ (approx. 2.9-4.3 V vs Li$^+$/Li) at rates ranging from 0.1C to 1C (two cycles each), followed by cycling at 0.2C.

Table S1. Crystallographic parameters from Rietveld refinement of XRD data collected from the uncoated NCM85 and ZrO$_2$@NCM85 CAMs.

Sample	**Rf (%)**	***a* (Å)**	***c* (Å)**	***V* (Å^3)**	***z* of O**	**B_{iso} O site (Å^2)**	**B_{iso} TM site (Å^2)**	**Ni^{2+} on Li site (%)**
NCM	4.98	2.8671(1)	14.1725(9)	100.892(9)	0.257(1)	0.5(3)	0.11(8)	2.5(0.9)
Z250	5.11	2.8675(1)	14.1734(9)	100.925(9)	0.257(1)	0.6(3)	0.22(9)	2.8(0.9)
Z300	4.48	2.8673(1)	14.1717(9)	100.900(9)	0.257(1)	0.5(3)	0.16(9)	3.2(1.0)
Z400	4.09	2.8675(1)	14.1734(9)	100.929(9)	0.257(1)	0.6(3)	0.17(8)	2.8(0.9)
Z550	4.62	2.8676(1)	14.1752(9)	100.950(9)	0.257(1)	0.5(3)	0.16(9)	2.5(1.0)
Z700	3.81	2.8676(1)	14.1755(9)	100.949(9)	0.257(1)	0.6(3)	0.21(8)	2.8(0.9)

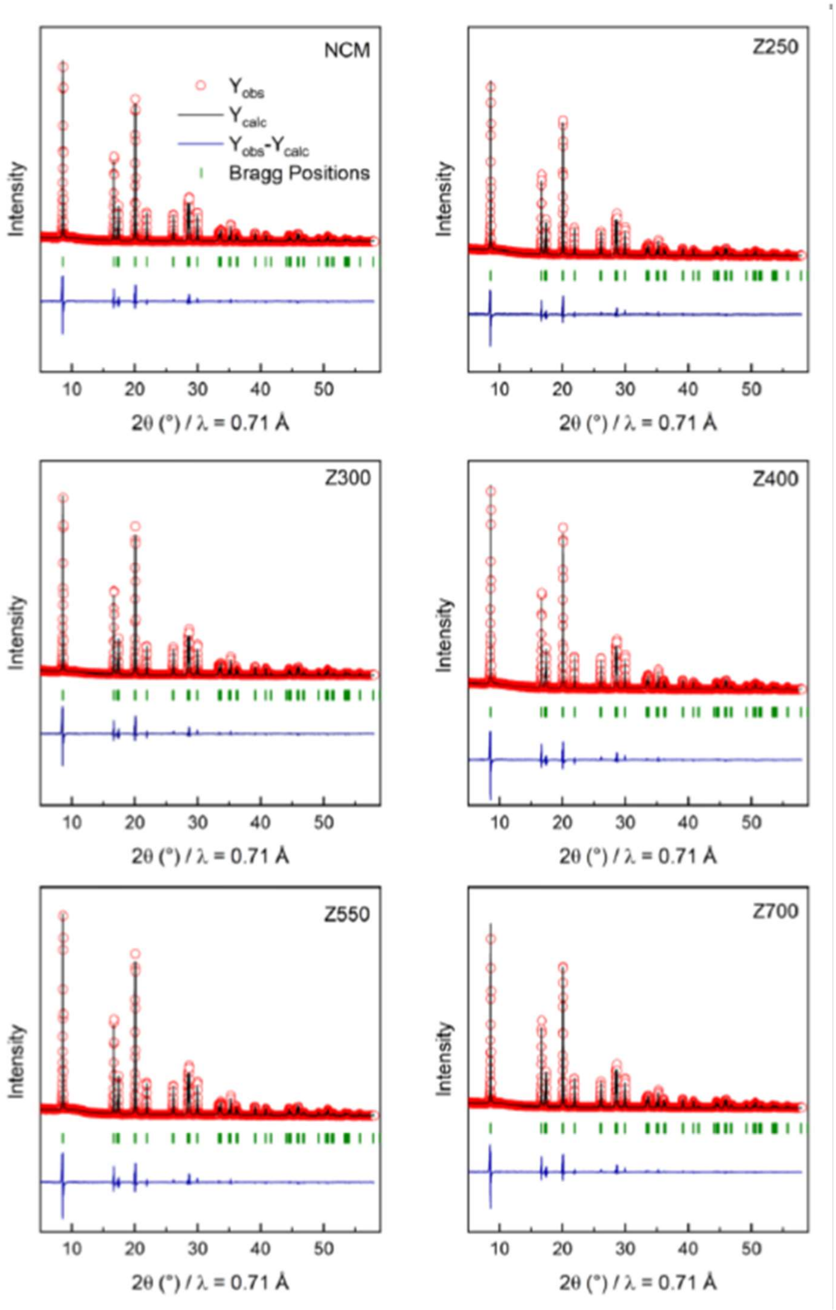

Figure S2. XRD patterns of the uncoated NCM85 and ZrO_2@NCM85 CAMs annealed at different temperatures and corresponding Rietveld refinement profiles.

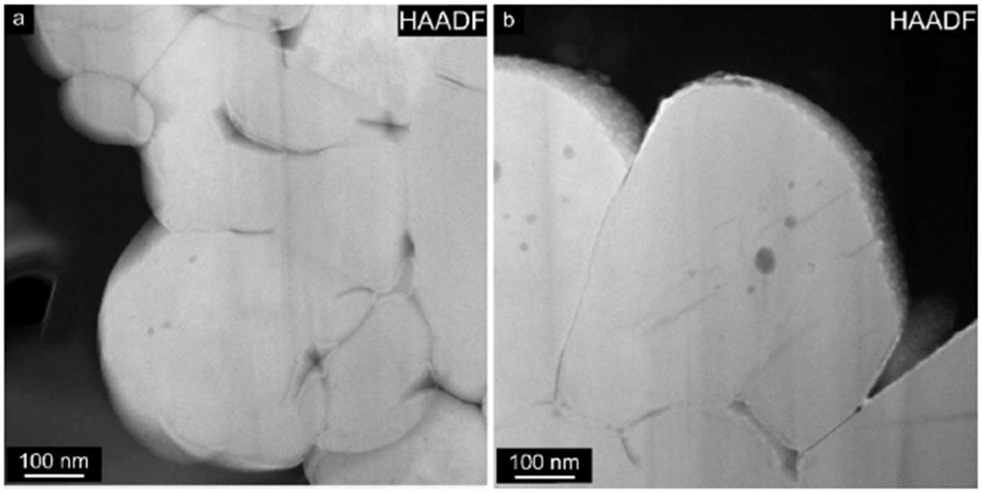

Figure S3. Low-magnification STEM-HAADF images of FIB-prepared particle cross-sections of (a) Z250 and (b) Z550 showing increasing surface roughness.

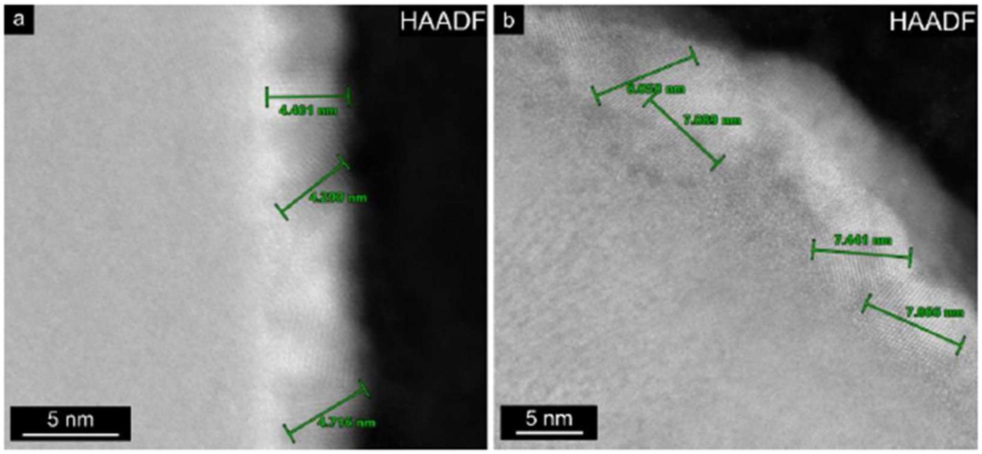

Figure S4. STEM-HAADF images of FIB-prepared particle cross-sections of (a) Z250 and (b) Z550, with indication of the approximate crystal size (ZrO_2).

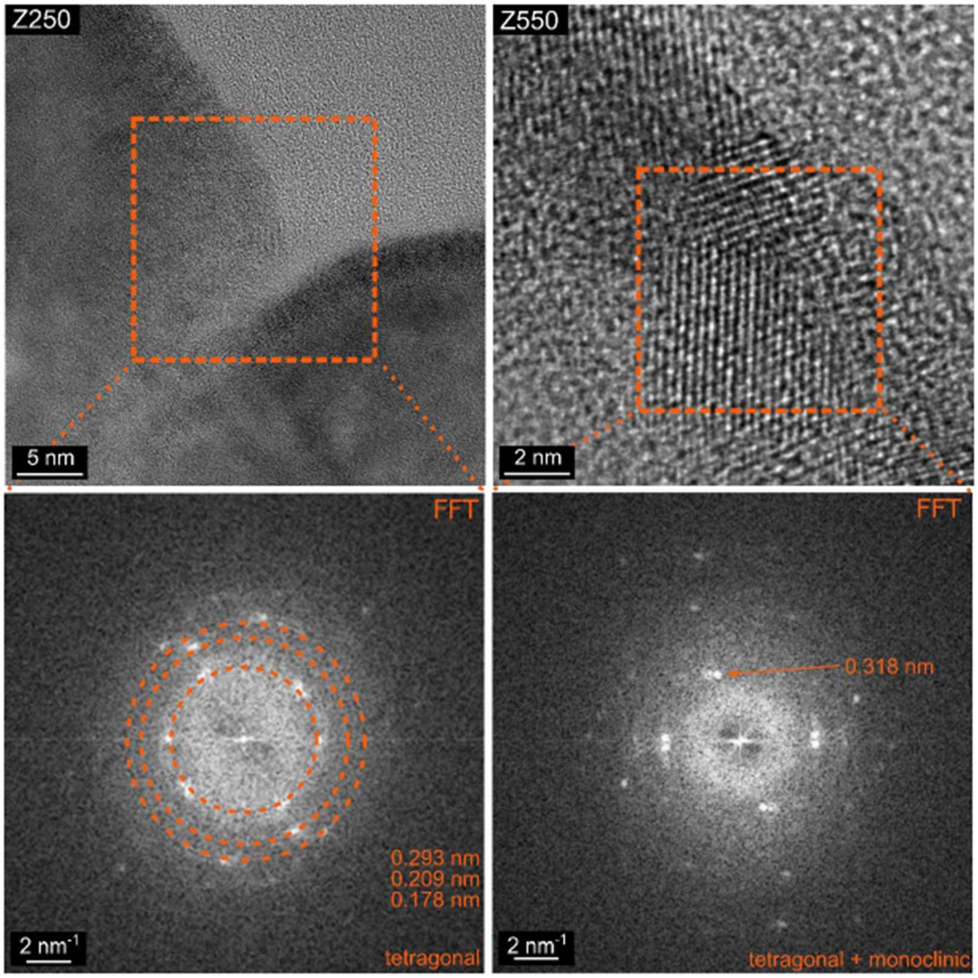

Figure S5. TEM images of FIB-prepared particle cross-sections of Z250 and Z550 and FFT patterns of the highlighted areas.

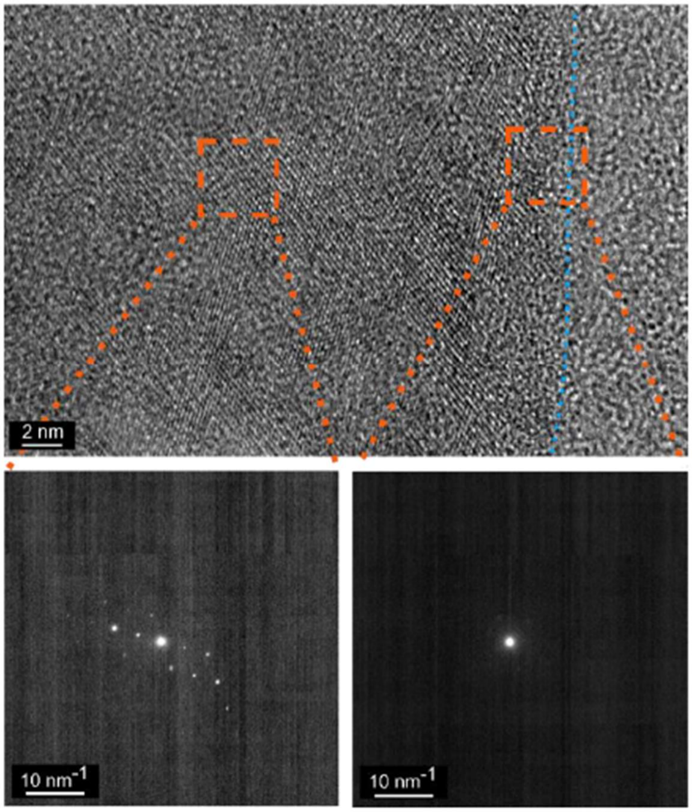

Figure S6. TEM image of a FIB-prepared particle cross-section of Z700 with NBED patterns collected from the surface and the “bulk". The blue dotted line indicates the boundary between NCM85 particle and FIB-deposited layer applied during sample preparation.

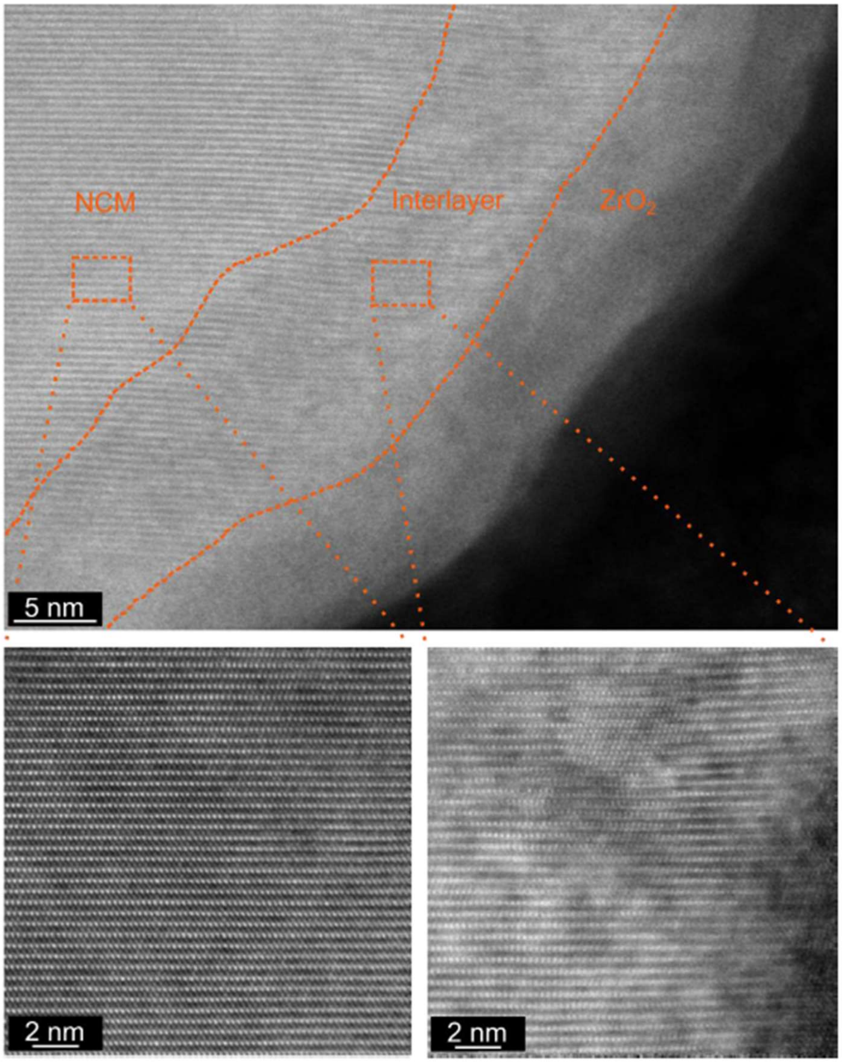

Figure S7. High-resolution STEM images of the Z700 particle surface, with dashed lines indicating the presence of an interlayer (between NCM85 and ZrO_2 coating). Dislocations are apparent in the interlayer.

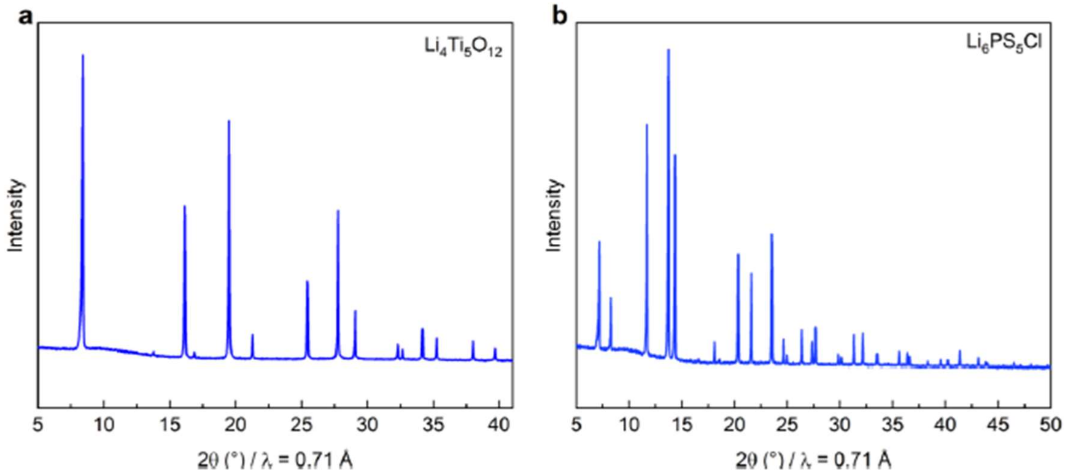

Figure S8. XRD patterns of (a) the anode material $Li_4Ti_5O_{12}$ and (b) the solid electrolyte Li_6PS_5Cl used for SSB cell testing in this study.

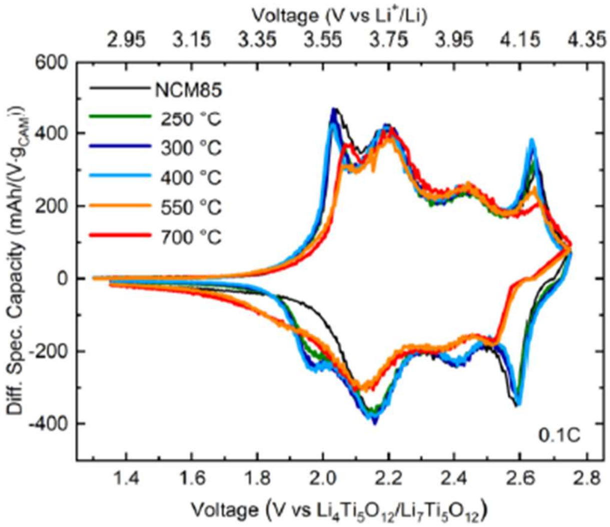

Figure S9. First-cycle differential capacity plots of the uncoated NCM85 and ZrO_2@NCM85 CAMs in SSB cells cycled at 0.1C and 45 °C in the voltage range 2.9-4.3 V vs Li^+/Li.

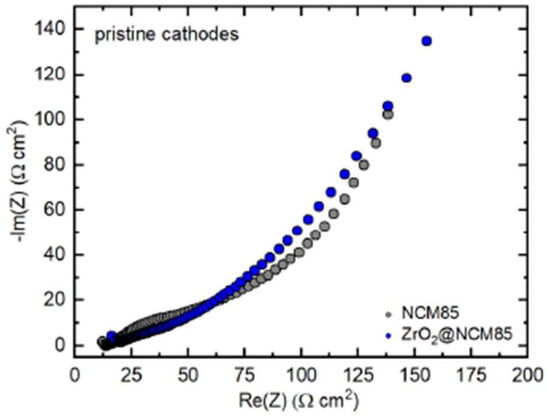

Figure S10. Nyquist plots of the electrochemical impedance of representative SSB cells in the pristine state at 45 °C.

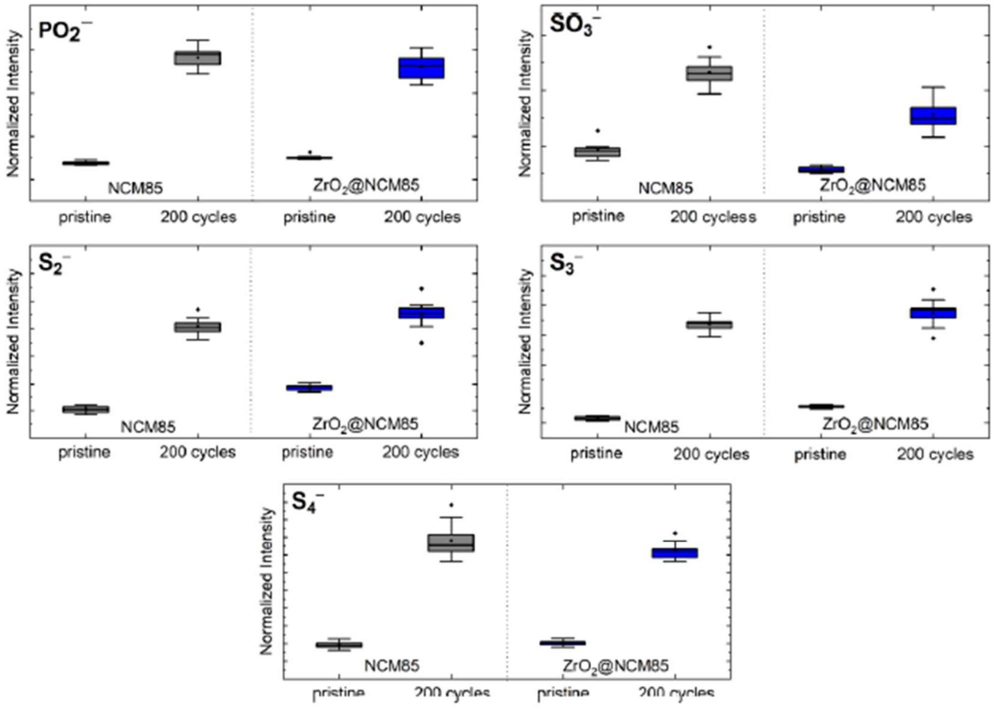

Figure S11. Box plots of measured intensities for species detected in the cycled cathodes by ToF-SIMS.

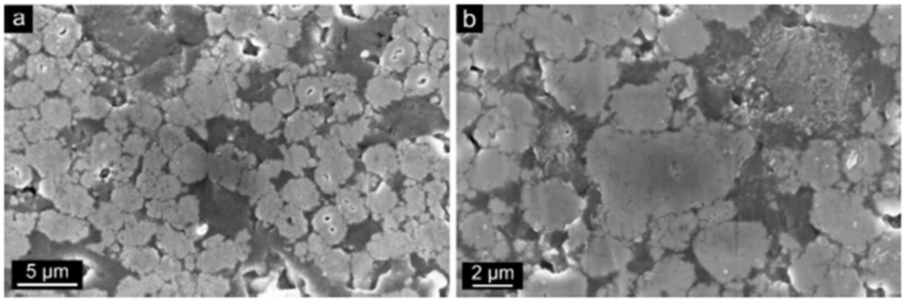

Figure S12. SEM images of pristine cathode cross-sections containing the uncoated NCM85 (prepared by ion milling).

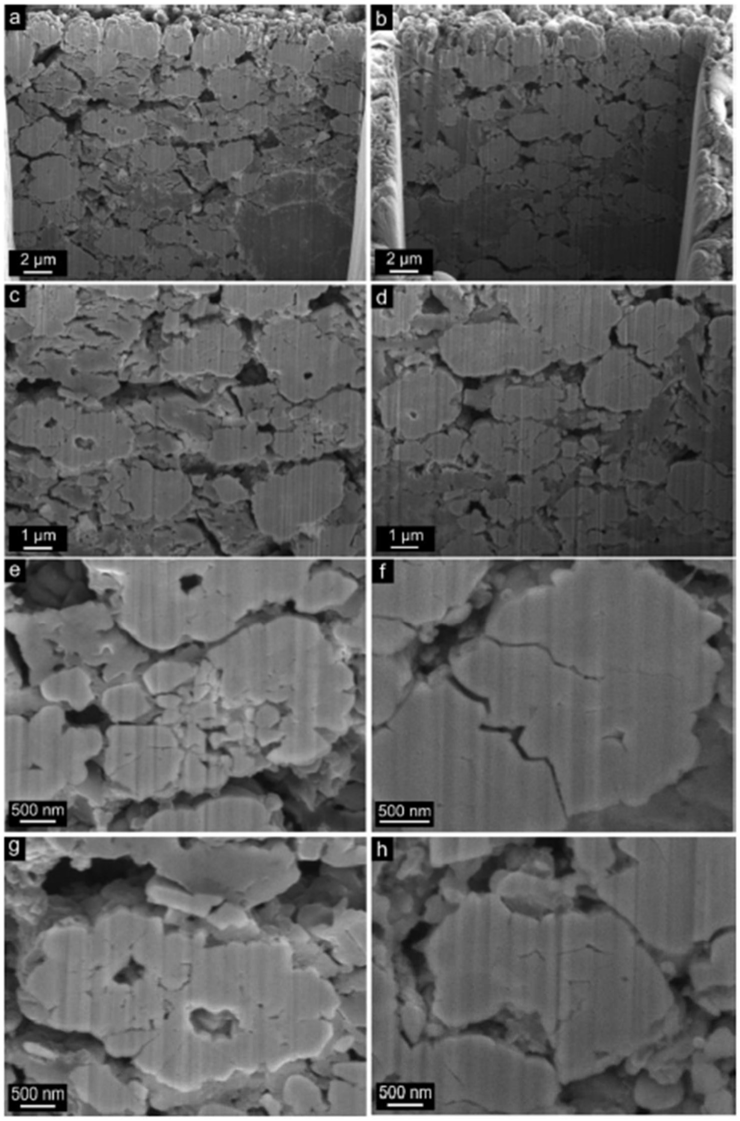

Figure S13. SEM images of FIB-prepared cross-sections of cathodes containing (left column) the uncoated NCM85 and (right column) ZrO_2@NCM85 after 200 cycles at 0.5C and 45 °C.

Estimating the diffusion coefficient for zirconium ions in NCM85 at 700 °C

The diffusion coefficient can be estimated from the ion-concentration profile based on the STEM-EDS data (see below) after annealing for 30 min. The highest Zr^{4+} concentration was set as zero point, from which the scanning distance was derived. A constant background was subtracted based on the average concentration beyond 50 nm. The diffusion coefficient can be determined using the Matano method. The Matano plane is drawn such that the areas A1 and A2 are equal.

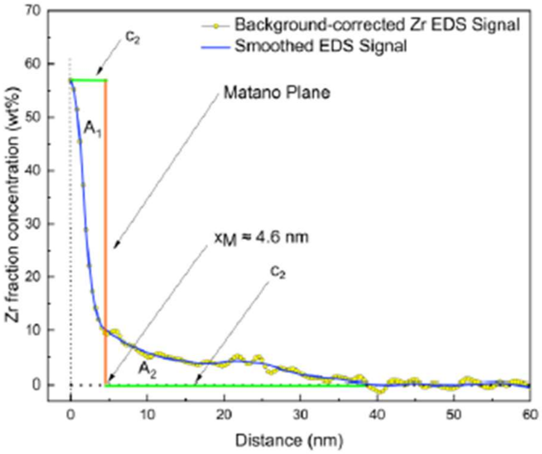

Zr^{4+} concentration profile after annealing at 700 °C for 30 min with denoted Matano plane.

Assuming the ideal case of two infinite half spaces, equation 1 is a solution to Fick's second law.

$$c(\mathrm{x,t}) = c_1 + \frac{c_2 - c_1}{2} \cdot \left(1 - \mathrm{erf}\left(\frac{x}{2\sqrt{D \cdot t}}\right)\right), \quad \text{(Eq. 1)}$$

where c_2 and c_1 are the ion concentrations at the surface and in the bulk of the NCM85, respectively, x represents the distance from the Matano plane and erf is the error function with:

$$\mathrm{erf(z)} = \frac{2}{\sqrt{\pi}} \int_0^{\mathrm{z}} \mathrm{e}^{-t^2}\, \mathrm{d}t. \qquad \text{(Eq. 2)}$$

The formula is applied for the distances 15, 20, 25, 30, 35 and 40 nm from the surface and the average diffusion coefficient is calculated to be $D \approx 3.8 \cdot 10^{-16}\ \frac{\mathrm{cm^2}}{\mathrm{s}}$.

6.2 Scientific Contributions

6.2.1 List of Publications

D. Kitsche, S. Schweidler, A. Mazilkin, H. Geßwein, F. Fauth, E. Suard, P. Hartmann, T. Brezesinski, J. Janek, M. Bianchini, The effect of gallium substitution on the structure and electrochemical performance of $LiNiO_2$ in lithium-ion batteries *Mater. Adv.* **2020**, *1*, 639.

D. Kitsche, Y. Tang, Y. Ma, D. Goonetilleke, J. Sann, F. Walther, M. Bianchini, J. Janek, T. Brezesinski, High Performance All-Solid-State Batteries with a Ni-Rich NCM Cathode Coated by Atomic Layer Deposition and Lithium Thiophosphate Solid Electrolyte. *ACS Appl. Energy Mater.* **2021**, *4*, 7338.

Y. Ma, J. H. Teo, **D. Kitsche**, T. Diemant, F. Strauss, Y. Ma, D. Goonetilleke, J. Janek, M. Bianchini, T. Brezesinski, Cycling Performance and Limitations of $LiNiO_2$ in Solid-State Batteries. *ACS Energy Lett.* **2021**, *6*, 3020.

F. Strauss,* **D. Kitsche**,* Y. Ma, J. H. Teo, D. Goonetilleke, J. Janek, M. Bianchini, T. Brezesinski, Operando Characterization Techniques for All-Solid-State Lithium-Ion Batteries. *Adv. Energy Sustain. Res.* **2021**, *2*, 2100004.

D. Kitsche, F. Strauss, Y. Tang, N. Bartnick, A. Kim, Y. Ma, C. Kübel, J. Janek, T. Brezesinski, A Quasi-Multinary Composite Coating on a Nickel-Rich NCM Cathode Material for All-Solid-State Batteries. *Batter. Supercaps* **2022**, *5*, e202100397.

D. Kitsche, Y. Tang, H. Hemmelmann, F. Walther, M. Bianchini, A. Kondrakov, J. Janek, T. Brezesinski, Atomic Layer Deposition-Derived Zirconia Coatings Ni-Rich Cathodes in Solid-State Batteries: Correlation Between Surface Constitution and Cycling Performance. *Small Sci.* **2022**, https://doi.org/10.1002/smsc.202200073.

* Shared first authorship

6.2.2 List of Patents

D. Kitsche, M. Bianchini, P. Hartmann, T. Brezesinski, J. Janek, Process for making an electrode active material, and electrode active material. *Patent pending* **2021**, CA3168384A1, WO2021170483A1

D. Kitsche, F. Strauss, A. Kondrakov, T. Brezesinski, Coated particulate material for use in an electrode of an electrochemical cell (Nb-based oxide coatings for NCM cathode active materials). *Patent pending* **2021**, European patent application no. 21212091.9

6.2.3 List of Conference Contributions

BASF International Scientific Network for Electrochemistry and Batteries – Meeting
Bad Dürkheim, Germany (2019)
Poster: The effect of gallium substitution on the structure and electrochemical performance of $LiNiO_2$ in lithium-ion batteries

European Materials Research Society – Fall Meeting
Virtual Conference (2021)
Presentation: ALD for Improved Performance of Ni-Rich NCM Cathode Materials in Lithium-Thiophosphate-Based Solid-State Batteries

242nd Meeting of the Electrochemical Society
Atlanta (GA), USA (2022)
Invited Presentation: ALD for Lithium Ion Battery and All-Solid-State Battery Applications

773th Wilhelm and Else Heraeus-Seminar: Materials and Energy - New Directions for the "Energiewende"
Bad Honnef, Germany
Poster: ALD-Derived Zirconia Coatings on Ni-Rich Cathodes in Solid-State Batteries: Correlation between Surface Constitution and Cycling Performance

7 Acknowledgements

Der Abschluss meiner Promotion ist ein Meilenstein in der langen Phase der Ausbildung in meinem Leben. Viele Menschen haben mich auf dem Weg hierher begleitet und unterstützt, wofür ich ihnen sehr dankbar bin.

Zunächst danke ich Prof. Dr. Jürgen Janek dafür, dass ich diese Doktorarbeit unter seiner Betreuung anfertigen konnte, für neue Ideen und Ratschläge und den offenen, lockeren, wertschätzenden und optimistischen Austausch in fachlichen und persönlichen Anliegen. An dieser Stelle sei auch herzlich Prof. Dr. Maren Lepple für das Koreferat, sowie Prof. Dr. Doreen Mollenhauer und PD Dr. Matthias Elm als weiteren Mitgliedern der Prüfungskommission gedankt.

Besonderer Dank gilt meinen Betreuern am BELLA dafür, dass sie einen guten Rahmen für meine Arbeit gegeben haben. Ich danke Pascal Hartmann für den ursprünglichen Kontakt und sein Angebot ans BELLA zu kommen. Aleksandr Kondrakov danke ich für die lockere und kollegiale Zusammenarbeit und die schnelle Bearbeitung von Freigaben etc. Sehr dankbar bin ich Matteo Bianchini für die umfangreiche Begleitung bei meinem ersten großen wissenschaftlichen Projekt im Rahmen meiner Masterarbeit, für die Einführung in zahlreiche Themen und Techniken und die respektvolle und freundschaftliche Zusammenarbeit und Förderung. Und schließlich danke ich Torsten Brezesinski für die Begleitung während der letzten Jahre, seinen Rat und die vielen Gespräche, die kollegiale Zusammenarbeit beim Meistern der zahlreichen kleinen und großen Aufgaben und Herausforderungen des (wissenschaftlichen) Alltags, für das verlässliche und zügige Abarbeiten jeglicher Anfragen und für das entgegengebrachte Vertrauen und die Freiheit zum selbstständigen Arbeiten.

Auch geht mein Dank an meine früheren und derzeitigen Kollegen und Freunde am BELLA und am INT, vor allem Florian Strauss, Sven Leuthner, Simon Schweidler, Katja Kretschmer, Dordije Tripkovic, Daniel Weber und Leonhard Karger. Ich konnte viel von ihnen lernen, sie jederzeit um Rat und Unterstützung bitten und mich mit ihnen über vielfältige Themen austauschen. Dies und noch viel mehr hat meinen wissenschaftlichen Alltag leichter, unterhaltsamer, und, wenn nötig, erträglicher gemacht hat.

Ich bin dankbar für die finanzielle und ideelle Unterstützung, die ich Rahmen meines Kekulé-Stipendiums vom Fonds der chemischen Industrie (VCI) erhalten habe.

Großer Dank gilt meinen Eltern für ihre langjährige Unterstützung, ihr Verständnis, ihre Ermutigungen und die Hoffnung, die sie in mich gesetzt haben. Sehr dankbar bin ich auch für meinen Bruder Jonas, meine ganze Familie und meine Freunde, die meinem Leben einen Kontext und eine Heimat geben. Die eigentlichen Meilensteine der letzten Jahre sind verbunden mit der Vertiefung meiner Beziehung zu meiner Partnerin Magda. Ich bin sehr glücklich, stolz und etwas erstaunt, wenn ich auf den Start unserer gemeinsamen Wohngemeinschaft, unsere Verlobung, unsere Eheschließung und die Gründung unserer eigenen Familie schaue. Unser wunderbarer Sohn Theo ist der absolute Höhepunkt dieser „kumulativen Ereignisse“ und ein großes Geschenk. Mit euch beiden schaue ich zuversichtlich in die Zukunft, ohne genau zu wissen, was sie bringt, denn „I like living with you.“ und „You make me happy when skies are grey.“